Civil and Computational Engineering Center
Prifysgol Abertawe
Swansea University

Computational Homogenization of Heterogeneous Hyperelastic Materials

Monica Zakhari
Supervised by Prof. Djordje Perić

Submitted to Swansea University in partial fulfillment of the requirements for the degree of Master of Science in Computational Mechanics.
Swansea University,
May 2013

Declarations and Statements

Declaration

This work has not previously been accepted in substance for any degree and is not being concurrently submitted in candidature for any degree.

Signed .....
Date .....

Statement 1

This dissertation is the result of my own independent work/investigation, except where otherwise stated. Other sources are acknowledged by footnotes giving explicit references. A bibliography is appended.

Signed .....
Date .....

Statement 2

I hereby give my consent for my dissertation, if relevant and accepted, to be available for photocopying and for inter-library loan, and for the title and summary to be made available to outside organisations.

Signed .....
Date .....

Acknowledgments

This thesis would not have been possible without the guidance, help, and enthusiastic encouragement of Prof. Djordje Perić, my supervisor, to whom I owe my sincere gratitude. I consider it an honor to work with him.

I would like to offer my special thanks to Prof. E. A. de Souza Neto for sharing his initial code and experience, and for providing insights when needed.

I would like also to acknowledge the European commission joint with CIMNE for their generous financial support through the Erasmus Mundus scholarship and for letting me be part of this program at the Technical University of Catalonia (UPC) and at Swansea University.

I owe the deepest gratitude to my parents, Edward and Mervat, and my sisters, Lydia and Madonna, for their continuous support and encouragement throughout my study.

Last but not least, I am deeply grateful to my fiancé Michael for his companionship and patience at all times, for his faith in me, and for allowing me to be as ambitious as I wanted.

Summary

This work is concerned with the implementation of the homogenization-based multi-scale finite element analysis of solids at finite strains. This is for the purpose of investigating the behavior of heterogeneous materials knowing the behavior of its constituents at the microscopic level. Computational homogenization is chosen for its versatility. The theory defines different multi-scale model which, in turn, defines the choice of the boundary conditions imposed on the representative volume element of the microstructure. These are namely, the Taylor, the linear boundary displacements, the periodic boundary fluctuations and the minimally constraint models.

For the same purpose, analytical estimates for nonlinear composites are addressed. An implementation of a framework based on the Second-Order Estimate is developed and tested against results based on the homogenization theory and available analytical solutions. The presented implementation of the Second-Order Estimate has shown to approximate effectively all stress components for compressible and incompressible representative volume elements with larger error values for the latter. A modification of the formulation is performed to accommodate the overall incompressibility of the representative volume elements.

Numerical examples such as porous solids and solids with rigid inclusions are presented to demonstrate the characteristics and the effectiveness of the strategy used. These examples confirm that computational homogenization provides outstanding results for heterogeneous materials with high statistical sample. This is also supported by the comparison performed with available analytical estimates. Consequently, this efficient computational homogenization framework provides a robust platform for the effective computation of the response of generic heterogeneous materials for which analytical solutions are generally not available.

Table of Contents

Table of Contents . . . vii
List of Figures . . . xi
List of Tables . . . xiv
List of Important Symbols . . . xvii

1 Introduction **1**
1.1 Aim of the Work . . . 2
1.2 Layout of the Thesis . . . 3

2 Elements of Continuum Mechanics and Finite Element Formulation **5**
2.1 Kinematics . . . 5
2.1.1 The Deformation Gradient . . . 6
2.1.2 Polar Decomposition of the Deformation Gradient . . . 7
2.1.3 Volume Changes and Isochoric/Volumetric Split . . . 8
2.1.4 Strain . . . 8
2.2 Stress . . . 9
2.2.1 Some Stress Tensors . . . 9
2.3 Equilibrium and Principle of Virtual Work . . . 11
2.3.1 Translational Equilibrium . . . 11
2.3.2 Rotational Equilibrium . . . 12
2.3.3 The Principle of Virtual Work . . . 12
2.3.4 The Boundary Value Problem . . . 13
2.4 Constitutive Equations . . . 13
2.4.1 Hyperelasticity . . . 13
2.4.2 Linearisation of the Internal Virtual Work . . . 14
2.4.3 Constitutive Model and Derivation of the Material Tangent Modulus 15
2.5 Finite Element Approximation . . . 19
2.6 Newton-Raphson Solution . . . 20

3 Homogenization: Finite Strain Formulation **21**
3.1 Equilibrium Equations in the Reference Configuration . . . 22
3.1.1 Equilibrium of the Macro-continuum . . . 22
3.1.2 Equilibrium of the Representative Volume Element . . . 22
3.2 Micro-to-Macro Transitions: Homogenized Properties . . . 23

3.2.1 Homogenized Deformation Gradient . . . 23
3.2.2 Homogenized Stress . . . 24
3.2.3 Additive Split of the Microscopic Displacement Field . . . 25
3.2.4 The Hill-Mandel Principle of Macro-homogeneity . . . 26
3.3 Kinematical Constraints . . . 27
3.3.1 The Minimum Kinematical Constraint . . . 27
3.3.2 Multi-scale Models . . . 28

4 Multi-Scale Finite Element Formulation 31
4.1 Linearisation of Microscopic Equilibrium Equation . . . 31
4.2 Voigt Notation . . . 32
4.3 Finite Element Discretization and Solution of the Microscopic Equilibrium Equation . . . 32
4.4 Finite Element Implementation of the Multi-scale Models . . . 34
4.4.1 Discretization of the Minimally Constrained Model . . . 34
4.4.2 Discretization of the Periodic Boundary Fluctuations Model . . . 36
4.4.3 Discretization of the Linear Boundary Displacements Model . . . 37
4.4.4 Discretization of the Taylor Model . . . 37
4.5 The Overall Procedure . . . 38

5 Analytical Estimates of the Behavior of Heterogeneous Hyperelastic Materials 41
5.1 The Effective Strain Energy Function . . . 42
5.2 The Second-Order Estimate . . . 42
5.2.1 The Second-Order Estimate for Two-phase Composites . . . 43
5.2.2 The Overall Second-Order Estimate Procedure . . . 45
5.3 Analytical Estimates for Special Cases . . . 47
5.3.1 Classical Voigt Upper Bound Estimate for Porous Materials . . . 47
5.3.2 Analytical Solution for Incompressible Porous Neo-Hookean Solids . 47
5.3.3 Analytical Solution for Incompressible Neo-Hookean Solids with Rigid Inclusions . . . 49
5.4 Validation of the Second-Order Estimate . . . 50
5.4.1 Porous Incompressible Neo-Hookean Solid: Analytical Estimates . . 50
5.4.2 Incompressible Neo-Hookean Solid with Rigid Inclusions: Analytical Estimates . . . 52

6 Computational Homogenization of Hyperelastic Materials 55
6.1 Porous Hyperelastic Solids . . . 55
6.1.1 Compressible Matrix Material under Simple In-plane Shear Loading 55
6.1.2 Incompressible Matrix Material under Simple In-plane Shear Loading 58
6.1.3 Incompressible Matrix Material under In-plane hydrostatic Loading 62
6.2 Incompressible Hyperelastic Solids with Rigid Inclusions . . . 65
6.3 Remarks on Finite Element Implementation . . . 71

7 Conclusions **77**

A Analytical Solution for Homogeneous Simple Shear Deformation **79**

List of Figures

1.1 Examples of heterogeneous microstructures. (a) Carbon fibre reinforced composite [31], (b) AlSi12Cu4MgNi2 alloy microstructure [13], (c) polycrystalline metal before deformation: equiaxed grains [26] and (d) polycrystalline metal after deformation: elongated grains [26]. 2

2.1 Generic motion of a deformable body from its reference configuration Ω (at time $= 0$) to a current (deformed) configuration at time t. 6

2.2 Current configuration of a general deformable body showing the resultant force on an infinitesimal area. 10

3.1 Deformation of the macro-continuum and a locally attached microstructure. 24

3.2 Additive split of the microscopic displacement field. 26

3.3 Square RVE for the periodic boundary fluctuations model. 29

4.1 Square RVE for the minimally constrained model showing the interior i, prescribed p, dependent d and free f dofs. 36

4.2 Square RVE for the periodic boundary fluctuations model showing the interior i, prescribed p dofs together with dofs belonging to Γ^+ denoted by $+$ and those belonging to Γ^- denoted by $-$. 37

4.3 The overall finite element procedure to solve the microscopic equilibrium problem and obtain homogenized properties. 39

5.1 Procedure followed for the computation of the Second-Order Estimate given the material properties, the prescribed macroscopic deformation gradient and the constitutive model. 46

5.2 The first Piola-Kirchhoff stress components for the Second-Order Estimate and the analytical solution for a porous incompressible Neo-Hookean solid subjected to simple in-plane shear deformation. The void volume fraction used is 20%. 51

5.3 The first Piola-Kirchhoff stress for the Second-Order Estimate and the analytical solution for a porous incompressible Neo-Hookean solid subjected to in-plane hydrostatic deformation. 52

5.4 The first Piola-Kirchhoff stress components of the Second-Order Estimate and the analytical solution for a porous incompressible Neo-Hookean solid subjected to simple in-plane shear deformation. The void volume fraction used is 20%. 53

6.1 Porous representative volume elements with void volume fraction of $c_o = 20\%$ meshed with 3-noded triangular elements. 56

6.2 Comparison between different multi-scale models for an RVE with a single circular void and another with randomly distributed voids both with initial void volume fraction of $c_o = 20\%$ and Hencky matrix material. The behavior obtained from the SOE and the Voigt upper bound are also provided. . . . 57

6.3 Comparison between different multi-scale models for an RVE with a single circular void and another with randomly distributed voids both with initial void volume fraction of $c_o = 20\%$ and compressible Neo-Hookean matrix material. SOE and the Voigt upper bound are plotted for comparison. . . . 58

6.4 Deformation of two porous representative volume elements with compressible Hencky matrix material and a void volume fraction of $c_o = 20\%$. One consists of a single void (first row) and the other is formed of a random distribution of voids (second row) under different magnitudes of shear, $\gamma = 0.28$, 0.42, and 0.56 (from left to right respectively) using the periodic boundary fluctuation assumption. 59

6.5 Shear component of the first Piola-Kirchhoff stress (P_{12}/μ) of two porous representative volume elements with compressible Neo-Hookean matrix material and a void volume fraction of $c_o = 20\%$. One consists of a single void (left) and the other is formed of a random distribution of voids (right). These are subjected to the linear boundary displacement assumption (first row), the periodic boundary fluctuation assumption (second row), and the uniform boundary traction assumption (third row) at a shear of $\gamma = 0.7$. . 60

6.6 Comparison between different multi-scale models for an RVE with a single circular void and another with randomly distributed voids both with initial void volume fraction of $c_o = 20\%$ and incompressible Neo-Hookean matrix material. SOE and analytical solution are also plotted for comparison. . . . 61

6.7 Deformation of porous representative volume element with incompressible Neo-Hookean matrix material and single void of volume fraction of $c_o = 20\%$ under different magnitudes of shear using the uniform boundary traction assumption. 62

6.8 Shear component of the first Piola-Kirchhoff stress (P_{12}/μ) (first row) and the pressure values (second row) for a representative volume element with a single void of $c_o = 20\%$ volume fraction. This is subjected to a shear of magnitude $\gamma = 1$ using the linear boundary displacement assumption (first column), the periodic boundary fluctuation assumption (second column) and uniform boundary traction (third column). 63

6.9 Porous representative volume elements with different volume fractions meshed with 4-noded quadrilateral elements. 63
6.10 The first Piola-Kirchhoff stress for the homogenized behavior, the Second-Order Estimate (SOE), and the analytical solution for a porous incompressible Neo-Hookean solid subjected to hydrostatic deformation of magnitude α. 64
6.11 Deformation (right) and the first Piola-Kirchhoff stress (P_{11}/μ) of a representative volume element with 50% void volume fraction subjected to in-plane hydrostatic loading of magnitude $\alpha = 1.35$ using the linear boundary displacement assumption (first row), the periodic boundary fluctuation assumption (second row) and uniform boundary traction (third row). 65
6.12 Deformation of a representative volume element subjected to in-plane hydrostatic loading of magnitude α using the linear boundary displacement assumption (first row), the periodic boundary fluctuation assumption (second row) and uniform boundary traction (third row). The initial void volume fraction used is $c_o = 30\%$. 66
6.13 Deformed mesh of two representative volume elements under the linear boundary displacement assumption (black) and the periodic boundary fluctuation assumption (red) at $\alpha = 1.25$. 67
6.14 Solid with a single rigid inclusion. 67
6.15 Comparison between different multi-scale models for a solid with a single rigid inclusion of initial volume fraction of $c = 20\%$ and incompressible Neo-Hookean matrix material. These are also compared to the SOE and the analytical solution. 68
6.16 Deformation of a representative volume element with a single rigid inclusion subjected to in-plane simple shear loading of magnitude γ using the linear boundary displacement assumption (first row), the periodic boundary fluctuation assumption (second row) and uniform boundary traction (third row). The inclusion volume fraction used is $c = 20\%$. 69
6.17 Shear component of the first Piola-Kirchhoff stress (P_{12}/μ) (first row) and the pressure values (second row) for a representative volume element with a single rigid inclusion of $c = 20\%$ volume fraction, subjected to a shear of magnitude $\gamma = 1$ using the linear boundary displacement assumption (first column), the periodic boundary fluctuation assumption (second column) and uniform boundary traction (third column). 70
6.18 Different finite elements. ($\times$) denotes a Gauss point and ($\bullet$) denotes a node. 71
6.19 The first Piola-Kirchhoff stress for the homogenized behavior of a porous incompressible Neo-Hookean solid subjected to in-plane simple shear deformation using different discretization elements. The linear boundary displacements model is used. 72
6.20 Shear component of the first Piola-Kirchhoff stress (P_{12}/μ) (left) and pressure distribution (right) of porous representative volumes discretized using different elements. The linear boundary displacements model is used. . . . 73

6.21 Shear component of the first Piola-Kirchhoff stress (P_{12}/μ) (left) and pressure distribution (right) of porous representative volumes discretized using different elements. The periodic boundary fluctuations model is used. . . . 74
6.22 Shear component of the first Piola-Kirchhoff stress (P_{12}/μ) (left) and pressure distribution (right) of porous representative volumes discretized using different elements. The uniform boundary model is used. 76

A.1 Analytical solution versus multi-scale solution obtained for a homogeneous RVE made of 32 linear triangular elements subjected to Periodic Boundary Conditions. 81

List of Tables

6.1 Residual values of a representative volume element with a single void and compressible Neo-Hookean matrix material at a shear of $\gamma = 0.56$. 58
6.2 Residual values of a representative volume element with randomly distributed voids and compressible Neo-Hookean matrix material at a shear of $\gamma = 0.56$. 59
6.3 Residual values of a representative volume element with a single void and incompressible Neo-Hookean matrix material at a shear of $\gamma = 0.6$. 61
6.4 Residual values of a representative volume element with a single rigid inclusion and incompressible Neo-Hookean matrix material at a shear of $\gamma = 0.6$. 69

List of Important Symbols

$(\cdot)_d$	Quantity $(\cdot)$ in the deformed/current configuration
$(\cdot)_\mu$	A microscopic quantity
$\bar{(\cdot)}$	A macroscopic quantity
$\boldsymbol{\sigma}$	Cauchy stress tensor
$\boldsymbol{\tau}$	Kirchhoff stress tensor
$\boldsymbol{\varepsilon}$	Almansi strain tensor
$\boldsymbol{B}$	Left Cauchy-Green strain tensor
$\boldsymbol{b}$	Body force per unit volume
$\boldsymbol{C}$	Right Cauchy-Green strain tensor
$\boldsymbol{E}$	Green-Lagrange strain tensor
$\boldsymbol{F}$	Deformation gradient tensor
$\boldsymbol{F}^{\mathrm{v}}$	Volumetric component of $\boldsymbol{F}$
$\boldsymbol{I}$	Second-order identity tensor
$\boldsymbol{N}_\alpha$	Principal directions of $\boldsymbol{U}$
$\boldsymbol{n}_\alpha$	Principal direction of $\boldsymbol{V}$
$\boldsymbol{P}$	First Piola-Kirchhoff stress tensor
$\boldsymbol{R}$	Rotation tensor
$\boldsymbol{S}$	Second Piola-Kirchhoff stress tensor
$\boldsymbol{t}$	Traction force
$\boldsymbol{U}$	Material stretch tensor

$\boldsymbol{u}$	Material displacement vector
$\boldsymbol{V}$	Spatial stretch tensor
$\boldsymbol{x}$	Particle position in the reference configuration
$\boldsymbol{x}_d$	Particle position in the current configuration
$\mathbf{P}$	Hill polarization tensor
$\mathbf{S}^{(r)}$	Strain-concentration tensor of phase r
$\boldsymbol{\varphi}$	Mapping between reference and current configurations
$\hat{\boldsymbol{F}}$	Isochoric/distortional component of $\boldsymbol{F}$
λ_α	Principal stretches
$\mathfrak{F}$	Generic constitutive functional
$\mathscr{K}$	Space of kinematically admissible displacements
$\mathscr{V}$	Space of virtual kinematically admissible displacements
Ω	Initial macro-continuum domain
ω	Current (deformed) macro-continuum domain
$\tilde{\boldsymbol{u}}_{\boldsymbol{\mu}}$	Microscopic displacement fluctuation field.
$\tilde{\Psi}$	Effective strain energy function.
J	Jacobian - determinant of $\boldsymbol{F}$
X_i	Cartesian coordinates in the reference configuration
x_i	Cartesian coordinates in the current configuration

Chapter 1

Introduction

The desirable performance of modern applications lies in the tailored behavior of the material of their components. This is, often, accomplished inexpensively by manipulating the microstructure of the material, i.e. by introducing microstructural heterogeneity. Almost any material is heterogeneous on the microstructural level, even if the observed marcoscopic structure appears homogeneous. For instance, composite materials have two or more phases with distinct interface even on the macroscopic level. Inclusions in metal alloys provide another form of heterogeneity, where they do not take a specific geometry but rather vary in shape and size. Polycrystalline metals are characterized by grains of different sizes and crystallographic orientation which affect significantly the overall properties of the metal. For example, metal forming processes can orient the grains in a certain direction in which the properties are enhanced leading to an overall anisotropic behavior (see Figure 1.1). Even porosity in that sense is a form of heterogeneity appearing, for example, in bone structure.

As mentioned earlier tailoring macroscopic material properties to fit a specific application is achieved by adding another phase with different properties to the matrix phase forming the microstructure. This requires a means of linking both scales. Over the past few years, interest has been directed to *multi-scale* modeling. This consists of solving the equilibrium equation for a *representative volume element* of the microstructure and obtain macroscopic properties using volume averaging the microscopic properties. This is known as *homogenization*. The exchange of properties from the macrostructure to the microstructure is known as *localization*. Elaborate explanation of the multi-scale theory can be found, for instance, in Moulinec and Suquet (1998) [27], Miehe *et al.* (1999) [25], Kouznetsova *et al.* (2001) *et al.* [12], Zohdi and Wriggers (2005) [42], de Souza Neto and Feijóo (2006) [4], and Perić *et al.* (2011) [33]

The versatility of the multi-scale theory makes it most suitable for modeling nonlinear heterogeneous materials. However, several attempts have been made to obtain the behavior of such materials as analytical as possible. For instance, estimates analogous to Voigt and Reuss bounds are introduced by Hill (1951), generalization of the Hashin-Shtrikman bounds to accommodate nonlinear elastic behavior developed by Willis (1983), and other more involved estimates formulated by Ponte Castañeda (1989) [38]. The recently devel-

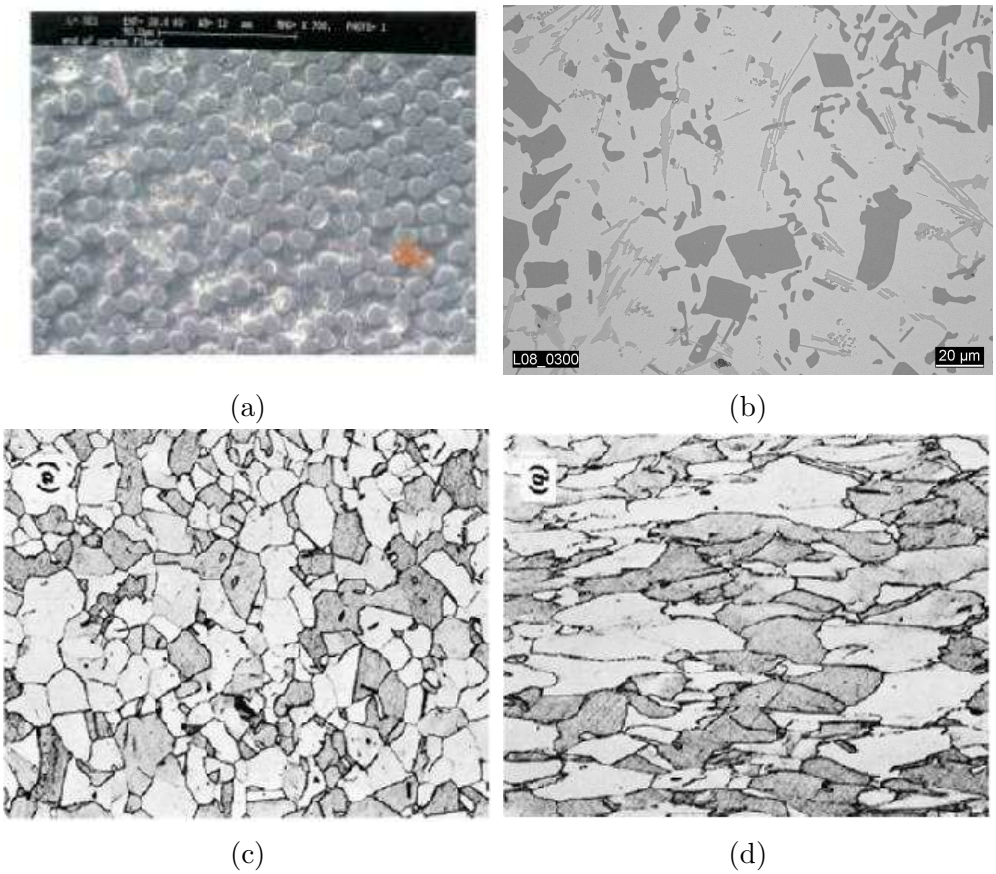

(a) (b)

(c) (d)

Figure 1.1: Examples of heterogeneous microstructures. (a) Carbon fibre reinforced composite [31], (b) AlSi12Cu4MgNi2 alloy microstructure [13], (c) polycrystalline metal before deformation: equiaxed grains [26] and (d) polycrystalline metal after deformation: elongated grains [26].

oped *Second-Order Estimate* method by Ponte Castañeda and co-workers was shown to be effective in approximating the behavior of nonlinear composite materials (Ponte Castañeda (1996) [36], Ponte Castañeda and Tiberio (2000) [34], Ponte Castañeda (2002) [37], Lopez-Pamies and Ponte Castañeda (2004, 2006, 2007) [16–19]). It was initially developed by Ponte Castañeda (1996) [36] for small strains, power-law materials and extended later to hyperelastic materials [34]. This method is further being developed, for instance, Ponte Castañeda (2012) [35].

1.1 Aim of the Work

This work aims at implementing a computational framework for the homogenization-based multi-scale finite element analysis of two-dimensional solids at finite strains. The framework is specified for the use of hyperelastic constitutive laws for the constituents of the

microstructure. The kinematical variational framework implemented is based on the equilibrium of the representative volume element, relating stresses and deformations between scales through volume averaging, the additive split of the microscopic displacements and hence defining the kinematical constraints, and finally, the Hill-Mandel Principle of Macro-homogeneity. This establishes several possible boundary conditions over the representative volume element.

Additionally, the implementation of analytical estimates for nonlinear heterogeneous materials form another aim for the present work. This will be based on the Second-Order Estimate developed by Ponte Castañeda [34] with the ultimate goal of accomplishing this as generic and as simple as possible. The implementation is focused on two-phase composite materials with the use of the Hashin-Shtrikman bounds for the linearised behavior. In that sense, one only requires the local constitutive laws describing the composite material that are introduced to the framework and the output will be an estimate of the macroscopic stress tensor.

1.2 Layout of the Thesis

Chapter 2 covers the basic elements of continuum mechanics: kinematics, the concept of stress, strong and weak forms of the equilibrium equation and constitutive laws specified to hyperelasticity. It also provides a brief description of the Finite Element approximation and the solution of the discretized problem using Newton-Raphson algorithms.

Chapter 3 provides the finite strain formulation of the homogenization theory. The equilibrium equations of the macrostructure and the microstructure are formulated as well as the micro-to-macro transition parameters. These are the homogenized deformation gradient and stress, the additive split of the microscopic displacements and the Hill-Mandel Principle of Macro-homogeneity. And finally, the kinematical constrains and the different multi-scale models are developed.

Chapter 4 covers the Finite Element implementation of the multi-scale models described in the previous chapter. It starts from the linearisation of the microscopic equilibrium equation and providing the Voigt notation essential for the implementation.

Chapter 5 describes the theory behind the Second-Order Estimate. The overall procedure implemented is then provided for a general two-phase composite made of hyperelastic materials. Other specialized analytical solutions are provided, namely, for porous solids with incompressible Neo-Hookean matrix material under a general loading and solids with rigid inclusion with incompressible Neo-Hookean matrix material. A validation of the implemented Second-Order Estimate against the available analytical solutions is done.

Chapter 6 demonstrates examples of the use of the implemented homogenization framework for porous solids and solids with rigid inclusions under several loading conditions. A

sensitivity analysis to the type of elements used for the discretization is also studied.

Chapter 7 provides the conclusions drawn from the presented work and suggestions for future work.

Chapter 2

Elements of Continuum Mechanics and Finite Element Formulation

A *continuum* is a body formed of an infinite number of particle describing the material it is made of. The *continuum mechanics* describes the mechanical behavior of such bodies. It assumes that these bodies can be described with certain field quantities treating the body as a continuous medium. This is an approximation as any matter is heterogeneous on certain scale. Besides, it is not valid, for example, on the molecular level, where discontinuities are of a similar order as the characteristic dimensions of the body studied and hence can not be neglected. Even though this study is concerned with heterogeneous materials, they are treated in a continuum manner, and the behavior of micro-constituents composing the heterogeneous body can be described based on the continuum theory.

This chapter is concerned with the basic concepts of continuum mechanics. The *kinematics* of *finite deformation* is first described, providing the concept of deformation gradient in addition to some measures of strain. This is then followed by a description of the causes of deformation such as forces in addition to the concept of stress. This also involves the definition of several stress tensors. Later, the *constitutive laws* relating the stress to the corresponding measure of strain are provided by introducing the concept of *hyperelasticity*. Finally, the equilibrium equations defining the problem are set in addition to the introduction of the *Principle of Virtual Work*. This is followed by a concise description of the *finite element* formulation and the solution of such nonlinear problems via a *Newton-Raphson* algorithm.

The material provided in the chapter is described in detail in a number of references. As for the current work, it is referred to the book by de Souza Neto *et al.* [5] and the book by Bonet and Wood [1].

2.1 Kinematics

Consider a generic motion of a deformable body denoted initially by Ω illustrated in Figure 2.1. It is assumed that the body is made up of a collection material particles each of

them described by the Cartesian coordinates (X_1, X_2, X_3) in the *initial* or *undeformed configuration* [1] and (x_1, x_2, x_3) in the *current* or *deformed configuration*. At time t, a material particle located at position $\boldsymbol{x}$ is moved to a current position $\boldsymbol{x}_d$ on the deformed body ω by a displacement vector $\boldsymbol{u}(\boldsymbol{x}, t)$ expressed with respect to the initial configuration. This motion is mathematically described by the mapping $\boldsymbol{\varphi}$ relating the reference and

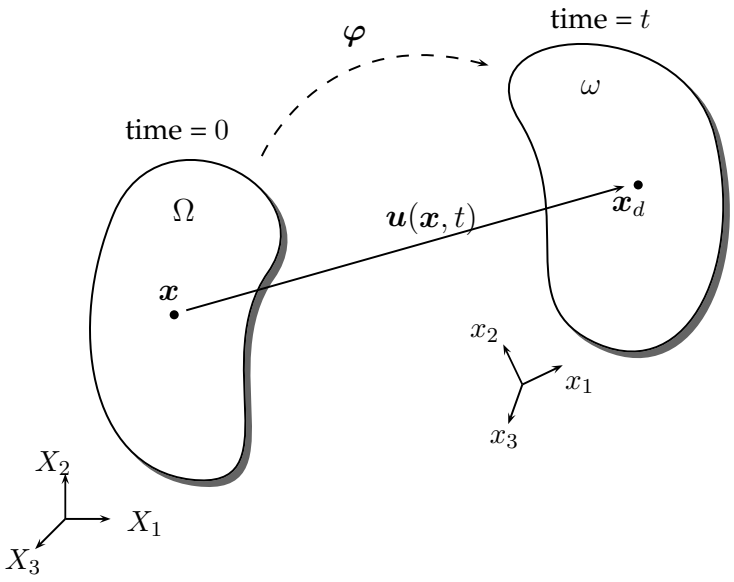

Figure 2.1: Generic motion of a deformable body from its reference configuration Ω (at time $= 0$) to a current (deformed) configuration at time t.

current configurations as

$$\boldsymbol{x}_d \equiv \boldsymbol{\varphi}(\boldsymbol{x}, t) = \boldsymbol{x} + \boldsymbol{u}(\boldsymbol{x}, t). \tag{2.1}$$

It is to be noted that for small strains the displacement between $\boldsymbol{x}$ and $\boldsymbol{x}_d$ is small compared to the dimensions of the body that its effect on the deformation and any related parameters is ignored.

Based on that, it is essential to make a distinction between fields, used to describe the motion of the body, expressed with respect to its reference and current configurations. The former is known as a *material* or *Lagrangian* description while the latter is called a *spatial* or *Eulerian* description. Tensors are defined similarly into material (Lagrangian) and spatial (Eulerian) tensors implying the description they refer to.

2.1.1 The Deformation Gradient

The deformation gradient is of particular importance in the continuum mechanics theory in finite strains. The reason for this is that it is involved in relating quantities before

[1] For the current work and without loss of generality, it is assumed that the initial configuration coincides with the reference configuration.

and after deformation. The deformation gradient, denoted by $\boldsymbol{F}$, relates infinitesimal vectors between two points in the reference configuration to the corresponding vector in the deformed configuration. In that sense, $\boldsymbol{F}$ is a *two-point tensor*, i.e. it relates quantities in two different configurations. Tensor $\boldsymbol{F}$ is defined as

$$\boldsymbol{F} \equiv \frac{\partial \boldsymbol{x}_d}{\partial \boldsymbol{x}}, \tag{2.2}$$

which can be equivalently written as

$$\boldsymbol{F} = \frac{\partial \boldsymbol{\varphi}}{\partial \boldsymbol{x}} = \frac{\partial \left(\boldsymbol{x} + \boldsymbol{u}(\boldsymbol{x}, t)\right)}{\partial \boldsymbol{x}} = \boldsymbol{I} + \nabla \boldsymbol{u}, \tag{2.3}$$

where ∇ denoted the gradient operator with respect to the initial coordinates, $\boldsymbol{I}$ is the second-order identity tensor, and identity 2.1 is taken into consideration.

2.1.2 Polar Decomposition of the Deformation Gradient

An advantageous use of the deformation gradient is its polar decomposition, that is decomposing the total deformation $\boldsymbol{F}$ into a tensor describing the rotation and another one describing the stretch. Mathematically, the polar decomposition, in the material configuration, is expressed as

$$\boldsymbol{F} \equiv \boldsymbol{R}\boldsymbol{U}, \tag{2.4}$$

where $\boldsymbol{R}$ is the *rotation tensor* which is an orthogonal tensor, i.e. $\boldsymbol{R}\boldsymbol{R}^T = \boldsymbol{I}$. While $\boldsymbol{U}$ is the *material stretch tensor* which is a symmetric tensor, i.e. $\boldsymbol{U} = \boldsymbol{U}^T$. Equivalently, in the spatial configuration, the polar decomposition is expressed as

$$\boldsymbol{F} \equiv \boldsymbol{V}\boldsymbol{R}, \tag{2.5}$$

where $\boldsymbol{V}$ is the *spatial stretch tensor* that is also symmetric. The detailed description of the polar decomposition is provided thoroughly in chapter 3 in [5] and in chapter 4 in [1].

It can be shown that both tensors $\boldsymbol{U}$ and $\boldsymbol{V}$ share the same principal values [1, 5]. As both tensors are symmetric, the spectral theorem can be applied. Thus, tensors $\boldsymbol{U}$ and $\boldsymbol{V}$ can be conveniently expressed as

$$\boldsymbol{U} = \sum_{\alpha=1}^{n} \lambda_\alpha \boldsymbol{N}_\alpha \otimes \boldsymbol{N}_\alpha \tag{2.6}$$

and

$$\boldsymbol{V} = \sum_{\alpha=1}^{n} \lambda_\alpha \boldsymbol{n}_\alpha \otimes \boldsymbol{n}_\alpha, \tag{2.7}$$

where λ_α are the principal stretches, $\boldsymbol{N}_\alpha$ are the material principal directions of $\boldsymbol{U}$, $\boldsymbol{n}_\alpha$ are the spatial principal directions of $\boldsymbol{V}$, and n is the number of dimensions involved.

2.1.3 Volume Changes and Isochoric/Volumetric Split

The deformation gradient is also used to obtain information about volume changes in the body studied. It can be shown that the determinant of $\boldsymbol{F}$ gives the ratio between differential volumes in the reference (dv) and current configurations (dv_d) [1, 5]. This can be written as

$$J = \det \boldsymbol{F} = \frac{dv_d}{dv}, \tag{2.8}$$

where J is the Jacobian. If $J = 1$, then no volumetric deformations are involved.

It is crucial, when dealing with incompressible or nearly incompressible materials, to split the deformation into *volumetric* components and *isochoric* or *distortional* components. The aim of this split is to ensure that the isochoric component of the deformation, denoted by $\hat{\boldsymbol{F}}$, does not contribute to any volume changes, that is

$$\det \hat{\boldsymbol{F}} = 1. \tag{2.9}$$

Such a condition is satisfied for the following form of $\hat{\boldsymbol{F}}$:

$$\hat{\boldsymbol{F}} = J^{-\frac{1}{3}} \boldsymbol{F}, \tag{2.10}$$

while the volumetric component $\boldsymbol{F}^{\mathrm{v}}$ can be expressed as

$$\boldsymbol{F}^{\mathrm{v}} = J^{\frac{1}{3}} \boldsymbol{I}. \tag{2.11}$$

2.1.4 Strain

Several strain tensors are constructed from the deformation gradient tensor. Strain tensors are further categorized as material or spatial strain tensors based on the description they refer to. Some of the strain tensors in each category will be described in the following.

The *right Cauchy-Green* tensor is a material strain tensor that is expressed in terms of the deformation gradient tensor. It is defined as

$$\boldsymbol{C} \equiv \boldsymbol{F}^T \boldsymbol{F} = \boldsymbol{U} \boldsymbol{R}^T \boldsymbol{R} \boldsymbol{U} = \boldsymbol{U}^2, \tag{2.12}$$

where the polar decomposition 2.4 is used. In view of 2.6, this can be equivalently expressed as

$$\boldsymbol{C} = \sum_{\alpha=1}^{n} \lambda_\alpha^2 \boldsymbol{N}_\alpha \otimes \boldsymbol{N}_\alpha. \tag{2.13}$$

The strain tensor $\boldsymbol{C}$ is then used to define another material strain tensor, namely, the *Green-Lagrange* strain tensor defined as

$$\boldsymbol{E} \equiv \frac{1}{2} \left(\boldsymbol{C} - \boldsymbol{I} \right). \tag{2.14}$$

Similarly, spatial strain tensors can be constructed. The *left Cauchy-Green* strain tensor is given by

$$\boldsymbol{B} \equiv \boldsymbol{F}\boldsymbol{F}^T = \boldsymbol{V}\boldsymbol{R}\boldsymbol{R}^T\boldsymbol{V} = \boldsymbol{V}^2, \tag{2.15}$$

where Equation 2.5 is used to obtain the last equality. Using Equation 2.7, $\boldsymbol{B}$ can hence be expressed as

$$\boldsymbol{B} = \sum_{\alpha=1}^{n} \lambda_\alpha^2 \boldsymbol{n}_\alpha \otimes \boldsymbol{n}_\alpha. \tag{2.16}$$

Another measure of spatial strain tensors is the *Almansi* tensor , defined based on the left Cauchy-Green tensor as

$$\boldsymbol{\varepsilon} \equiv \frac{1}{2}\left(\boldsymbol{I} - \boldsymbol{B}^{-1}\right). \tag{2.17}$$

2.2 Stress

Consider an infinitesimal area Δa in the vicinity of a particle position $\boldsymbol{x}_d$ belonging to a deformable body in its current configuration (ω) as shown in Figure 2.2. If the resultant force acting on this area is denoted by $\Delta \boldsymbol{f}_d$, the corresponding traction force is

$$\boldsymbol{t}_d(\boldsymbol{n}) \equiv \lim_{\Delta a \to 0} \frac{\Delta \boldsymbol{f}_d}{\Delta a}, \tag{2.18}$$

where $\boldsymbol{n}$ is the outward normal to Δa at point $\boldsymbol{x}_d$. The traction force satisfies Newton's third law, that is

$$\boldsymbol{t}_d(-\boldsymbol{n}) = -\boldsymbol{t}_d(\boldsymbol{n}). \tag{2.19}$$

This traction force is then related to the normal vector via the *Cauchy stress* tensor $\boldsymbol{\sigma}$ as

$$\boldsymbol{t}_d(\boldsymbol{n}) \equiv \boldsymbol{\sigma}\boldsymbol{n}, \text{ where } \boldsymbol{\sigma} = \sum_{i,j=1}^{n} \sigma_{ij} \boldsymbol{e}_i \otimes \boldsymbol{e}_j \tag{2.20}$$

in Cartesian coordinates with basis unit vectors $\boldsymbol{e}$ in the current configuration. The Cauchy stress is a spatial tensor as it relates the current force vector to the deformed area.

2.2.1 Some Stress Tensors

Other stress tensors can be constructed from the previously described measure of stress. Some of these stress tensors are provided in the following.

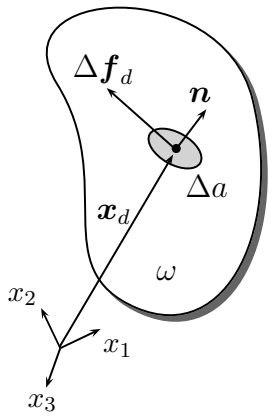

Figure 2.2: Current configuration of a general deformable body showing the resultant force on an infinitesimal area.

The First Piola-Kirchhoff Stress

The *first Piola-Kirchhoff stress* tensor, similar to $\boldsymbol{F}$, is a two-point tensor that can be related to the Cauchy stress via the following relation,

$$\boldsymbol{P} = J\boldsymbol{\sigma}\boldsymbol{F}^{-T}, \text{ with } \boldsymbol{P} = \sum_{i,J=1}^{n} P_{iJ}\boldsymbol{e}_i \otimes \boldsymbol{E}_J, \tag{2.21}$$

in Cartesian coordinates where $\boldsymbol{E}$ are the basis unit vectors in the reference configuration. The first Piola-Kirchhoff stress, in that sense, relates the traction force in the current configuration to the corresponding differential area in the reference configuration. This implies that the traction force vector $\boldsymbol{t}_d$ in the deformed configuration (2.20) can be mapped back to into the traction force $\boldsymbol{t}$ in the reference configuration. That is

$$\boldsymbol{t} = \boldsymbol{P}\boldsymbol{N}, \tag{2.22}$$

where $\boldsymbol{N}$ is unit outward normal vector to the particle point $\boldsymbol{x}$ (the initial position of $\boldsymbol{x}_d$).

Remark: Traction force vector $\boldsymbol{t}$ defined in Equation 2.22 does not represent an actual traction force applied on point $\boldsymbol{x}$, but it represents a co-linear vector to $\boldsymbol{t}_d$ in the reference configuration.

The Second Piola-Kirchhoff Stress

As the first Piola-Kirchhoff is a two-point tensor and not completely defined in terms of quantities in the initial configuration, the *second Piola-Kirchhoff stress* tensor, a material stress tensor, is defined. This tensor is expressed in terms of the Cauchy stress and the

first Piola-Kirchhoff stress as

$$\boldsymbol{S} = J\boldsymbol{F}^{-1}\boldsymbol{\sigma}\boldsymbol{F}^{-T} = \boldsymbol{F}^{-1}\boldsymbol{P}. \tag{2.23}$$

The Kirchhoff Stress

Another stress tensor that may be important for some constitutive laws is the *Kirchhoff stress* tensor that is expressed, in terms of the previously described stress tensors, as

$$\boldsymbol{\tau} = J\boldsymbol{\sigma} = \boldsymbol{P}\boldsymbol{F}^{T} = \boldsymbol{F}\boldsymbol{S}\boldsymbol{F}^{T}. \tag{2.24}$$

2.3 Equilibrium and Principle of Virtual Work

This section deals with the equilibrium state of the continuum body. The equilibrium equations describing the motion of the body are described here, this is known as the *strong form* of the problem. This is followed by the derivation of the *weak form* of the problem, that is enforcing equilibrium in an integral form which is also known as the *Principle of Virtual Work* (PVW).

2.3.1 Translational Equilibrium

Consider again the current configuration of a deformable body illustrated in Figure 2.2. If the body is subjected a body force per unit volume $\boldsymbol{b}_d$ and a traction force per unit area $\boldsymbol{t}_d$ acting on its boundaries, for the body to be in translational equilibrium, the sum of all forces acting on the body must vanish. This can be expressed as

$$\int_{\partial\omega} \boldsymbol{t}_d \, da + \int_{\omega} \boldsymbol{b}_d \, dv = 0. \tag{2.25}$$

In view of Equation 2.20, the above relation can be modified to

$$\int_{\partial\omega} \boldsymbol{\sigma}\boldsymbol{n} \, da + \int_{\omega} \boldsymbol{b}_d \, dv = 0, \tag{2.26}$$

which, making use of the Gauss theorem, can be rewritten as

$$\int_{\omega} (\mathrm{div}_d \, \boldsymbol{\sigma} + \boldsymbol{b}_d) \, dv = 0. \tag{2.27}$$

As the above equation has to hold for any body differential volume of the body, it can be expressed as

$$\mathrm{div}_d \, \boldsymbol{\sigma} + \boldsymbol{b}_d = 0, \tag{2.28}$$

where div_d denotes divergence taken with respect to coordinates in the deformed configuration. Equation 2.28 is also known as the strong form of the equilibrium equation.

2.3.2 Rotational Equilibrium

It can be shown that the rotational equilibrium of the deformed body is satisfied by imposing symmetry over the Cauchy stress tensor, that is

$$\boldsymbol{\sigma} = \boldsymbol{\sigma}^T. \tag{2.29}$$

Relation 2.21 can hence be used to express the rotational equilibrium condition on the first Piola-kirchhoff stress, giving

$$\boldsymbol{P}\boldsymbol{F}^T = \boldsymbol{F}\boldsymbol{P}^T. \tag{2.30}$$

The lengthy derivation of Equation 2.29 is omitted for convenience and it is provided in detail in [1, 5].

2.3.3 The Principle of Virtual Work

The *Finite Element* (FE) formulation, essential for the solution of the problem of interest for the present work, requires the weak form of the equilibrium equation set up in Equation 2.28. This explains the use of the *Principle of Virtual Work* (PVW).

Let $\boldsymbol{\eta}_d$ denote an arbitrary virtual displacement in the current configuration. The PVW requires that the equilibrium is satisfied weakly in an integral form over the domain of the current configuration as

$$\delta W(\boldsymbol{u}, \boldsymbol{\eta}_d) = \int_\omega (\mathrm{div}_d\, \boldsymbol{\sigma} + \boldsymbol{b}_d) \cdot \boldsymbol{\eta}_d \; dv = 0, \tag{2.31}$$

where δW is the virtual work obtained from applying the virtual displacement. Making use of Gauss theorem and identity

$$\mathrm{div}(\boldsymbol{\eta}_d) = (\mathrm{div}\, \boldsymbol{\sigma}) \cdot \boldsymbol{\eta}_d + \boldsymbol{\sigma} : \nabla \boldsymbol{\eta}_d, \tag{2.32}$$

Equation 2.31 is manipulated into the following final form

$$\delta W(\boldsymbol{u}, \boldsymbol{\eta}_d) = \underbrace{\int_\omega \boldsymbol{\sigma} : \nabla \boldsymbol{\eta}_d \; dv}_{\delta W_{int}} \overbrace{- \int_\omega \boldsymbol{b}_d \cdot \boldsymbol{\eta}_d \; dv - \int_{\partial\omega} \boldsymbol{t}_d \cdot \boldsymbol{\eta}_d \; da}^{\delta W_{ext}} = 0, \tag{2.33}$$

where δW_{int} and δW_{ext} the internal and external virtual work respectively. It is also useful to express the weak form of the equilibrium equation in terms of the first Piola-Kirchhoff stress in the reference configuration. This gives

$$\delta W(\boldsymbol{u}, \boldsymbol{\eta}) = \underbrace{\int_\Omega \boldsymbol{P} : \nabla \boldsymbol{\eta} \; dV}_{\delta W_{int}} \overbrace{- \int_\Omega \boldsymbol{b} \cdot \boldsymbol{\eta} \; dV - \int_{\partial\Omega} \boldsymbol{t} \cdot \boldsymbol{\eta} \; dA}^{\delta W_{ext}} = 0, \tag{2.34}$$

where $\boldsymbol{\eta}$ is the virtual displacement applied in the reference configuration. In addition, the procedure used to obtain Equation 2.33 can be reversed to obtain the strong form of the equilibrium in the reference configuration, and this can be expressed as

$$\operatorname{div} \boldsymbol{P} + \boldsymbol{b} = 0. \tag{2.35}$$

2.3.4 The Boundary Value Problem

The above described equilibrium equations are required to set the *Boundary Value Problem* (BVP) to be solved. This will be formulated here in the reference configuration as it is convenient for the problem of interest for the current work. The BVP formulated in the reference configuration is expressed as follows:

> *Given the body force* $\boldsymbol{b}$ *on a body* Ω *and the traction force* $\boldsymbol{t}$ *on its boundary* $\partial\Omega$ *in the reference configuration, find a kinematically admissible displacement* $\boldsymbol{u} \in \mathscr{K}$ *such that the weak equilibrium form of the problem:*
>
> $$\int_\Omega \boldsymbol{P} : \nabla\boldsymbol{\eta}\, dV - \int_\Omega \boldsymbol{b}\cdot\boldsymbol{\eta}\, dV - \int_{\partial\Omega} \boldsymbol{t}\cdot\boldsymbol{\eta}\, dA = 0 \quad \forall\boldsymbol{\eta} \in \mathscr{V},$$
>
> *is satisfied at all times, and where* $\mathscr{K}$ *is the space of kinematically admissible displacements and* $\mathscr{V}$ *is the space of virtual kinematically admissible displacements.*

2.4 Constitutive Equations

The equilibrium equations described in 2.33 and 2.34 are expressed in terms of a measure of stress. This stress is built in the body due to the deformation of material that it is made of. The deformation as shown earlier results in strains. The relationship between stress and strain is called the *constitutive equation*. The simplest example would be the linear elastic material which is described by a linear relationship between the stress and strain as implied by *Hook's law*, through *Young's modulus*. The constitutive laws of interest for this work, describe a class of materials in finite strains known as *hyperelastic* materials. Those materials are described by a stored energy function.

In this section, the concept of hyperelasticity will be introduced, followed by the linearisation of the internal virtual work to show that the derivation of the tangent modulus of the material is essential for the solution procedure. Finally, the description of the hyperelastic materials used in this work and the derivation of the corresponding tangent moduli are provided.

2.4.1 Hyperelasticity

Materials are described by hyperelasticity if the work done by the stress in this material depends only on the initial (at t_o) and final (at t) configurations and independent of the

path of deformation. Consequently, these materials can be described by a *stored energy function* or an *elastic potential* denoted by Ψ,

$$\Psi(\boldsymbol{F}(\boldsymbol{x}), \boldsymbol{x}) = \int_{t_o}^{t} \boldsymbol{P}(\boldsymbol{F}(\boldsymbol{x}), \boldsymbol{x}) : \dot{\boldsymbol{F}} \; dt, \tag{2.36}$$

where $\dot{\boldsymbol{F}}$ is the rate of the deformation gradient. This implies that the following expression is valid,

$$\dot{\Psi} = \boldsymbol{P} : \dot{\boldsymbol{F}}. \tag{2.37}$$

Knowing the strain energy function describing the material, the first Piola-Kirchhoff stress can be expressed as

$$\boldsymbol{P} = \frac{\partial \Psi(\boldsymbol{F}(\boldsymbol{x}), \boldsymbol{x})}{\partial \boldsymbol{F}(\boldsymbol{x})}. \tag{2.38}$$

The energy function Ψ can also be expressed in terms of other measures of strain, e.g. the Cauchy-Green strain tensor. This can be written as

$$\Psi(\boldsymbol{F}(\boldsymbol{x}), \boldsymbol{x}) = \Psi(\boldsymbol{C}(\boldsymbol{x}), \boldsymbol{x}), \tag{2.39}$$

which is differentiated to obtain the second Piola-Kirchhoff stress tensor as

$$\boldsymbol{S} = 2\frac{\partial \Psi(\boldsymbol{C}(\boldsymbol{x}), \boldsymbol{x})}{\partial \boldsymbol{C}(\boldsymbol{x})}, \tag{2.40}$$

where the factor 2 is due to identity 2.12.

2.4.2 Linearisation of the Internal Virtual Work

By taking the directional derivative of the internal virtual work δW_{int} (first term in Equation 2.34) in the direction of a displacement $\Delta \boldsymbol{u}$,

$$D\delta W_{int}[\Delta \boldsymbol{u}] = \int_{\Omega_\mu^s} D(\boldsymbol{P} : \nabla \boldsymbol{\eta})[\Delta \boldsymbol{u}] \; dV, \tag{2.41}$$

and noticing that the virtual displacement $\boldsymbol{\eta}$ does not depend on the displacement $\Delta \boldsymbol{u}$, Equation (4.1) can be simplified to

$$D\delta W_{int}[\Delta \boldsymbol{u}] = \int_{\Omega} D(\boldsymbol{P})[\Delta \boldsymbol{u}] : \nabla \boldsymbol{\eta} \; dV. \tag{2.42}$$

The stress $\boldsymbol{P}$ depends on the deformation gradient which, in turn, depends on the displacement $\boldsymbol{u}$, hence $\boldsymbol{P}$ can be expressed as $\boldsymbol{P}(\boldsymbol{F}(\boldsymbol{u}))$. Hence, Equation 2.42 can be modified to

$$\begin{aligned} D\delta W_{int}[\Delta \boldsymbol{u}] &= \int_{\Omega} \frac{\partial \boldsymbol{P}}{\partial \boldsymbol{F}} : \nabla(\Delta \boldsymbol{u}) : \nabla \boldsymbol{\eta} \; dV, \\ &= \int_{\Omega} \mathbf{A} : \nabla(\Delta \boldsymbol{u}) : \nabla \boldsymbol{\eta} \; dV, \end{aligned} \tag{2.43}$$

where $\mathbf{A}$ is the fourth order material tangent modulus depending on the constitutive model used.

2.4.3 Constitutive Model and Derivation of the Material Tangent Modulus

The constitutive models used in the present work are described in following in addition to the corresponding derivation of the material tangent modulus. These are the compressible and incompressible Neo-Hookean material model, and the Hencky model.

The Neo-Hookean Models

The *Neo-Hookean* material models are of particular importance for describing rubber-like materials, they are relatively simple compared to other models (e.g. the Mooney-Rivlin model) [5]. The *compressible* and the *incompressible Neo-Hookean* models are described in the following.

a. **The compressible Neo-Hookean model** is characterized by material parameters similar to those used to describe the linear elastic material, namely the *lamé parameters*, λ and μ. The energy function describing this material is

$$\Psi = \frac{\mu}{2}\left(\operatorname{tr}\boldsymbol{C} - 3\right) - \mu \ln J + \frac{\lambda}{2}\left(\ln J\right)^2 . \tag{2.44}$$

Equation 2.38 is then used to obtain a form of the first Piola-Kirchhoff stress describing this material, and this can be written as

$$\boldsymbol{P} = \mu(\boldsymbol{F} - \boldsymbol{F}^{-\boldsymbol{T}}) + \lambda(\ln\ J)\boldsymbol{F}^{-\boldsymbol{T}}. \tag{2.45}$$

The corresponding material tangent modulus $\mathbf{A}$ is thus derived as

$$\begin{aligned}
\mathsf{A}_{ijkl} &= \frac{\partial P_{ij}}{\partial F_{kl}} \\
&= \mu\frac{\partial F_{ij}}{\partial F_{kl}} - \mu\frac{\partial F^{-1}_{ji}}{\partial F_{kl}} + \lambda\frac{\partial(\ln\ J)}{\partial J}\frac{\partial(\det(\boldsymbol{F}))}{\partial F_{kl}}F^{-1}_{ji} + \lambda(\ln\ J)\frac{\partial F^{-1}_{ji}}{\partial F_{kl}} \\
&= \mu\ \delta_{ik}\delta_{jl} + \mu\ F^{-1}_{jk}F^{-1}_{li} + \lambda\left(\frac{1}{J}\right)JF^{-1}_{lk}F^{-1}_{ji} - \lambda(\ln\ J)F^{-1}_{jk}F^{-1}_{li} \\
&= \mu\ \delta_{ik}\delta_{jl} + (\mu - \lambda(\ln\ J))\,F^{-1}_{jk}F^{-1}_{li} + \lambda F^{-1}_{lk}F^{-1}_{ji},
\end{aligned} \tag{2.46}$$

which can be written, in tensor notation, as

$$\mathbf{A} = \mu\mathbf{I} + \lambda\boldsymbol{F}^{-\boldsymbol{T}} \otimes \boldsymbol{F}^{-\boldsymbol{T}} + (\mu - \lambda(\ln\ J))\,\frac{\partial \boldsymbol{F}^{-\boldsymbol{T}}}{\partial \boldsymbol{F}}, \tag{2.47}$$

where $\mathbf{I}$ is the fourth order identity tensor.

b. **The incompressible Neo-Hookean model** is of practical use, as the case for other incompressible materials, in finite strains, specially when plasticity is involved

[5]. Incompressibility denotes that there are no volume changes involved in the deformation, that is $J = 1$. Enforcing this condition on Equation 2.44, the energy function of this material is given as

$$\Psi = \frac{\mu}{2} \left(\operatorname{tr} \boldsymbol{C} - 3 \right). \tag{2.48}$$

The numerical treatment of incompressibility is done by imposing a small volumetric deformation to the problem and ending up with a *nearly-incompressible* material. The procedure provided in [1] is followed here to obtain the nearly-incompressible Neo-Hookean energy function. The strain energy function describing this material consists of two components: a distortional part ($\hat{\Psi}$) and a volumetric part ($U(J)$),

$$\Psi = \hat{\Psi} + U(J). \tag{2.49}$$

The distortional energy function is proven in [1] to have the same format as Equation 2.48 using the distortional part of the strain, that is

$$\hat{\Psi} = \frac{\mu}{2} \left(\operatorname{tr} \hat{\boldsymbol{C}} - 3 \right), \tag{2.50}$$

where $\hat{\boldsymbol{C}} = J^{-\frac{2}{3}} \boldsymbol{C}$. A simple form of volumetric energy can also be used which is given as

$$U(J) = \frac{1}{2} \kappa (J - 1)^2, \tag{2.51}$$

where κ is a large penalty number in the range $10^3 - 10^4$ used to enforce incompressibility, but it can denote as well a real material parameter like the bulk modulus. Equations 2.49, 2.50 and 2.51 are then used to obtain the final form used for the first Piola-Kirchhoff stress which can be written as

$$\boldsymbol{P} = \mu J^{-\frac{2}{3}} \left(\boldsymbol{F} - \frac{1}{3} \left(\operatorname{tr} \boldsymbol{C} \right) \boldsymbol{F}^{-T} \right) + \kappa J (J - 1) \boldsymbol{F}^{-T}. \tag{2.52}$$

Finally, the material tangent modulus can be derived as follows,

$$\begin{aligned}
\mathsf{A}_{ijkl} &= \frac{\partial P_{ij}}{\partial F_{kl}} \\
&= \mu J^{-\frac{2}{3}} \left(\frac{\partial F_{ij}}{\partial F_{kl}} - \frac{1}{3} \left(\operatorname{tr} \boldsymbol{C} \right) \frac{\partial F^{-1}_{ji}}{\partial F_{kl}} - \frac{1}{3} F^{-1}_{ji} \frac{\partial \left(\operatorname{tr} \boldsymbol{C} \right)}{\partial F_{kl}} \right) \\
&- \frac{2}{3} \mu \left(F_{ij} - \frac{1}{3} \left(\operatorname{tr} \boldsymbol{C} \right) F^{-1}_{ji} \right) \frac{\partial J}{\partial F_{kl}} \\
&+ \kappa J (J-1) \frac{\partial F^{-1}_{ji}}{\partial F_{kl}} + \kappa (2J-1) F^{-1}_{ji} \frac{\partial J}{\partial F_{kl}}, \\
&= \mu J^{-\frac{2}{3}} \left(\delta_{ik} \delta_{jl} + \frac{1}{3} \left(\operatorname{tr} \boldsymbol{C} \right) F^{-1}_{jk} F^{-1}_{li} - \frac{2}{3} F^{-1}_{ji} F_{kl} \right) \\
&- \frac{2}{3} \mu J^{-\frac{2}{3}} \left(F_{ij} - \frac{1}{3} \left(\operatorname{tr} \boldsymbol{C} \right) F^{-1}_{ji} \right) F^{-1}_{lk} \\
&- \kappa J (J-1) F^{-1}_{jk} F^{-1}_{li} + \kappa J (2J-1) F^{-1}_{ji} F^{-1}_{lk}.
\end{aligned} \tag{2.53}$$

In tensor notation, Equation 2.53 can be written as

$$\begin{aligned}
\mathbf{A} &= \mu J^{-\frac{2}{3}} \mathbf{I} + \left(\frac{1}{3} \mu J^{-\frac{2}{3}} \left(\operatorname{tr} \boldsymbol{C} \right) - \kappa J (J-1) \right) \boldsymbol{F}^{-\boldsymbol{T}} \otimes \boldsymbol{F}^{-\boldsymbol{T}} \\
&- \frac{2}{3} \mu J^{-\frac{2}{3}} \left(\boldsymbol{F}^{-\boldsymbol{T}} \otimes \boldsymbol{F} + \boldsymbol{F} \otimes \boldsymbol{F}^{-\boldsymbol{T}} \right) \\
&+ \left(\frac{2}{9} \mu J^{-\frac{2}{3}} \left(\operatorname{tr} \boldsymbol{C} \right) + \kappa J (2J-1) \right) \frac{\partial \boldsymbol{F}^{-\boldsymbol{T}}}{\partial \boldsymbol{F}}.
\end{aligned} \tag{2.54}$$

The Hencky Model

The *Hencky* model is particularly useful in describing vulcanized-rubber. In addition, it becomes crucial for elasto-plastic formulation in finite strains. This is due to the similarities between the energy function describing it and that describing the linear elastic material. The detailed description of the Hencky model is provided in [5]. It is defined in terms of the *Eulerian logarithmic strain* $\boldsymbol{\varepsilon}^l$ which is defined as

$$\boldsymbol{\varepsilon}^l \equiv \ln \boldsymbol{V} = \frac{1}{2} \ln \boldsymbol{B}. \tag{2.55}$$

The strain energy function describing this material is expressed as

$$\Psi = \frac{1}{2} \boldsymbol{\varepsilon}^l : \mathbf{D} : \boldsymbol{\varepsilon}^l, \tag{2.56}$$

where $\mathbf{D}$ is the fourth order elasticity tensor having the same format as the small strain elasticity tensor. It is given as

$$\mathbf{D} = 2\mu \mathbf{I}_S + \lambda \boldsymbol{I} \otimes \boldsymbol{I}, \tag{2.57}$$

where I_S is the fourth order symmetric identity tensor and its Cartesian components (as defined in [5]) are

$$\mathsf{I}_{Sijkl} = \frac{1}{2}(\delta_{ik}\delta_{jl} + \delta_{il}\delta_{jk}). \tag{2.58}$$

Tensor $\mathbf{D}$ can be written, in Cartesian components, as

$$\mathsf{D}_{ijkl} = \mu(\delta_{ik}\delta_{jl} + \delta_{il}\delta_{jk}) + \lambda\delta_{ij}\delta_{kl}. \tag{2.59}$$

The Kirchhoff stress can be expressed, as a function of $\boldsymbol{\varepsilon}^l$, as

$$\boldsymbol{\tau} = 2\mu\boldsymbol{\varepsilon}^l + \lambda(\mathrm{tr}\boldsymbol{\varepsilon}^l)\boldsymbol{I}, \tag{2.60}$$

which has the same format as the stress describing the linear elastic isotropic material. In light of Equation 2.24, the material tangent modulus $\mathbf{A}$ is obtained as

$$\begin{aligned}
\mathsf{A}_{ijkl} &= \frac{\partial P_{ij}}{\partial F_{kl}} \\
&= \frac{\partial \tau_{im}}{\partial F_{kl}} F^{-1}_{jm} + \tau_{im}\frac{\partial F^{-1}_{im}}{\partial F_{kl}} \\
&= \frac{1}{2}\left(\frac{\partial \boldsymbol{\tau}}{\partial \boldsymbol{\varepsilon}} : \frac{\partial \boldsymbol{\varepsilon}}{\partial \boldsymbol{B}} : \frac{\partial \boldsymbol{B}}{\partial \boldsymbol{F}}\right)_{imkl} F^{-1}_{jm} - \tau_{im}F^{-1}_{jk}F^{-1}_{lm} \\
&= \frac{1}{2}\left(\mathbf{D} : \mathbf{L} : \bar{\mathbf{F}}\right)_{imkl} F^{-1}_{jm} - P_{il}F^{-1}_{jk} \\
&= \bar{\mathsf{C}}_{ijkl} - \bar{\mathsf{P}}_{ijkl},
\end{aligned} \tag{2.61}$$

The components of $\bar{\mathsf{C}}_{ijkl}$ are obtained as follows:

- The fourth order tensor $\mathbf{L}$ represents the derivative of the tensor logarithmic function of $\boldsymbol{B}$. As the tensor logarithmic function falls in the class of isotropic functions described in Appendix A in [5], it can be expressed as

$$\mathsf{L}_{ijkl} = \begin{cases} \frac{\ln b_1 - \ln b_2}{b_1 - b_2}\left(\frac{1}{2}(\delta_{ik}\delta_{jl} + \delta_{il}\delta_{jk}) - E_{1ij}E_{1kl} - E_{2ij}E_{2kl}\right) & \\ \quad + \frac{1}{b_1}E_{1ij}E_{1kl} + \frac{1}{b_2}E_{2ij}E_{2kl} & \text{if } b_1 \neq b_2, \\ \frac{1}{2b_1}(\delta_{ik}\delta_{jl} + \delta_{il}\delta_{jk}) & \text{if } b_1 = b_2, \end{cases} \tag{2.62}$$

  where b_1 and b_2 are the eigenvalues of $\boldsymbol{B}$, E_1 and E_2 are the eigenprojections of $\boldsymbol{B}$.

- The fourth order tensor $\bar{\mathbf{F}}$ denotes the derivative of $\boldsymbol{B}$ with respect to $\boldsymbol{F}$ and can be

obtained as

$$\begin{aligned}\bar{\mathsf{F}}_{ijkl} &= \frac{\partial B_{ij}}{\partial F_{kl}} \\ &= \frac{\partial}{\partial F_{kl}}(F_{im}F_{jm}) \\ &= \frac{\partial F_{im}}{\partial F_{kl}}F_{jm} + F_{im}\frac{\partial F_{jm}}{\partial F_{kl}} \\ &= \delta_{ik}\delta_{ml}F_{jm} + F_{im}\delta_{jk}\delta_{ml} \\ &= \delta_{ik}F_{jl} + F_{il}\delta_{jk}. \end{aligned} \tag{2.63}$$

2.5 Finite Element Approximation

The BVP described in Section 2.3.4 is approximated using a FE discretization applied to both spaces $\mathscr{K}$ and $\mathscr{V}$. This is done by dividing the reference configuration Ω into a total of N elements giving a discretized domain Ω^h, for a given discretization h. Consequently, a position $\boldsymbol{x}$ belonging to an element e can be expressed as

$$\boldsymbol{x} = \sum_{a=1}^{n} \boldsymbol{N}_a^{(e)}\boldsymbol{x}_a = \boldsymbol{N}_a^{(e)}\boldsymbol{x}_a, \tag{2.64}$$

where $\boldsymbol{N}_a^{(e)}$ are the shape functions describing element e, $\boldsymbol{x}_a$ are the element nodal coordinates, n is the number of nodes per element, and the second equality is based on the Einstein notation. This discretizes the space $\mathscr{K}$ into $\mathscr{K}^h$. Similarly, the space of virtual displacements $\mathscr{V}_\mu$ can be discretized into $\mathscr{V}_\mu^h$, and the virtual displacement $\boldsymbol{\eta}$ and its gradient are also discretized as

$$\boldsymbol{\eta} = \boldsymbol{N}_a^{(e)}\boldsymbol{\eta}_a \text{ and } \nabla\boldsymbol{\eta} = \boldsymbol{G}_a^{(e)}\boldsymbol{\eta}_a, \tag{2.65}$$

where $\boldsymbol{G}_a^{(e)}$ is the associated local non-symmetric gradient matrix at node a.

Based on that, the components of the equilibrium equation 2.33 can be discretized, for element e, in the same manner:

$$\delta W_{int}^{e,h} = \underbrace{\sum_{a=1}^{n}\left\{\int_{\Omega^e}\boldsymbol{G}_a^T\boldsymbol{P}\,dV\right\}}_{\mathbb{T}^e}\cdot\boldsymbol{\eta}_a, \text{ and} \tag{2.66}$$

$$\delta W_{ext}^{e,h} = \underbrace{\sum_{a=1}^{n}\left\{\int_{\Omega^e}\boldsymbol{N}_a^T\boldsymbol{b}\,dV + \int_{\partial\Omega^e}\boldsymbol{N}_a^T\boldsymbol{t}\,dA\right\}}_{\mathbb{F}^e}\cdot\boldsymbol{\eta}_a, \tag{2.67}$$

where $\mathbb{T}^e$ and $\mathbb{F}^e$ are the internal and external nodal force vectors associated with element e respectively. A FE assembly is then performed to obtain global internal and external

force vectors, which are expressed as

$$\mathbb{T} = \bigcup_{e=1}^{N} \mathbb{T}^e \text{ and } \mathbb{F} = \bigcup_{e=1}^{N} \mathbb{F}^e, \tag{2.68}$$

where $\bigcup_{e=1}^{N}$ denotes the finite element assembly of the elemental vectors and matrices. The discretized virtual work can be given in terms of the internal and external force vectors as

$$\delta W^h = \mathbb{R} \cdot \left(\bigcup_{e=1}^{N} \sum_{a=1}^{n} \boldsymbol{\eta}_a \right) = 0 \tag{2.69}$$

where $\mathbb{R}$ is the global residual vector and it is equivalent to

$$\mathbb{R} = \mathbb{T} - \mathbb{F}. \tag{2.70}$$

2.6 Newton-Raphson Solution

The BVP described in Section 2.3.4 is generally non-linear and its solution requires the use of iterative methods of the linearised version of the problem, in particular, the *Newton-Raphson* (N-R) interative method.

First of all the weak equilibrium equation in the reference configuration (2.34) is linearised as

$$\delta W(\boldsymbol{u}, \boldsymbol{\eta}) + D\delta W(\boldsymbol{u}, \boldsymbol{\eta})[\Delta \boldsymbol{u}] = 0, \tag{2.71}$$

where $D\delta W(\boldsymbol{u}, \boldsymbol{\eta})[\Delta \boldsymbol{u}]$ is the directional derivative of the virtual work in the direction of a $\Delta \boldsymbol{u}$. This can be discretized and solved iteratively using a N-R algorithm. For an iteration k, Equation 2.71 is dicretized as

$$\mathbb{R}^{(k)} \approx \mathbb{R}^{(k-1)} + D\mathbb{R}^{(k-1)}[\Delta \boldsymbol{u}^{(k)}] = 0, \tag{2.72}$$

The directional derivative of the global residual vector is commonly referred to as the global tangent stiffness matrix $\mathbb{K}$. Equation 2.72 can thus be rewritten as

$$\mathbb{R}^{(k)} \approx \mathbb{R}^{(k-1)} + \mathbb{K}^{(k-1)} \Delta \boldsymbol{u}^{(k)} = 0. \tag{2.73}$$

The N-R procedure provides the solution for the linear system of equations

$$\mathbb{K}^{(k-1)} \Delta \boldsymbol{u}^{(k)} = -\mathbb{R}^{(k-1)}, \tag{2.74}$$

as $\Delta \boldsymbol{u}^{(k)}$ that is finally used to update the displacement vector

$$\boldsymbol{u}^{(k)} \Leftarrow \boldsymbol{u}^{(k-1)} + \Delta \boldsymbol{u}^{(k)}. \tag{2.75}$$

Chapter 3

Homogenization: Finite Strain Formulation

The family of multi-scale theory of interest for the present work is based on describing the heterogeneous (macro-) continuum using a typical boundary value problem. The constitutive response at each point of the macro-continuum is obtained by homogenizing the behavior of a locally attached *Representative Volume Element* (RVE). This RVE represents the local microstructure of the corresponding point in the macro-continuum to which it is attached. The kinematical variational framework of the homogenization-based multi-scale theory, as proposed by [4], can be expressed in an axiomatic manner based on the following concepts,

- the equilibrium of the RVE,
- relating the macroscopic and microscopic deformation gradients and stresses through volume averages,
- the *additive split* of the microscopic displacement defining the constraint on the kinematically admissible displacements of the RVE, and,
- the *Hill-Mandel Principle of Macro-homogeneity* [9, 23].

This chapter starts by describing the equilibrium equations of the macro-continuum and the microstructure at the reference configuration, then moving to the coupling of scales. This introduces the homogenization of the deformation gradient and the stress, an essential aspect in the formulation of the multi-scale theory which is the Hill-Mandel Principle of Macro-homogeneity, and finally, the additive split of the microscopic displacement. For a well-posed problem, the kinematical constraints that can be imposed on the RVE are introduced and this, consequently, defines different multi-scale models.

3.1 Equilibrium Equations in the Reference Configuration

This section describes the equilibrium equations of the macro-continuum and the microstructure locally attached to it. These are all formulated in the reference configuration and used later to formulate the BVP to be solved.

3.1.1 Equilibrium of the Macro-continuum

Let $\bar{\Omega}$ denote the initial marco-continuum domain, subjected to a deformation described by a deformation gradient $\bar{\boldsymbol{F}} = \nabla\bar{\boldsymbol{\varphi}}$, where $\bar{\boldsymbol{\varphi}}$ is the deformation mapping between initial and deformed configurations of the macro-continuum as illustrated in Figure 3.1. The initial macroscopic domain $\bar{\Omega}$ is subjected to a body force per unit volume $\bar{\boldsymbol{b}} = \bar{\boldsymbol{b}}(\boldsymbol{x}, t)$ and a boundary traction per unit area $\bar{\boldsymbol{t}} = \bar{\boldsymbol{t}}(\boldsymbol{x}, t)$. According to the PVW, the macro-continuum is in equilibrium if and only if

$$\int_{\bar{\Omega}} \bar{\boldsymbol{P}}(\boldsymbol{x}, t) : \nabla\bar{\boldsymbol{\eta}} \; d\bar{V} - \int_{\bar{\Omega}} \bar{\boldsymbol{b}}(\boldsymbol{x}, t) \cdot \bar{\boldsymbol{\eta}} \; d\bar{V} - \int_{\partial\bar{\Omega}} \bar{\boldsymbol{t}}(\boldsymbol{x}, t) \cdot \bar{\boldsymbol{\eta}} \; d\bar{A} = 0 \quad \forall \bar{\boldsymbol{\eta}} \in \bar{\mathscr{V}} \tag{3.1}$$

holds for any time t, where $\bar{\boldsymbol{P}}$ is the first Piola-Kirchhoff stress tensor and $\bar{\mathscr{V}}$ is the space of virtual kinematically admissible displacements ($\bar{\boldsymbol{\eta}}$) of the macro-continuum. Equation 3.1 can be equivalently expressed in strong form as

$$\begin{cases} \operatorname{div} \bar{\boldsymbol{P}}(\boldsymbol{x}, t) = \bar{\boldsymbol{b}}(\boldsymbol{x}, t) & \text{on } \bar{\Omega}, \text{ and} \\ \bar{\boldsymbol{P}}(\boldsymbol{x}, t)\bar{\boldsymbol{N}} = \bar{\boldsymbol{t}}(\boldsymbol{x}, t) & \text{on } \partial\bar{\Omega}, \end{cases} \tag{3.2}$$

where $\bar{\boldsymbol{N}}$ is the outward normal to the boundary of macro-continuum $\partial\bar{\Omega}$. The boundary conditions for the deformation and traction are

$$\bar{\boldsymbol{\varphi}} = \bar{\boldsymbol{\varphi}}_b \text{ on } \partial\bar{\Omega}_d \quad \text{and} \quad \bar{\boldsymbol{t}} := \bar{\boldsymbol{P}}\bar{\boldsymbol{N}} = \bar{\boldsymbol{t}}_b \text{ on } \partial\bar{\Omega}_f,$$

where the decomposition of the surface of macro-continuum $\partial\bar{\Omega} = \partial\bar{\Omega}_d \cup \partial\bar{\Omega}_f$ and $\partial\bar{\Omega}_d \cap \partial\bar{\Omega}_f = \emptyset$ is considered. It is to be noted that all gradient operators are evaluated in the reference configuration.

3.1.2 Equilibrium of the Representative Volume Element

Let Ω_μ denote the *Representative Volume Element* (RVE) composed of a solid phase and a void phase ($\Omega_\mu = \Omega_\mu^s \cup \Omega_\mu^v$), subjected to a body force $\boldsymbol{b}$, and an external traction $\boldsymbol{t}^e$ along its boundaries $\partial\Omega_\mu$. The RVE is subjected to a deformation gradient $\boldsymbol{F}_\mu = \nabla\boldsymbol{\varphi}$ that relates initial ($\boldsymbol{y}$) and current ($\boldsymbol{y}_d$) particle positions. The PVW provides the weak form

of the equilibrium of the RVE which can be written, in the reference configuration, as

$$\int_{\Omega_\mu^s} \boldsymbol{P_\mu}(\boldsymbol{y},t) : \nabla\boldsymbol{\eta}\ dV - \int_{\Omega_\mu^s} \boldsymbol{b}(\boldsymbol{y},t)\cdot\boldsymbol{\eta}\ \ dV - \int_{\partial\Omega_\mu^s} \boldsymbol{t^e}(\boldsymbol{y},t)\cdot\boldsymbol{\eta}\ \ dA = 0 \quad \forall\boldsymbol{\eta}\in\mathscr{V}_\mu, \tag{3.3}$$

where $\mathscr{V}_\mu$ is the space of virtual kinematically admissible microscopic displacements $\boldsymbol{\eta}$. The strong form of Equation 3.3 can expressed as

$$\begin{cases} \operatorname{div}\boldsymbol{P_\mu}(\boldsymbol{y},t) = \boldsymbol{b}(\boldsymbol{y},t) & \text{on } \Omega_\mu, \text{ and} \\ \boldsymbol{P_\mu}(\boldsymbol{y},t)\boldsymbol{N} = \boldsymbol{t^e}(\boldsymbol{y},t) & \text{on } \partial\Omega_\mu, \end{cases} \tag{3.4}$$

where $\boldsymbol{N}$ is the outward normal to the surface of the RVE $\partial\Omega_\mu$. The integral is defined over the solid phase ($\Omega_\mu^s \subset \Omega_\mu$) as deformation is not defined over the void phase [4]. For simplicity, the considered RVEs for the present work are limited to those with no intersection between the void phase and the boundaries of the RVE. It should be noted that it is assumed in Equation 3.3 that no traction forces exist across the solid/void interface.

The deformation of the RVE is driven by the macroscopic deformation gradient $\bar{\boldsymbol{F}}$ [25]. It is noteworthy that the microscopic deformation gradient $\boldsymbol{F_\mu}$ is related to $\bar{\boldsymbol{F}}$ through homogenization theory as will be described in detail in following section.

3.2 Micro-to-Macro Transitions: Homogenized Properties

Coupling of scales is introduced in this section. Some homogenized properties are provided here, namely, deformation gradient, stress, and stress power based on the Hill-Mandel principle. Finally, the additive split of the microscopic displacement field is described.

3.2.1 Homogenized Deformation Gradient

The first concept in defining the kinematical variational framework of the multi-scale theory is relating the macroscopic and microscopic deformation gradients. The assumption made is that at any time t, the macroscopic deformation gradient $\bar{\boldsymbol{F}}$ at a point $\boldsymbol{x}$ on the macro-continuum is the volume average of the microscopic deformation gradient $\boldsymbol{F_\mu}$ defined on the RVE attached to $\boldsymbol{x}$:

$$\bar{\boldsymbol{F}}(\boldsymbol{x},t) \equiv \frac{1}{V_\mu}\int_{\Omega_\mu^s} \boldsymbol{F_\mu}(\boldsymbol{y},t)\ dV, \tag{3.5}$$

where $\boldsymbol{y}$ is the local coordinate in Ω_μ, and $V_\mu := \operatorname{vol}(\Omega_\mu)$ is the volume of the RVE in its initial configuration. It is to be noted that the integration is done over the solid domain as the microscopic displacement is not defined over the void phase [4].

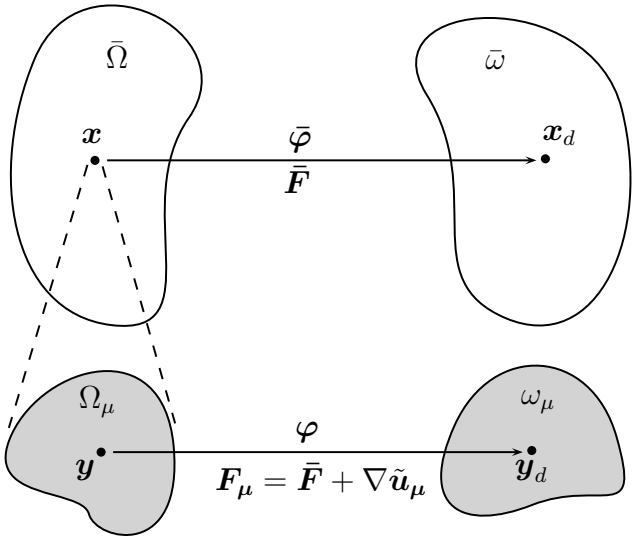

Figure 3.1: Deformation of the macro-continuum and the microstructure with $(\bar{\boldsymbol{\varphi}}, \bar{\boldsymbol{F}})$ and $(\boldsymbol{\varphi}, \boldsymbol{F_\mu})$ being the deformation mappings and the deformation gradients of the macro-continuum and microsturcture, respectively. The initial and final configurations of the macro-continuum are $(\bar{\Omega}, \bar{\omega})$ respectively. The corresponding configurations for the microstructure are (Ω_μ, ω_μ). A microstructure Ω_μ is locally attached to $\boldsymbol{x}$ on the initial macro-continuum.

According to the definition of the deformation gradient tensor (see Equation 2.3), Equation 3.5 can be simplified to

$$\begin{aligned}\bar{\boldsymbol{F}}(\boldsymbol{x}, t) &= \frac{1}{V_\mu}\int_{\Omega_\mu^s} \left[\boldsymbol{I} + \nabla \boldsymbol{u_\mu}(\boldsymbol{y}, t)\right]\, dV \\ &= \boldsymbol{I} + \frac{1}{V_\mu}\int_{\Omega_\mu^s} \nabla \boldsymbol{u_\mu}(\boldsymbol{y}, t)\, dV \qquad (3.6) \\ &= \boldsymbol{I} + \frac{1}{V_\mu}\int_{\partial\Omega_\mu^s} \boldsymbol{u_\mu}(\boldsymbol{y}, t) \otimes \boldsymbol{N}(\boldsymbol{y})\, dA, \qquad (3.7)\end{aligned}$$

where $\boldsymbol{N}$ is the outward normal to the RVE, and the Green's theorem is used to obtain Equation 3.7.

3.2.2 Homogenized Stress

Similar to the homogenized deformation gradient, the homogenized first Piola-Kirchhoff stress tensor $\bar{\boldsymbol{P}}$ is defined, at any time t, as the volume average of the microscopic first

Piola-Kirchhoff stress $\boldsymbol{P_\mu}$ over the RVE:

$$\bar{\boldsymbol{P}}(\boldsymbol{x},t) \equiv \frac{1}{V_\mu}\int_{\Omega^s_\mu} \boldsymbol{P_\mu}(\boldsymbol{y},t)\; dV. \tag{3.8}$$

This also applies to other measures of stress, Cauchy stress $\boldsymbol{\sigma}_\mu$, the second Piola-Kirchhoff stress $\boldsymbol{S}_\mu$ and the Kirchhoff stress $\boldsymbol{\tau}_\mu$ with the corresponding volume of the RVE (whether it is initial or deformed RVE volume).

Generaly, the stress is related to the deformation gradient via the constitutive behavior of the material of the point studied. That is, the constitutive behavior sets the relation

$$\boldsymbol{P_\mu} = \mathfrak{F}(\boldsymbol{F_\mu}) \tag{3.9}$$

that holds for any point $\boldsymbol{y}$. In the above relation, $\mathfrak{F}$ denotes a generic constitutive functional which, for example, can be the derivative of an energy function for hyperelastic materials or can include internal variables for elasto-plastic materials.

Remark: In general, the transformations between spatial volume-averaged stresses (e.g. Cauchy stress) and material volume-averaged stresses (e.g. first Piola-Kirchhoff stress) are not necessarily the same as the conventional relationships linking stresses on the microscopic level. This is due to the nonlinearity in the relations linking them [29]. The conditions for which this holds are provided in [4].

3.2.3 Additive Split of the Microscopic Displacement Field

Critical to the formulation of the multi-scale theory is the split of the microscopic displacement field into a sum

$$\boldsymbol{u_\mu} = \bar{\boldsymbol{u}} + \tilde{\boldsymbol{u}}_\mu = \left[\bar{\boldsymbol{F}}(\boldsymbol{x},t) - \boldsymbol{I}\right]\boldsymbol{y} + \tilde{\boldsymbol{u}}_\mu \tag{3.10}$$

of a homogeneous displacement $\bar{\boldsymbol{u}}$ that is due to the macroscopic deformation and a displacement fluctuation $\tilde{\boldsymbol{u}}_\mu$. This split is illustrated in Figure 3.2. The displacement $\bar{\boldsymbol{u}}$ varies linearly in $\boldsymbol{y}$ and is homogeneous over the entire RVE while the displacement fluctuation $\tilde{\boldsymbol{u}}_\mu$ accounts for the deformation occurring at the RVE level and does not contribute to the overall deformation of the macro-continuum. Accordingly, the microscopic deformation gradient can be expressed as follows, using the definition of the deformation gradient,

$$\boldsymbol{F_\mu} = \boldsymbol{I} + \nabla\boldsymbol{u_\mu} = \bar{\boldsymbol{F}} + \nabla\tilde{\boldsymbol{u}}_\mu. \tag{3.11}$$

The displacement fluctuation field is essential for defining the space of virtual kinematically admissible displacements as will be described in Section 3.3 and hence the linearisation of the equilibrium equation 3.3 to be solved using Finite Element methods (see Chapter 4).

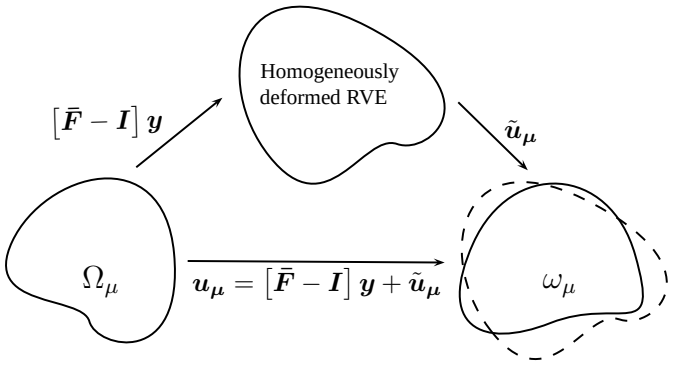

Figure 3.2: Additive split of the microscopic displacement field.

3.2.4 The Hill-Mandel Principle of Macro-homogeneity

The *Hill-Mandel Principle of Macro-homogeneity* [9, 23] is another fundamental concept in formulating the framework of the multi-scale theory. It requires the macroscopic stress power to be equal to the volume average microscopic stress power over the RVE for any kinematically admissible motion of the RVE. Consequently, for any equilibrium state of the RVE,

$$\bar{\boldsymbol{P}} : \dot{\bar{\boldsymbol{F}}} = \frac{1}{V_\mu} \int_{\Omega_\mu^s} \boldsymbol{P}_{\boldsymbol{\mu}} : \dot{\boldsymbol{F}}_{\boldsymbol{\mu}}\, dV \tag{3.12}$$

must hold for any kinematically admissible deformation gradient rate field $\dot{\boldsymbol{F}}_{\boldsymbol{\mu}}$. According to the additive split 3.11,

$$\dot{\boldsymbol{F}}_{\boldsymbol{\mu}} = \dot{\bar{\boldsymbol{F}}} + \nabla \dot{\tilde{\boldsymbol{u}}}_{\boldsymbol{\mu}}, \tag{3.13}$$

which is substituted back in the right hand side of Equation 3.12. This leads to

$$\begin{aligned} \bar{\boldsymbol{P}} : \dot{\bar{\boldsymbol{F}}} &= \frac{1}{V_\mu} \int_{\Omega_\mu^s} \boldsymbol{P}_{\boldsymbol{\mu}} : \dot{\bar{\boldsymbol{F}}} + \frac{1}{V_\mu} \int_{\Omega_\mu^s} \boldsymbol{P}_{\boldsymbol{\mu}} : \nabla \dot{\tilde{\boldsymbol{u}}}_{\boldsymbol{\mu}}\, dV, \\ &= \bar{\boldsymbol{P}} : \dot{\bar{\boldsymbol{F}}} + \frac{1}{V_\mu} \int_{\Omega_\mu^s} \boldsymbol{P}_{\boldsymbol{\mu}} : \nabla \dot{\tilde{\boldsymbol{u}}}_{\boldsymbol{\mu}}\, dV, \end{aligned} \tag{3.14}$$

which implies that

$$\int_{\Omega_\mu^s} \boldsymbol{P}_{\boldsymbol{\mu}} : \nabla \dot{\tilde{\boldsymbol{u}}}_{\boldsymbol{\mu}}\, dV = 0 \;\forall \dot{\tilde{\boldsymbol{u}}}_{\boldsymbol{\mu}} \in \mathscr{V}_\mu. \tag{3.15}$$

By applying the integration by parts to the left hand side of Equation 3.15,

$$\int_{\partial\Omega_\mu^s} (\boldsymbol{P_\mu N}) \cdot \dot{\tilde{\boldsymbol{u}}}_{\boldsymbol{\mu}} dA - \int_{\Omega_\mu^s} (\operatorname{div} \boldsymbol{P_\mu}) \cdot \dot{\tilde{\boldsymbol{u}}}_{\boldsymbol{\mu}} dV = 0 \ \forall \dot{\tilde{\boldsymbol{u}}}_{\boldsymbol{\mu}} \in \mathscr{V}_\mu \tag{3.16}$$

can be obtained. In view of the strong form of the equilibrium equation 3.4, Equation 3.16 can be expressed as

$$\int_{\partial\Omega_\mu^s} \boldsymbol{t^e} \cdot \dot{\tilde{\boldsymbol{u}}}_{\boldsymbol{\mu}} dA - \int_{\Omega_\mu^s} \boldsymbol{b} \cdot \dot{\tilde{\boldsymbol{u}}}_{\boldsymbol{\mu}} dV = 0 \ \forall \dot{\tilde{\boldsymbol{u}}}_{\boldsymbol{\mu}} \in \mathscr{V}_\mu. \tag{3.17}$$

Since the space $\mathscr{V}_\mu$ is a vector space, as will be described in Section 3.3, Equation 3.17 holds if and only if

$$\int_{\partial\Omega_\mu^s} \boldsymbol{t^e} \cdot \dot{\tilde{\boldsymbol{u}}}_{\boldsymbol{\mu}} dA = 0 \text{ and } \int_{\Omega_\mu^s} \boldsymbol{b} \cdot \dot{\tilde{\boldsymbol{u}}}_{\boldsymbol{\mu}} dV = 0 \ \forall \dot{\tilde{\boldsymbol{u}}}_{\boldsymbol{\mu}} \in \mathscr{V}_\mu.$$

This provides an equivalent variational expression of the Hill-Mandel principle which reduces the equilibrium equation 3.3 to

$$\int_{\Omega_\mu^s} \boldsymbol{P_\mu}(\boldsymbol{y}, t) : \nabla \boldsymbol{\eta} \ dV = 0 \ \forall \boldsymbol{\eta} \in \mathscr{V}_\mu. \tag{3.18}$$

3.3 Kinematical Constraints

To setup a well-posed problem, the kinematical constraint on the RVE has to be defined. For the problem of interest, this consists of defining the space of kinematically admissible microscopic displacements and consequently the space of virtual kinematically admissible microscopic displacements $\mathscr{V}_\mu$.

This section is concerned with defining the possible kinematical constraints that can be imposed on the RVE starting with the minimum kinematical constraint. Further constraints will also be introduced. As will be shown, the choice of kinematical constraint defines different classes multi-scale models [4].

3.3.1 The Minimum Kinematical Constraint

The assumption made over the deformation gradient in Section 3.2 imposes a constraint on the allowable displacements of the RVE. From Equation 3.7, the constraint on the displacement field of the RVE can be expressed as

$$\int_{\partial\Omega_\mu^s} \boldsymbol{u_\mu}(\boldsymbol{y}, t) \otimes \boldsymbol{N}(\boldsymbol{y}) \ dA = V_\mu(\bar{\boldsymbol{F}}(\boldsymbol{x}, t) - \boldsymbol{I}) . \tag{3.19}$$

Consequently, the space of kinematically admissible microscopic displacement fields $\mathscr{K}_\mu$ (with $\boldsymbol{u}_\mu \in \mathscr{K}_\mu$) should at least satisfy Equation 3.19. This requires $\mathscr{K}_\mu$ to be a subset

of the minimally constrained set of kinematically admissible microscopic displacements, denoted by $\mathscr{K}_\mu^*$ and defined by Equation 3.19:

$$\mathscr{K}_\mu \subset \mathscr{K}_\mu^* \equiv \left\{ \boldsymbol{u},\ \text{sufficiently regular} \mid \int_{\partial\Omega_\mu} \boldsymbol{u} \otimes \boldsymbol{N}\ dA = V_\mu \left(\boldsymbol{F} - \boldsymbol{I}\right) \right\}, \tag{3.20}$$

and with a *sufficiently regular* field meaning that all the operations in which they are involved make sense [4, 33]. An extension to this procedure is to include the additive split 3.11 introduced in the previous section to Equation 3.20. This leads to the following,

$$\tilde{\mathscr{K}}_\mu \subset \tilde{\mathscr{K}}_\mu^* \equiv \left\{ \boldsymbol{u},\ \text{sufficiently regular} \mid \int_{\partial\Omega_\mu} \boldsymbol{u} \otimes \boldsymbol{N}\ dA = \boldsymbol{0} \right\} \tag{3.21}$$

with $\tilde{\mathscr{K}}_\mu$ being the space of kinematically admissible microscopic displacement fluctuations (with $\tilde{\boldsymbol{u}}_\mu \in \tilde{\mathscr{K}}_\mu$) and $\tilde{\mathscr{K}}_\mu^*$ being the minimally constrained space of kinematically admissible microscopic displacement fluctuations.

For this class of virtual work-based variational formulation, the virtual displacements are defined as variations in the kinematically admissible displacements. Based on that, the corresponding space of virtual kinematically admissible displacements can be expressed as

$$\mathscr{V}_\mu \equiv \left\{ \boldsymbol{\eta} = \boldsymbol{u}_1 - \boldsymbol{u}_2 \mid \boldsymbol{u}_1, \boldsymbol{u}_2 \in \mathscr{K}_\mu \right\}. \tag{3.22}$$

On account of Equation 3.10, $\mathscr{V}_\mu$ can be modified to

$$\mathscr{V}_\mu = \left\{ \boldsymbol{\eta} = \tilde{\boldsymbol{u}}_1 - \tilde{\boldsymbol{u}}_2 \mid \tilde{\boldsymbol{u}}_1, \tilde{\boldsymbol{u}}_2 \in \tilde{\mathscr{K}}_\mu \right\}, \tag{3.23}$$

therefore, it coincides with the space of kinematically admissible displacement fluctuations:

$$\mathscr{V}_\mu = \tilde{\mathscr{K}}_\mu \subset \tilde{\mathscr{K}}_\mu^*. \tag{3.24}$$

3.3.2 Multi-scale Models

In this section, different classes of multi-scale models will be defined based on Equation 3.24. Those are namely, the minimally constrained (or uniform boundary traction) model, the periodic boundary fluctuations model, the linear boundary displacements (or zero boundary fluctuations) model and the Taylor model. These are all defined according to assumptions made on the displacement fluctuation field $\tilde{\boldsymbol{u}}_\mu$. The detailed description of these models is provided in the following.

The minimally constrained (or uniform boundary traction) model defines $\mathscr{V}_\mu$ as

$$\mathscr{V}_\mu = \mathscr{V}_\mu^{\text{trac}} \equiv \tilde{\mathscr{K}}_\mu^* \tag{3.25}$$

defined by Equation 3.21.

The periodic boundary fluctuations model is suitable to describe materials with periodic microstructures. The microstructure for this class of models is formed from a periodic repetition of the RVE.

Consider, for example, a two-dimensional square RVE for which each pair of equally sized sides i are assigned Γ_i^+ and Γ_i^-. Each pair is chosen such that the normals to the sides forming it, $\boldsymbol{n}_i^+$ and $\boldsymbol{n}_i^-$ respectively, are opposite in direction

$$\boldsymbol{n}_i^+ = -\boldsymbol{n}_i^-, \tag{3.26}$$

as illustrated in Figure 3.3.

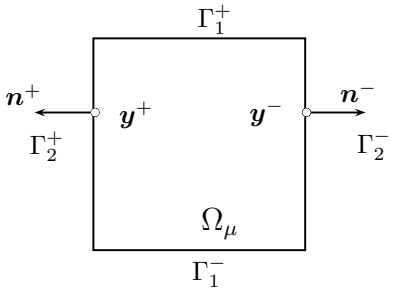

Figure 3.3: Square RVE for the periodic boundary fluctuations model.

This model is based on the assumption that the displacement fluctuation field of points y^+ and y^- on Γ_i^+ and Γ_i^-, respectively, are equal. That is, for each pair $\{\boldsymbol{y}^+, \boldsymbol{y}^-\}$,

$$\tilde{\boldsymbol{u}}_{\boldsymbol{\mu}}(\boldsymbol{y}^+, t) = \tilde{\boldsymbol{u}}_{\boldsymbol{\mu}}(\boldsymbol{y}^-, t). \tag{3.27}$$

Accordingly, the space $\mathscr{V}_\mu$ is defined as

$$\mathscr{V}_\mu = \mathscr{V}_\mu^{\text{per}} \equiv \left\{ \tilde{\boldsymbol{u}}_\mu \in \tilde{\mathscr{K}}_\mu^* \mid \tilde{\boldsymbol{u}}_\mu(\boldsymbol{y}^+, t) = \tilde{\boldsymbol{u}}_\mu(\boldsymbol{y}^-, t) \ \forall \text{ pairs } \{\boldsymbol{y}^+, \boldsymbol{y}^-\} \in \partial\Omega_\mu \right\}. \tag{3.28}$$

As all the displacement fluctuations in $\mathscr{V}_\mu^{\text{per}}$ satisfy the minimum kinematical constraint,

$$\mathscr{V}_\mu^{\text{per}} \subset \mathscr{V}_\mu^{\text{trac}} = \tilde{\mathscr{K}}_\mu^*. \tag{3.29}$$

The linear boundary displacements (or zero boundary fluctuations) model is derived by assigning zero displacement fluctuations on the RVE boundary. From Equation 3.11, the assumption made leads to

$$\boldsymbol{u}_{\boldsymbol{\mu}} = \left[\bar{\boldsymbol{F}}(\boldsymbol{x}, t) - \boldsymbol{I}\right] \boldsymbol{y} \text{ on } \partial\Omega_\mu. \tag{3.30}$$

The corresponding space $\mathscr{V}_\mu$ is expressed as

$$\mathscr{V}_\mu = \mathscr{V}_\mu^{\text{lin}} \equiv \left\{ \tilde{\boldsymbol{u}}_\mu \in \tilde{\mathscr{K}}_\mu^* \mid \tilde{\boldsymbol{u}}_\mu(\boldsymbol{y}, t) = \boldsymbol{0} \ \forall \boldsymbol{y} \in \partial\Omega_\mu \right\}. \tag{3.31}$$

The space $\mathscr{V}_\mu^{\text{lin}}$ trivially satisfies the periodic boundary fluctuations described earlier, making $\mathscr{V}_\mu^{\text{lin}}$ a subset of $\mathscr{V}_\mu^{\text{per}}$. From Equation 3.29,

$$\mathscr{V}_\mu^{\text{lin}} \subset \mathscr{V}_\mu^{\text{per}} \subset \mathscr{V}_\mu^{\text{trac}} \tag{3.32}$$

is obtained.

The Taylor model simply assumes that the RVE is only subjected to homogeneous deformation, i.e., assumes zero displacement fluctuations on the entire RVE. This can be expressed as

$$\boldsymbol{u_\mu} = \left[\bar{\boldsymbol{F}}(\boldsymbol{x}, t) - \boldsymbol{I}\right] \boldsymbol{y} \text{ and } \tilde{\boldsymbol{u}}_\mu = \boldsymbol{0} \quad \forall \boldsymbol{y} \in \Omega_\mu. \tag{3.33}$$

This implies that the space $\mathscr{V}_\mu$ is expressed as

$$\mathscr{V}_\mu = \mathscr{V}_\mu^{\text{Taylor}} \equiv \{\boldsymbol{0}\}. \tag{3.34}$$

Trivially, the space $\mathscr{V}_\mu^{\text{Taylor}}$ satisfies the linear boundary displacements model leading to

$$\mathscr{V}_\mu^{\text{Taylor}} \subset \mathscr{V}_\mu^{\text{lin}} \subset \mathscr{V}_\mu^{\text{per}} \subset \mathscr{V}_\mu^{\text{trac}}. \tag{3.35}$$

Chapter 4

Multi-Scale Finite Element Formulation

Chapter 3 provides the BVP for macro-continuum and the corresponding RVE, in addition to the possible boundary conditions that can be imposed on the RVE. The solution of the problem follows trivially.

In this chapter, the solution to the RVE problem using *Finite Element* (FE) methods is described. It starts by linearising the microscopic equilibrium equation, this is crucial for the solution of the discretized nonlinear problem. Afterwards, Voigt notation essential for the FE formulation is introduced. This is followed by the FE approximation (discretization) of the nonlinear microscopic BVP which is solved iteratively using Newton-Raphson (N-R) iterative algorithm. Later, the discretization of the multi-scale models, described in Section 3.3.2, is developed. And finally, the overall implementation procedure is provided.

4.1 Linearisation of Microscopic Equilibrium Equation

The linearisation of the nonlinear microscopic equilibrium equation 3.18 is important for the solution of the FE approximation of the problem. Typically, the solution is obtained by the use of iterative methods of incremental linearised problems, in particular, the Newton-Raphson interative method.

By taking the directional derivative of the virtual work δW in the direction of a displacement $\delta \boldsymbol{u}_{\boldsymbol{\mu}}$,

$$D\delta W[\delta \boldsymbol{u}_{\boldsymbol{\mu}}] = \int_{\Omega^s_\mu} D(\boldsymbol{P}_{\boldsymbol{\mu}} : \nabla \boldsymbol{\eta})[\delta \boldsymbol{u}_{\boldsymbol{\mu}}]\, dV, \tag{4.1}$$

The same procedure provided in Section 2.4.2 is followed here. The final linearised form

of the virtual work is obtained as

$$D\delta W[\delta \boldsymbol{u_\mu}] = \int_{\Omega^s_\mu} \frac{\partial \boldsymbol{P_\mu}}{\partial \boldsymbol{F_\mu}} : \nabla \delta \boldsymbol{u_\mu} : \nabla \boldsymbol{\eta} \; dV,$$

$$D\delta W[\delta \boldsymbol{u_\mu}] = \int_{\Omega^s_\mu} \mathbf{A} : \nabla \delta \boldsymbol{u_\mu} : \nabla \boldsymbol{\eta} \; dV, \tag{4.2}$$

where $\mathbf{A}$ is the material tangent modulus depending on the constitutive model used. This is considering that the stress $\boldsymbol{P_\mu}$ depends on the microscopic deformation gradient which, in turn, depends on the microscopic displacement $\boldsymbol{u_\mu}$, thus, $\boldsymbol{P_\mu}$ can be expressed as $\boldsymbol{P_\mu}\left(\boldsymbol{F_\mu}(\boldsymbol{u_\mu})\right)$.

4.2 Voigt Notation

The FE formulation and solution are most convenient when the components of tensors are expressed in matrix form. This is known as the *Voigt notation* and it is inevitable for the present work. As the Voigt notation is not unique, the notation used throughout the present work is established in this section.

The formulation used in the present work is based on finite strains, hence, dealing with non-symmetric stress tensors [5]. In this case, for in-plane problems, the second order tensors, e.g. the first Piola-Kirchhoff stress $\boldsymbol{P}$, are represented as

$$\boldsymbol{P} = \begin{bmatrix} P_{11} & P_{12} \\ P_{21} & P_{22} \end{bmatrix} \rightarrow \begin{bmatrix} P_{11} \\ P_{21} \\ P_{12} \\ P_{22} \end{bmatrix}. \tag{4.3}$$

This order of components is then adopted to all the tensors involved in the computations. Fourth order tensors , for in-plane problem, can be expressed as

$$\begin{bmatrix} \mathsf{A}_{1111} & \mathsf{A}_{1121} & \mathsf{A}_{1112} & \mathsf{A}_{1122} \\ \mathsf{A}_{2111} & \mathsf{A}_{2121} & \mathsf{A}_{2112} & \mathsf{A}_{2122} \\ \mathsf{A}_{1211} & \mathsf{A}_{1221} & \mathsf{A}_{1212} & \mathsf{A}_{1222} \\ \mathsf{A}_{2211} & \mathsf{A}_{2221} & \mathsf{A}_{2212} & \mathsf{A}_{2222} \end{bmatrix}. \tag{4.4}$$

It is to be noted the matrix described in Equation 4.4 is consistent with the component order followed in Equation 4.3 and that the matrices provided in the following chapters will follow the same notation described above.

4.3 Finite Element Discretization and Solution of the Microscopic Equilibrium Equation

A standard finite element procedure is used to discretize the weak form of the equilibrium of the RVE 3.18. For a given discretization h, the reference configuration Ω_μ is divided into

N elements giving a discretized domain Ω_μ^h. Similar to the procedure followed in Section 2.5, a position $\boldsymbol{y}$ belonging to an element e can be expressed as

$$\boldsymbol{y} = \boldsymbol{N}_a^{(e)} \boldsymbol{y}_a, \tag{4.5}$$

where $\boldsymbol{N}_a^{(e)}$ are the shape functions describing element e, $\boldsymbol{y}_a$ are the element nodal coordinates, n is the number of nodes per element. Similarly, the space of virtual displacements $\mathscr{V}_\mu$ can be discretized into $\mathscr{V}_\mu^h$, and the virtual displacement $\boldsymbol{\eta}$ and its gradient are also discretized as

$$\boldsymbol{\eta} = \boldsymbol{N}_a^{(e)} \boldsymbol{\eta}_a \text{ and } \boldsymbol{\eta} = \boldsymbol{G}_a^{(e)} \boldsymbol{\eta}_a, \tag{4.6}$$

where $\boldsymbol{G}_a^{(e)}$ is the associated local non-symmetric gradient matrix at node a. The matrix $\boldsymbol{G}^{(e)}$ has $2n \times 4$ dimensions based on the Voigt notation set by Equation 4.3 and it has the following format,

$$\boldsymbol{G}^{(e)} = \begin{bmatrix} N_{1,x}^{(e)} & 0 & N_{2,x}^{(e)} & 0 & \dots & N_{n,x}^{(e)} & 0 \\ 0 & N_{1,x}^{(e)} & 0 & N_{2,x}^{(e)} & \dots & 0 & N_{n,x}^{(e)} \\ N_{1,y}^{(e)} & 0 & N_{2,y}^{(e)} & 0 & \dots & N_{n,y}^{(e)} & 0 \\ 0 & N_{1,y}^{(e)} & 0 & N_{2,y}^{(e)} & \dots & 0 & N_{n,y}^{(e)} \end{bmatrix} \tag{4.7}$$

in Cartesian coordinates, where $N_{a,j}^{(e)}$ is the derivative of the element e shape function describing node a by the j-coordinate. This is then used to obtain a global non-symmetric gradient matrix $\boldsymbol{G}$,

$$\boldsymbol{G} = \bigcup_{e=1}^{N} \boldsymbol{G}_a^{(e)}, \tag{4.8}$$

based on the finite element assembly of the elemental matrices.

The finite element approximation of the microscopic equilibrium problem 3.18 is based on the previously described discretization, this can be expressed as

$$\left\{ \int_{\Omega_\mu^{s,h}} \boldsymbol{G}^T \boldsymbol{P}_{\boldsymbol{\mu}} \, dV \right\} \cdot \boldsymbol{\eta} = 0 \; \forall \boldsymbol{\eta} \in \mathscr{V}_\mu^h. \tag{4.9}$$

An iterative Newton procedure is used to solve Equation 4.9 which determines the displacement fluctuation field via the update

$$\tilde{\boldsymbol{u}}_\mu^{(k)} \Leftarrow \tilde{\boldsymbol{u}}_\mu^{(k-1)} + \Delta \tilde{\boldsymbol{u}}_\mu^{(k)} \tag{4.10}$$

for an iteration k. The field $\Delta \tilde{\boldsymbol{u}}_\mu^{(k)}$ is obtained from the solution of the linearised equilibrium problem that has the form

$$\left[\mathbb{T}^{(k-1)} + \mathbb{K}^{(k-1)} \Delta \tilde{\boldsymbol{u}}_\mu^{(k)} \right] \cdot \boldsymbol{\eta} = 0 \; \forall \boldsymbol{\eta} \in \mathscr{V}_\mu^h, \tag{4.11}$$

as no external force vector is involved in this case and where $\mathbb{T}^{(k-1)}$ is the internal force vector,

$$\mathbb{T}^{(k-1)} \equiv \int_{\Omega_\mu^{s,h}} \boldsymbol{G}^T \boldsymbol{P}_{\boldsymbol{\mu}} \left(\boldsymbol{F}_{\boldsymbol{\mu}}(\tilde{\boldsymbol{u}}_{\boldsymbol{\mu}}^{(k-1)}) \right) \, dV, \tag{4.12}$$

and the tangent stiffness matrix

$$\mathbb{K}^{(k-1)} \equiv \int_{\Omega_\mu^{s,h}} \boldsymbol{G}^T \boldsymbol{A}^{(k-1)} \boldsymbol{G} \, dV, \tag{4.13}$$

with $\boldsymbol{A}$ being the consistent constitutive tangent matrix of the RVE defined as the matrix form of the constitutive tangent operator

$$\mathbf{A}^{(k-1)} \equiv \left. \frac{\partial \boldsymbol{P}_{\boldsymbol{\mu}}}{\partial \boldsymbol{F}_{\boldsymbol{\mu}}} \right|_{\boldsymbol{F}_{\boldsymbol{\mu}}(\tilde{\boldsymbol{u}}_{\boldsymbol{\mu}}^{(k-1)})}, \tag{4.14}$$

which follows the Voigt notation described in Section 4.2 and has the form of matrix 4.4.

4.4 Finite Element Implementation of the Multi-scale Models

The solution of the microscopic equilibrium problem using the Newton-Raphson procedure requires defining the discretized space of virtual kinematically admissible displacements $\mathscr{V}_\mu^h$. As the latter depends on the choice of multi-scale model, the discretization of the models is essential. An implementation procedure analogous to that described by Perić *et al.* [33], for small strains, will be followed in the present work.

The Taylor model does not require numerical solutions as the space $\mathscr{V}_\mu^{\text{Taylor}}$ defines the solution to problem 4.11 by assigning zero displacement fluctuations on all the *degrees of freedom* (dofs) of the RVE. This is not the case of the other models, for that reason, these are described in this section.

4.4.1 Discretization of the Minimally Constrained Model

To implement the minimally constrained model into a FE framework, the space of virtual kinematically admissible displacement described in Equation 3.25 is discretized as

$$\mathscr{V}_\mu^{\text{trac},h} = \left\{ \boldsymbol{\eta} = \begin{bmatrix} \boldsymbol{\eta}_i \\ \boldsymbol{\eta}_b \end{bmatrix} \mid \int_{\partial\Omega_\mu^h} \boldsymbol{N}_b \boldsymbol{\eta}_b \otimes \boldsymbol{n} \, dA = \mathbf{0} \right\}, \tag{4.15}$$

where $\boldsymbol{\eta_b}$ and $\boldsymbol{\eta_i}$ are vectors containing the boundary and the internal dofs, respectively. The boundary dofs are further split into free $\boldsymbol{\eta}_f$, dependent $\boldsymbol{\eta}_d$ and prescribed $\boldsymbol{\eta}_p$ dofs as

$$\boldsymbol{\eta}_b = \begin{bmatrix} \boldsymbol{\eta}_f \\ \boldsymbol{\eta}_d \\ \boldsymbol{\eta}_p \end{bmatrix}. \tag{4.16}$$

The integral in Equation 4.15 can be equivalently expressed in matrix format [33, 40] as

$$\boldsymbol{C}\boldsymbol{\eta}_b = \mathbf{0}, \tag{4.17}$$

where $\boldsymbol{C}$ is the constraint matrix. Matrix $\boldsymbol{C}$ has to be consistent with the Voigt notation described earlier. For an arbitrary finite element in two-dimensions, matrix $\boldsymbol{C}$ for an element e can be written as

$$\boldsymbol{C}^{(e)} = \begin{bmatrix} \int_{\Gamma^{(e)}} N_1^{(e)} n_1 dA & 0 & \cdots & \int_{\Gamma^{(e)}} N_p^{(e)} n_1 dA & 0 \\ 0 & \int_{\Gamma^{(e)}} N_1^{(e)} n_1 dA & \cdots & 0 & \int_{\Gamma^{(e)}} N_p^{(e)} n_1 dA \\ \int_{\Gamma^{(e)}} N_1^{(e)} n_2 dA & 0 & \cdots & \int_{\Gamma^{(e)}} N_p^{(e)} n_2 dA & 0 \\ 0 & \int_{\Gamma^{(e)}} N_1^{(e)} n_2 dA & \cdots & 0 & \int_{\Gamma^{(e)}} N_p^{(e)} n_2 dA \end{bmatrix}, \tag{4.18}$$

where p is the number of nodes of element e intersecting the boundaries of the RVE denoted by $\Gamma^{(e)}$. Following the same procedure described in [4, 33, 40], Equation 4.17 can be rewritten as

$$\begin{bmatrix} \boldsymbol{C}_f & \boldsymbol{C}_d & \boldsymbol{C}_p \end{bmatrix} \begin{bmatrix} \boldsymbol{\eta}_f \\ \boldsymbol{\eta}_d \\ \boldsymbol{\eta}_p \end{bmatrix} = \mathbf{0}, \tag{4.19}$$

based on the split of the boundary dofs described by 4.16. To prevent rigid body motion at least 3 degrees of freedom have to be prescribed for the two-dimensional case, hence, $\boldsymbol{\eta_p} = \mathbf{0}$. The system of equations described by 4.19 is reduced to

$$\begin{bmatrix} \boldsymbol{C}_f & \boldsymbol{C}_d \end{bmatrix} \begin{bmatrix} \boldsymbol{\eta}_f \\ \boldsymbol{\eta}_d \end{bmatrix} = \mathbf{0}. \tag{4.20}$$

In view of the Voigt notation used to build matrix $\boldsymbol{C}^{(e)}$, Equation 4.20, in two-dimensions, involves 4 scalar equations with 4 dependent degrees of freedom. Consequently, these 4 scalar equations involve $2m-4$ variables, where m is the total number of boundary nodes. This is demonstrated in Figure 4.1. Equation 4.20 is used to relate the dofs $\boldsymbol{\eta}_f$ and $\boldsymbol{\eta}_d$,

$$\boldsymbol{\eta}_d = \boldsymbol{R}\boldsymbol{\eta}_f, \quad \text{where} \quad \boldsymbol{R} \equiv -\boldsymbol{C}_d^{-1}\boldsymbol{C}_f. \tag{4.21}$$

Consequently, the discretized space $\mathscr{V}_\mu^{\text{trac},h}$, expressed in Equation 4.15, can be modified to

$$\mathscr{V}_\mu^{\text{trac},h} = \left\{ \boldsymbol{\eta} = \begin{bmatrix} \boldsymbol{\eta}_i \\ \boldsymbol{\eta}_f \\ \boldsymbol{\eta}_d \end{bmatrix} \mid \boldsymbol{\eta}_d = \boldsymbol{R}\boldsymbol{\eta}_f \right\}. \tag{4.22}$$

By applying the same split imposed on $\boldsymbol{\eta}$ to the components of linearised problem 4.11, and also accounting for the definition of the space $\mathscr{V}_\mu^{\text{trac},h}$ and that it coincides with the space of admissible displacement fluctuations (see Equation 3.24), Equation 4.11 can be expressed as,

$$\left\{ \begin{bmatrix} \mathbb{F}_i \\ \mathbb{F}_f \\ \mathbb{F}_d \end{bmatrix}^{(k-1)} + \begin{bmatrix} \mathbb{K}_{ii} & \mathbb{K}_{if} & \mathbb{K}_{id} \\ \mathbb{K}_{fi} & \mathbb{K}_{ff} & \mathbb{K}_{fd} \\ \mathbb{K}_{di} & \mathbb{K}_{df} & \mathbb{K}_{dd} \end{bmatrix}^{(k-1)} \begin{bmatrix} \Delta\tilde{\boldsymbol{u}}_i \\ \Delta\tilde{\boldsymbol{u}}_f \\ \boldsymbol{R}\Delta\tilde{\boldsymbol{u}}_f \end{bmatrix}^{(k)} \right\} \cdot \begin{bmatrix} \boldsymbol{\eta}_i \\ \boldsymbol{\eta}_f \\ \boldsymbol{R}\boldsymbol{\eta}_f \end{bmatrix} = 0 \quad \forall \boldsymbol{\eta}_i, \boldsymbol{\eta}_f. \tag{4.23}$$

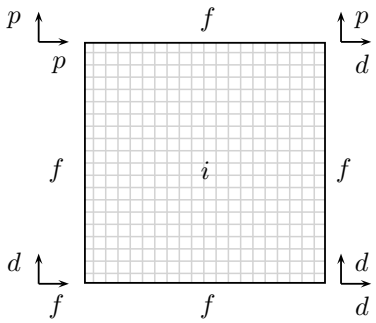

Figure 4.1: Square RVE for the minimally constrained model showing the interior i, prescribed p, dependent d and free f dofs.

The procedure described above helps reducing the system to

$$\begin{bmatrix} \mathbb{K}_{ii} & \mathbb{K}_{if} + \mathbb{K}_{id}\boldsymbol{R} \\ \mathbb{K}_{fi} + \boldsymbol{R}^T\mathbb{K}_{di} & \mathbb{K}_{ff} + \mathbb{K}_{fd}\boldsymbol{R} + \boldsymbol{R}^T\mathbb{K}_{df} + \boldsymbol{R}^T\mathbb{K}_{dd}\boldsymbol{R} \end{bmatrix}^{(k-1)} \begin{bmatrix} \Delta\tilde{\boldsymbol{u}}_i \\ \Delta\tilde{\boldsymbol{u}}_f \end{bmatrix}^{(k)} = - \begin{bmatrix} \mathbb{F}_i \\ \mathbb{F}_f \end{bmatrix}^{(k-1)}, \tag{4.24}$$

which is solved for the internal and free dofs displacement fluctuations and the displacement fluctuation of the dependent dofs are obtained afterwards from relation 4.21.

4.4.2 Discretization of the Periodic Boundary Fluctuations Model

The same procedure described above is followed here for the periodic boundary fluctuations model. The associated space of admissible virtual displacements $\mathscr{V}_\mu^{\text{per}}$, introduced in Equation 3.28, is discretized as

$$\mathscr{V}_\mu^{\text{per},h} = \left\{ \boldsymbol{\eta} = \begin{bmatrix} \boldsymbol{\eta}_i \\ \boldsymbol{\eta}_+ \\ \boldsymbol{\eta}_- \end{bmatrix} \Big| \boldsymbol{\eta}_+ = \boldsymbol{\eta}_- \right\}, \tag{4.25}$$

where $\boldsymbol{\eta}_i, \boldsymbol{\eta}_+$ and $\boldsymbol{\eta}_-$ are vectors containing the interior, nodes belonging to Γ^+ and nodes belonging to Γ^-, respectively. It is noteworthy that some nodes are prescribed (denoted by p) with zero displacement fluctuations to prevent rigid body motion. The split of the mesh dofs is illustrated in Figure 4.2.

This discretization is then applied to the components of the linearised problem 4.11, taking into consideration the condition of periodicity $\boldsymbol{\eta}_+ = \boldsymbol{\eta}_-$ and the relation between the space of virtual displacement and the space of displacement fluctuations (Equation 3.24), the following system of equations can be obtained,

$$\left\{ \begin{bmatrix} \mathbb{F}_i \\ \mathbb{F}_+ \\ \mathbb{F}_- \end{bmatrix}^{(k-1)} + \begin{bmatrix} \mathbb{K}_{ii} & \mathbb{K}_{i+} & \mathbb{K}_{i-} \\ \mathbb{K}_{+i} & \mathbb{K}_{++} & \mathbb{K}_{+-} \\ \mathbb{K}_{-i} & \mathbb{K}_{-+} & \mathbb{K}_{--} \end{bmatrix}^{(k-1)} \begin{bmatrix} \Delta\tilde{\boldsymbol{u}}_i \\ \Delta\tilde{\boldsymbol{u}}_+ \\ \Delta\tilde{\boldsymbol{u}}_+ \end{bmatrix}^{(k)} \right\} \cdot \begin{bmatrix} \boldsymbol{\eta}_i \\ \boldsymbol{\eta}_+ \\ \boldsymbol{\eta}_+ \end{bmatrix} = 0 \quad \forall \boldsymbol{\eta}_i, \boldsymbol{\eta}_+. \tag{4.26}$$

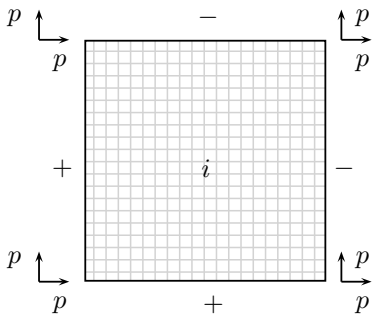

Figure 4.2: Square RVE for the periodic boundary fluctuations model showing the interior i, prescribed p dofs together with dofs belonging to Γ^+ denoted by $+$ and those belonging to Γ^- denoted by $-$.

As shown in the above equation, the periodicity condition reduces the unknown dofs to $\boldsymbol{\eta}_i$ and $\boldsymbol{\eta}_+$, which consequently reduces the system of equations to

$$\begin{bmatrix} \mathbb{K}_{ii} & \mathbb{K}_{i+} + \mathbb{K}_{i-} \\ \mathbb{K}_{+i} + \mathbb{K}_{-i} & \mathbb{K}_{++} + \mathbb{K}_{+-} + \mathbb{K}_{-+} + \mathbb{K}_{--} \end{bmatrix}^{(k-1)} \begin{bmatrix} \Delta\tilde{\boldsymbol{u}}_i \\ \Delta\tilde{\boldsymbol{u}}_+ \end{bmatrix}^{(k)} = - \begin{bmatrix} \mathbb{F}_i \\ \mathbb{F}_+ \end{bmatrix}^{(k-1)}, \tag{4.27}$$

to be solved for $\Delta\tilde{\boldsymbol{u}}_i$ and $\Delta\tilde{\boldsymbol{u}}_+$.

4.4.3 Discretization of the Linear Boundary Displacements Model

The discretization of the linear boundary displacements model is straightforward as the assumption made here is that all the boundary dofs are prescribed with zero displacement fluctuations. That is, the only dofs to be solved for are the interior dofs. This specialization when applied to the linearised problem, reduces the system to

$$\left[\mathbb{K}_{ii}\right]^{(k-1)} \left[\Delta\tilde{\boldsymbol{u}}_i\right]^{(k)} = - \left[\mathbb{F}_i\right]^{(k-1)}, \tag{4.28}$$

which coincides with the conventional FE solution procedure.

4.4.4 Discretization of the Taylor Model

As mentioned earlier, the Taylor model does not require any numerical solution, as, by definition of the space $\mathscr{V}_\mu^{\text{Taylor}}$, all the involved dofs on the boundaries and in the interior of the RVE are prescribed with zero displacement fluctuations. That is, the solution to linearised problem 4.11 are known a priori:

$$\left[\Delta\tilde{\boldsymbol{u}}_{\text{all}}\right]^{(k)} = \left[\mathbf{0}\right], \tag{4.29}$$

where $\Delta\tilde{\boldsymbol{u}}_{\text{all}}$ denotes the Newton-Raphson displacement update of all dofs.

4.5 The Overall Procedure

The procedure, described in the preceding sections, is implemented in MATLAB [43] for hyperelastic materials. Several types of elements are also developed, namely, 3-noded triangular elements, 4-noded quadrilateral elements, 4-noded quadrilateral elements with *F-bar formulation* [3, 5] and 8-noded quadrilateral elements with reduced and full integration. The Newton-Raphson algorithm implemented is also coupled with a sub-incrementation option. That is, if the maximum number of iterations is reached without convergence for a particular time step n, the incrementation size is cut and the procedure for n is restarted from the last converged state.

The overall procedure to solve the microscopic equilibrium problem 3.3, using FE discretization, and to obtain macroscopic (homogenized) properties is illustrated in Figure 4.3.

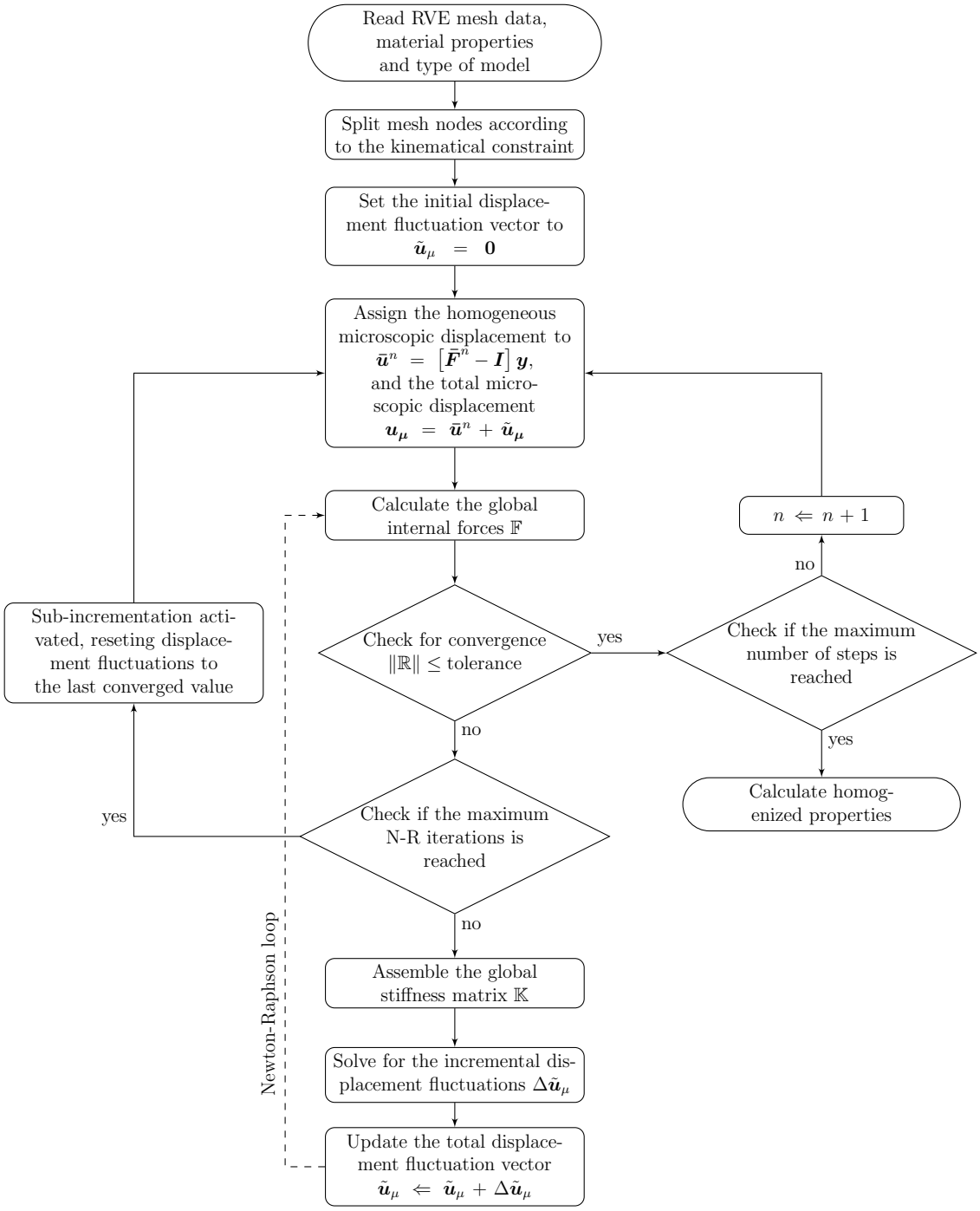

Figure 4.3: The overall finite element procedure to solve the microscopic equilibrium problem and obtain homogenized properties.

Chapter 5

Analytical Estimates of the Behavior of Heterogeneous Hyperelastic Materials

The well-developed linear elasticity theory suggests a number of estimates for the behavior of composites with elastic phases subjected to small strains. The simplest of these are the *Voigt upper bound* (1889) and the *Reuss lower bound* (1929) that are based on classical expressions for the minimum potential energy. These bounds do not include any information about the distribution, the shape nor the phase volume fractions. Hashin and Shtrikman (1963) provided tighter bounds denoted by the *Hashin-Shtrikman bounds*. These are based on the choice of a homogeneous reference material based on which the overall behavior can be obtained. If the softer (stiffer) material is used as reference the bound obtained is a lower (upper) bound. Many more estimates are available for this case in contrast to composites made of nonlinear materials.

Of particular interest is the recently developed method by Ponte Castañeda as it was shown to be effective in approximating the behavior of nonlinear composite materials [34], that is the *Second-Order Estimate*. It is initially developed by Ponte Castañeda (1996) [36] for small strains, power-law materials and extended later to hyperelastic materials [34].

This chapter is concerned with the formulation and implementation of analytical methods for estimating the macroscopic behavior of heterogeneous hyperelastic materials subjected to finite strains with a particular focus to the SOE. The objective is to express the overall behavior in the form of an *effective stored energy function* of the composite material as analytical as possible. The effective stored energy function is described first, followed by the description of the Second-Order Estimate (SOE). The overall procedure and implementation will be described later. This is followed by other analytical solutions specialized to specific types of loading and materials. And finally, the validation of results is performed comparing the SOE implemented against the described analytical solutions.

5.1 The Effective Strain Energy Function

Consider the initial configuration Ω[1] of an RVE made of N different phases. Let $\Psi^{(r)}(\boldsymbol{F})$ be the strain energy function of phase r ($r = 1, ..., N$), where $\boldsymbol{F}$ is the microscopic deformation gradient tensor (refer to footnote 1). The microscopic strain energy function can be described as

$$\Psi(\boldsymbol{y}, \boldsymbol{F}) = \sum_{r=1}^{N} \theta^{(r)}(\boldsymbol{y}) \Psi^{(r)}(\boldsymbol{F}), \tag{5.1}$$

where $\boldsymbol{y}$ defines the particle point in Ω (see Figure 3.1) and $\theta^{(r)}(\boldsymbol{y})$ is defined by

$$\theta^{(r)}(\boldsymbol{y}) = \begin{cases} 1 & \text{if } \boldsymbol{y} \in \Omega^{(r)}, \\ 0 & \text{otherwise,} \end{cases}$$

where $\Omega^{(r)}$ is the initial configuration of phase r.

The prescribed macroscopic average deformation gradient is obtained by taking the volume average of the microscopic deformation gradient over the initial volume as

$$\bar{\boldsymbol{F}} = \frac{1}{V_\Omega} \int_\Omega \boldsymbol{F} \, dV \doteq \langle \boldsymbol{F} \rangle, \tag{5.2}$$

where $V_\Omega = \text{vol}(\Omega)$. The macroscopic behavior is described by an *effective strain energy function* $\tilde{\Psi}$, hence, the overall first Piola-Kirchhoff stress can be expressed as

$$\bar{\boldsymbol{P}}(\bar{\boldsymbol{F}}) = \frac{\partial \tilde{\Psi}(\bar{\boldsymbol{F}})}{\partial \bar{\boldsymbol{F}}}. \tag{5.3}$$

According to Equation 5.3, the effective strain energy function is required to characterize the overall macroscopic behavior and this will be obtained in the following.

5.2 The Second-Order Estimate

The *Second-Order Estimate* (SOE), developed by Ponte Castañeda (1996) [36], is based on the asymptotic expansion of the nonlinear hyperelastic composite behavior using the second-order *Taylor expansion* of the strain energy function of its constituents. This linearised behavior allows the use of the well-defined classical bounds for linear elastic composites. The linearised composite has the same microstructure of the nonlinear composite and it is denoted by the *Linear Comparison Composite* (LCC).

The SOE procedure is described in the following for hyperelastic composites. It can be found in detail elsewhere, for instance, Ponte Castañeda (1996, 2012) [35, 36] for small strain formulation, Ponte Castañeda and Tiberio (2000) [34] for hyperelastic composites

[1] Although this quantity describes the microstructure, the notation $(\cdot)_\mu$ is suppressed for convenience.

studying particle-reinforced RVEs, Lopez-Pamies and Ponte Castañeda (2004, 2007) [16, 19] for porous RVEs in finite strains.

The effective strain energy function describing the overall behavior of the heterogeneous hyperelastic material is given in this context by the variational principle

$$\tilde{\Psi}(\bar{\boldsymbol{F}}) = \min_{\boldsymbol{F}} \langle \Psi(\boldsymbol{y}, \boldsymbol{F}) \rangle = \min_{\boldsymbol{F}} \sum_{r=1}^{N} c^{(r)} \langle \Psi^{(r)}(\boldsymbol{F}) \rangle^{(r)}, \tag{5.4}$$

where $\langle \cdot \rangle^{(r)}$ denotes the volume average over phase r, and $c^{(r)}$ is the initial volume fraction of phase r and is equal to $\langle \theta^{(r)} \rangle$. The SOE method involves the approximation of $\Psi^{(r)}(\boldsymbol{F})$ by its second-order Taylor expansion about the average deformation gradient $\bar{\boldsymbol{F}}^{(r)} (= \langle \boldsymbol{F} \rangle^{(r)})$ over phase r

$$\Psi^{(r)}(\boldsymbol{F}) = \Psi^{(r)}(\bar{\boldsymbol{F}}^{(r)}) + (\boldsymbol{F} - \bar{\boldsymbol{F}}^{(r)}) : \boldsymbol{P}^{(r)} + \frac{1}{2}(\boldsymbol{F} - \bar{\boldsymbol{F}}^{(r)}) : \mathbf{A}^{(r)} : (\boldsymbol{F} - \bar{\boldsymbol{F}}^{(r)}), \tag{5.5a}$$

$$\boldsymbol{P}^{(r)} = \frac{\partial \Psi^{(r)}}{\partial \boldsymbol{F}}(\bar{\boldsymbol{F}}^{(r)}), \tag{5.5b}$$

$$\mathbf{A}^{(r)} = \frac{\partial^2 \Psi^{(r)}}{\partial \boldsymbol{F}^2}(\bar{\boldsymbol{F}}^{(r)}), \tag{5.5c}$$

where expression 5.5a corresponds to the behavior of the linear but heterogeneous LCC. Equations 5.4 and 5.5 are then used to obtain the effective strain-energy of the heterogeneous material. This leads to an effective strain energy function as obtained by Ponte Castañeda (1996) [36] and Ponte Castañeda and Tiberio (2000) [34], that can expressed as

$$\tilde{\Psi}(\bar{\boldsymbol{F}}) = \sum_{r=1}^{N} c^{(r)} \left[\Psi^{(r)}(\bar{\boldsymbol{F}}^{(r)}) + \frac{1}{2}(\bar{\boldsymbol{F}} - \bar{\boldsymbol{F}}^{(r)}) : \boldsymbol{P}^{(r)} \right]. \tag{5.6}$$

Taking the derivative of Equation 5.6 with respect to the macroscopic deformation gradient, in view of Equation 5.3, the overall first Piola-Kirchhoff stress is obtained as

$$\bar{\boldsymbol{P}} = \sum_{r=1}^{N} \frac{c^{(r)}}{2} \left[\boldsymbol{P}^{(r)} + \left[\boldsymbol{P}^{(r)} + (\bar{\boldsymbol{F}} - \bar{\boldsymbol{F}}^{(r)}) : \mathbf{A}^{(r)} \right] : \frac{\partial \bar{\boldsymbol{F}}^{(r)}}{\partial \bar{\boldsymbol{F}}} \right]. \tag{5.7}$$

The effective strain energy function (Equation 5.6) and the overall first Piola-Kirchhoff stress (Equation 5.7) depend on the average deformation gradient in each phase $\bar{\boldsymbol{F}}^{(r)}$. This requires the solution of the variational problem expressed in terms of the LCC behavior. Ponte Castañeda and Tiberio (2000) [34] described how to obtain $\bar{\boldsymbol{F}}^{(r)}$ for N-phases. The special case where only two phases are involved is given by Levin (1967) [15] and a detailed description of this procedure is provided in [18, 34, 37].

5.2.1 The Second-Order Estimate for Two-phase Composites

Consider an RVE composed of two hyperelastic phases with strain energy function $\Psi^{(1)}$ and $\Psi^{(2)}$ with initial volume fractions $c^{(1)}$ and $c^{(2)}$, respectively. According to Levin (1967)

[15], for a two-phase composite (i.e. $r = 1, 2$), tensor $\bar{\boldsymbol{F}}^{(r)}$ required to obtain the overall composite behavior (Equations 5.6, 5.7) is obtained as

$$\bar{\boldsymbol{F}}^{(r)} = \mathbf{S}^{(r)} : \bar{\boldsymbol{F}} + (\mathbf{S}^{(r)} - \mathbf{I}) : (\Delta\mathbf{A})^{-1} : \Delta\boldsymbol{T}, \tag{5.8}$$

where $\mathbf{S}^{(r)}$ is the strain-concentration tensor in phase r, and tensors $\Delta\mathbf{A}$ and $\Delta\boldsymbol{T}$ are given as

$$\Delta\mathbf{A} = \mathbf{A}^{(1)} - \mathbf{A}^{(2)}, \tag{5.9a}$$
$$\Delta\boldsymbol{T} = \boldsymbol{T}^{(1)} - \boldsymbol{T}^{(2)}, \tag{5.9b}$$
$$\boldsymbol{T}^{(r)} = \boldsymbol{P}^{(r)} - \mathbf{A}^{(r)} : \bar{\boldsymbol{F}}^{(r)} . \tag{5.9c}$$

In order to obtain the strain-concentration tensors of both phases, the solution of the following equations is required,

$$c^{(1)}\mathbf{S}^{(1)} + c^{(2)}\mathbf{S}^{(2)} = \mathbf{I}, \tag{5.10a}$$
$$c^{(1)}\mathbf{A}^{(1)} : \mathbf{S}^{(1)} + c^{(2)}\mathbf{A}^{(2)} : \mathbf{S}^{(2)} = \tilde{\mathbf{A}}, \tag{5.10b}$$

where $\tilde{\mathbf{A}}$ is the overall tangent modulus of the linear heterogeneous material and it can be obtained from classical linear material estimates, for example, the *Hashin-Shtrikman* (HS) or the *Self-Consistent* (SC) estimates. For the current work, the HS estimate is used to obtain $\tilde{\mathbf{A}}$ as described in [18] and [35].

Consider a reference material with tangent modulus $\mathbf{A}^{(0)}$, the HS estimates are generated from

$$\tilde{\mathbf{A}} = \mathbf{A}^{(0)} + (1 - c^{(0)}) \left[c^{(0)}\mathbf{P}^{(0)} - (\Delta\mathbf{A})^{-1} \right]^{-1}, \tag{5.11}$$

where $\mathbf{P}^{(0)}$ is the *Hill Polarization tensor* evaluated at the reference material, $c^{(0)}$ is the volume fraction of the phase chosen as a reference, and $\Delta\mathbf{A}$ here is the difference in tangent moduli between the reference material and the other phase. For the case where $\mathbf{A}^{(2)} > \mathbf{A}^{(1)}$, if $\mathbf{A}^{(0)} = \mathbf{A}^{(2)}$, this gives the HS upper bound while if $\mathbf{A}^{(0)} = \mathbf{A}^{(1)}$, this gives the HS lower bound.

For the case of random, isotropic or statistically isotropic, aligned cylindrical second phase with initially circular cross sections, $\mathbf{P}^{(0)}$ can be expressed as [19],

$$\mathbf{P}^{(0)} = \frac{1}{2\pi} \int_{\xi_1^2 + \xi_2^2 = 1} \mathbf{H}^{(0)}(\xi_1, \xi_2, \xi_3 = 0)\, dS, \tag{5.12}$$

where $\mathsf{H}^{(0)}_{ijkl} = (\mathsf{A}_{imkn}\xi_m\xi_n)^{-1}\xi_j\xi_l$, and ξ_3 is aligned with the longitudinal axis of the cylindrical phase. The procedure described by Masson (2008) [24] is used to simplify Equation 5.12 and is summarized in the following.

The expression $\xi_1^2 + \xi_2^2 = 1$ describes the surface of an ellipse with $\xi_1 = \frac{x_1}{a_1}$ and $\xi_2 = \frac{x_2}{a_2}$, where a_1 and a_2 are the radii of the ellipse in directions x_1 and x_2, respectively, (for circular voids, $a_1 = a_2$). The following change of variables is performed

$$x_1 = \frac{\cos\theta}{a_1} \quad \text{and} \quad x_2 = \frac{\sin\theta}{a_2}.$$

Hence, the integral in Equation 5.12 becomes

$$\mathsf{P}^{(0)}_{ijkl} = \frac{1}{2\pi}\int_0^{2\pi} \mathsf{M}^{(0)}_{ijkl}(\theta)\, d\theta, \tag{5.13}$$

with

$$M^{(0)}_{ijkl} = \frac{1}{4}\left(\Gamma^{-1}_{jk}x_i x_l + \Gamma^{-1}_{ik}x_j x_l + \Gamma^{-1}_{jl}x_i x_k + \Gamma^{-1}_{il}x_j x_k\right), \text{ and}$$
$$\Gamma_{ik} = \mathsf{A}_{ijkl}x_j x_l.$$

It is to be noted that if the SC estimate were to be used instead of HS, the expression for $\tilde{\mathbf{A}}$ becomes implicit and has to be solved numerically.

5.2.2 The Overall Second-Order Estimate Procedure

Equation 5.8 providing the expression for $\bar{\boldsymbol{F}}^{(r)}$ depends on $\mathbf{S}^{(r)}$, $\mathbf{A}^{(r)}$ and $\boldsymbol{T}^{(r)}$ which are evaluated at $\bar{\boldsymbol{F}}^{(r)}$ leading to an implicit expression and hence requires a root-finding algorithm. The procedure implemented uses the simplest of these, namely, the *fixed-point iteration* algorithm.

It is also shown in Equation 5.8 that $\bar{\boldsymbol{F}}^{(r)}$ depends on its derivative with respect to the macroscopic deformation gradient $\bar{\boldsymbol{F}}$. To simplify the problem, this derivative is approximated by the strain-concentration tensor of phase r, that is

$$\frac{\partial \bar{\boldsymbol{F}}^{(r)}}{\partial \bar{\boldsymbol{F}}} = \mathbf{S}^{(r)}.$$

This is ignoring the implicit dependence of the quantities in Equation 5.8 on $\bar{\boldsymbol{F}}^{(r)}$. This has proven to be an acceptable approximation based on the results obtained from the procedure.

Another important aspect of the implemented procedure, is that the initial guess for $\bar{\boldsymbol{F}}^{(r)}$ depends on whether the material is compressible or incompressible, this is to ensure a faster convergence. The initial guesses are described as

$$\bar{\boldsymbol{F}}^{(r)}_i = \begin{cases} \frac{1}{1-c^{(r)}}\bar{\boldsymbol{F}} & \text{for compressible material,} \\ \bar{\boldsymbol{F}} & \text{for incompressible material.} \end{cases}$$

The overall procedure used to reach the Second-Order Estimate is described in Figure 5.1.

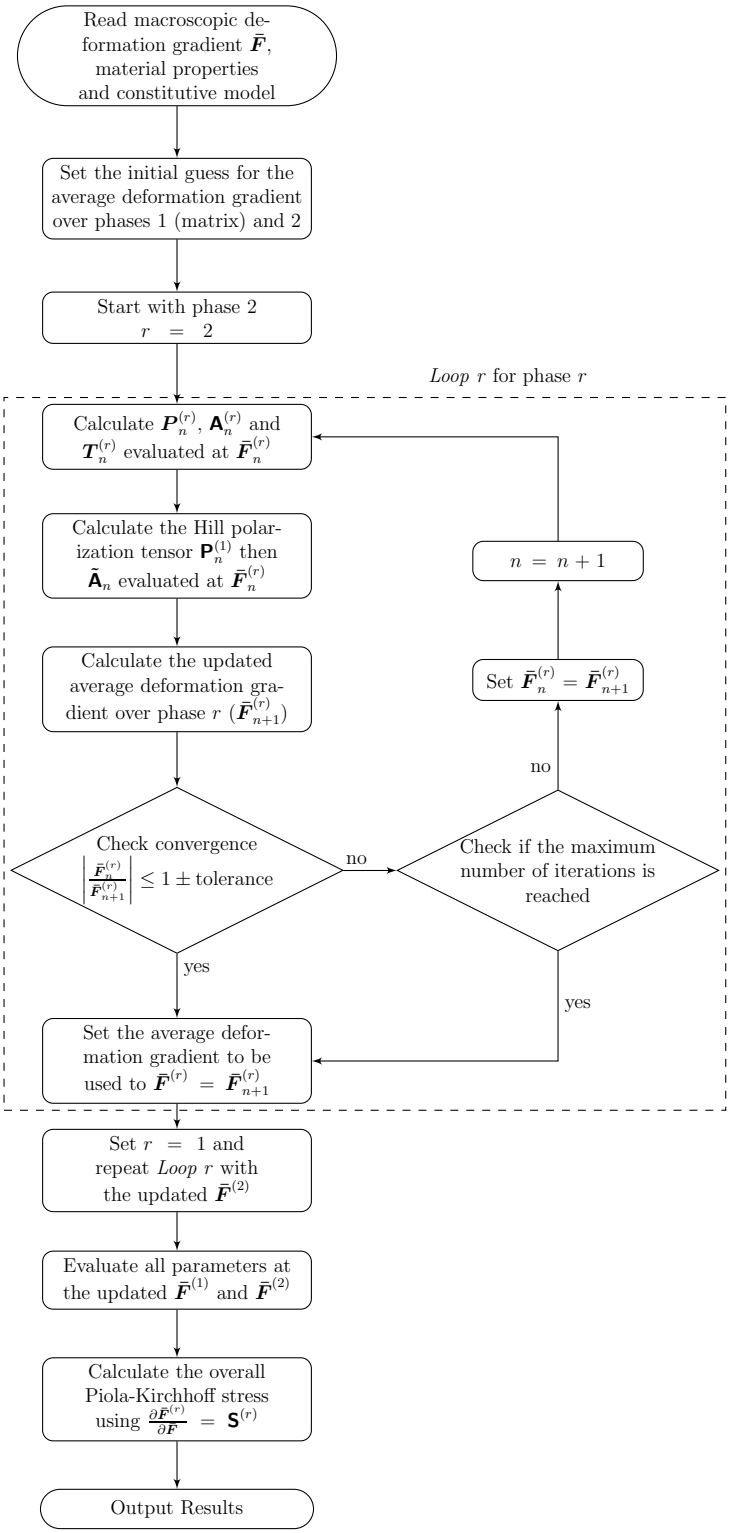

Figure 5.1: Procedure followed for the computation of the Second-Order Estimate given the material properties, the prescribed macroscopic deformation gradient and the constitutive model.

5.3 Analytical Estimates for Special Cases

This section provides some analytical solutions specialized to specific loading cases and materials. This is will help validate the results obtained from the SOE that is applicable for general two-phase RVEs.

5.3.1 Classical Voigt Upper Bound Estimate for Porous Materials

A means of validating the results obtained for porous materials is by employing the classical Voigt upper bound estimate. According to [19], when the strain field in the RVE is assumed to be constant a Voigt-type estimate for the overall behavior is obtained.

For a porous RVE, where only one phase is involved with energy function Ψ and an initial void volume fraction of c_o, the Voigt estimate $\tilde{\Psi}_V$ can be expressed as

$$\tilde{\Psi}_V(\bar{\boldsymbol{F}}) = (1 - c_o)\Psi(\bar{\boldsymbol{F}}), \tag{5.14a}$$

$$\bar{\boldsymbol{P}}_V(\bar{\boldsymbol{F}}) = (1 - c_o)\boldsymbol{P}(\bar{\boldsymbol{F}}). \tag{5.14b}$$

It is obvious from Equation 5.14 that the Voigt estimate depends only on the initial volume fraction of the phases, and does not take into consideration the distribution nor the shape of the voids [38].

5.3.2 Analytical Solution for Incompressible Porous Neo-Hookean Solids

Consider a two-dimensional RVE with incompressible Neo-Hookean matrix material and random isotropic distribution of pores of initial porosity volume fraction of c_o. Lopez-Pamies and Idiart (2009) [21] were able to obtain an analytical solution for the described problem. The solution is based on the solution of a *Hamilton-Jacobi* equation with c_o and $\bar{\boldsymbol{F}}$ are assumed to be the time and space, respectively, in the equation for infinite-rank laminate microstructures [11]. For the described RVE, the effective energy function, as obtained in [21], is expressed as

$$\tilde{\Psi}(\bar{\boldsymbol{F}}, c_o) = \frac{\mu}{2}\frac{1 - c_o}{1 + c_o}\left(\operatorname{tr}\bar{\boldsymbol{C}} - 2\right) + \frac{\mu}{2}(\bar{J} - 1)\left[\ln\left(\frac{\bar{J} + c_o - 1}{\bar{J}c_o}\right) - 2\frac{1 - c_o}{1 + c_o}\right]. \tag{5.15}$$

Although the matrix material is incompressible, the existence of pores renders a compressible overall behavior of the RVE. Thus, any deformation is admissible in this case. The corresponding overall first Piola-Kirchhoff stress can hence be expressed as

$$\begin{aligned}\bar{\boldsymbol{P}} = \mu\frac{1 - c_o}{1 + c_o}\bar{\boldsymbol{F}} + \frac{\mu}{2}\bar{J}\left[\ln\left(\frac{\bar{J} + c_o - 1}{\bar{J}c_o}\right) - 2\left(\frac{1 - c_o}{1 + c_o}\right)\right]\bar{\boldsymbol{F}}^{-T} \\ + \frac{\mu}{2}(\bar{J} - 1)\left(\frac{1 - c_o}{\bar{J} + c_o - 1}\right)\bar{\boldsymbol{F}}^{-T}.\end{aligned} \tag{5.16}$$

The simple in-plane shear deformation is of particular interest for this work for which the macroscopic deformation gradient is

$$\bar{\boldsymbol{F}}_\gamma = \begin{bmatrix} 1 & \gamma \\ 0 & 1 \end{bmatrix}, \tag{5.17}$$

where γ is the magnitude of shear deformation. Equation 5.15, in this case, reduces to

$$\tilde{\Psi}_\gamma(\bar{\boldsymbol{F}}_\gamma, c_o) = \frac{\mu}{2}\frac{1-c_o}{1+c_o}\left(\operatorname{tr}\bar{\boldsymbol{C}}_\gamma - 2\right), \tag{5.18}$$

where $\bar{\boldsymbol{C}}_\gamma = \bar{\boldsymbol{F}}_\gamma^T\bar{\boldsymbol{F}}_\gamma$. This corresponds to a first Piola-Kirchhoff stress of (based on $\tilde{\Psi}_\gamma$)

$$\bar{\boldsymbol{P}}_\gamma = \frac{\partial\tilde{\Psi}_\gamma}{\partial\bar{\boldsymbol{F}}_\gamma} = \mu\frac{1-c_o}{1+c_o}\bar{\boldsymbol{F}}_\gamma. \tag{5.19}$$

This solution is equivalent to the energy function describing the (perfectly) incompressible Neo-Hookean material described in Equation 2.48 but with modified coefficient by a factor of $\frac{1-c_o}{1+c_o}$. However, from Equation 5.16, the overall first Piola-Kirchhoff stress is given as

$$\bar{\boldsymbol{P}} = \frac{\partial\tilde{\Psi}}{\partial\bar{\boldsymbol{F}}}(\bar{\boldsymbol{F}}_\gamma) = \mu\frac{1-c_o}{1+c_o}\left(\bar{\boldsymbol{F}}_\gamma - \bar{\boldsymbol{F}}_\gamma^{-T}\right). \tag{5.20}$$

Equations 5.19 and 5.20 are not to be confused as the former corresponds to the stress obtained from an incompressible energy function (see [21] for the formulation using principle stretches) while the latter is the stress obtained when a volume-preserving deformation, in this case shear deformation, is applied to a solid with energy function $\tilde{\Psi}$ and for this reason, the latter is to be used in the present work.

Under in-plane hydrostatic deformation, that is

$$\bar{\boldsymbol{F}}_\alpha = \begin{bmatrix} \alpha & 0 \\ 0 & \alpha \end{bmatrix}, \tag{5.21}$$

the analytical solution in Equation 5.15 is reduced to

$$\tilde{\Psi}(\bar{\boldsymbol{F}}_\alpha, c_o) = \frac{\mu}{2}(\bar{J}_\alpha - 1)\left[\ln\left(\frac{\bar{J}_\alpha + c_o - 1}{c_o}\right) - \ln\bar{J}_\alpha\right], \tag{5.22}$$

where $\bar{J}_\alpha = \det\bar{\boldsymbol{F}}_\alpha$. This is the same result obtained by Lopez-Pamies *et al.* (2012) [22] based on the *composite spheres assemblage model* introduced initially by Hashin (1985) [8] and it was employed by Lopez-Pamies and Ponte Castañeda (2004) [19] for porous RVEs under hydrostatic loading. The first Piola-Kirchhoff stress corresponding to the energy function 5.22 is

$$\begin{aligned}\bar{\boldsymbol{P}} = {}& \frac{\mu}{2}\bar{J}_\alpha\left[\ln\left(\frac{\bar{J}_\alpha + c_o - 1}{c_o}\right) - \ln\bar{J}_\alpha\right]\bar{\boldsymbol{F}}_\alpha^{-T} \\ & + \frac{\mu}{2}(\bar{J}_\alpha - 1)\left(\frac{\bar{J}_\alpha}{\bar{J}_\alpha + c_o - 1} - 1\right)\bar{\boldsymbol{F}}_\alpha^{-T}.\end{aligned} \tag{5.23}$$

5.3.3 Analytical Solution for Incompressible Neo-Hookean Solids with Rigid Inclusions

Lopez-Pamies (2010) successfully obtained an analytical solution for incompressible hyperelastic solids with rigid inclusions [20]. It basically uses *iterated dilute homogenization* to obtain the effective strain energy function of the overall material. That is, it is assumed that, at each iteration i, the material is formed of a hyperelastic matrix phase with energy function Ψ and a *dilute* random rigid phase of infinitesimal volume fraction f_i, in the reference configuration. The overall behavior at iteration i is described by the behavior of the material in the previous iteration in addition to a term accounting for the effect of the rigid phase. This can be expressed as

$$\tilde{\Psi}_i = \tilde{\Psi}_{i-1} + \mathscr{G}(\tilde{\Psi}_{i-1}, \bar{\boldsymbol{F}}) f_i, \tag{5.24}$$

where $\mathscr{G}$ is, as defined in [20], a functional operator with respect to $\tilde{\Psi}_{i-1}$ and a function with respect $\bar{\boldsymbol{F}}$ and it is yet to be determined. The infinitesimal volume fraction f_i is related the finite volume fraction c_i as

$$f_i = \frac{c_i - c_{i-1}}{1 - c_{i-1}}. \tag{5.25}$$

From Equations 5.24 and 5.25, and using the fact that the difference $c_i - c_{i-1}$ is infinitesimal, Equation 5.24 is reduced to the following *initial value problem*.

> An effective energy function that satisfies
>
> $$(1-c)\frac{\partial \tilde{\Psi}}{\partial c}(\bar{\boldsymbol{F}}, c) - \mathscr{G}(\tilde{\Psi}, \bar{\boldsymbol{F}}) = 0, \text{ with } \tilde{\Psi}(\bar{\boldsymbol{F}}, 0) = \Psi(\bar{\boldsymbol{F}}), \tag{5.26}$$
>
> for a *random* distribution of *isotropic* rigid inclusions of volume fraction c, is to be found.

The characterization of the overall behavior depends on the choice of $\mathscr{G}$. For the specific class of *infinite-rank laminates* [7, 11], this can be found analytically.

Lopez-Pamies applied the previous problem to a two-dimensional incompressible Neo-Hookean solid with rigid inclusions described by the energy function 2.48 [20]. For the incompressible case, the deformation gradient can be expressed in terms of its principal stretches $\bar{\boldsymbol{F}} = \bar{\boldsymbol{F}}(\bar{\lambda}, \bar{\lambda}^{-1})$ which satisfies the condition of incompressibility, $\bar{J} = \det \bar{\boldsymbol{F}} = \bar{\lambda}\bar{\lambda}^{-1} = 1$. It was shown in [20] that $\mathscr{G} = 2\tilde{\Psi}(\bar{\lambda}, c)$ for this case. The solution for problem 5.26 is then obtained as

$$\tilde{\Psi}(\bar{\lambda}, c) = \frac{\mu}{2(1-c)^2}(\bar{\lambda}^2 + \bar{\lambda}^{-2} - 2). \tag{5.27}$$

For the purpose of this work, the tensor form of Equation 5.27 is required. Similar to Equation 2.48, Equation 5.27 can be expressed as

$$\tilde{\Psi}(\bar{\boldsymbol{C}}, c) = \frac{\mu}{2(1-c)^2}\left(\operatorname{tr} \bar{\boldsymbol{C}} - 2\right) \text{ with } \bar{J} = \det \bar{\boldsymbol{F}} = 1, \tag{5.28}$$

where in the above equation, the condition of incompressibility has to be satisfied for it to be valid.

As the rigid inclusion as well as the matrix phase are incompressible, volume-preserving deformations are the only admissible ones, e.g. simple shear deformation, and the overall stress tensor expected under such conditions is purely deviatoric [5]. Consequently, the effective energy function can be expressed as

$$\tilde{\Psi}(\bar{\boldsymbol{C}}, c) = \hat{\tilde{\Psi}}(\bar{\boldsymbol{C}}, c) = \frac{\mu}{2(1-c)^2}\left(\operatorname{tr}\hat{\bar{\boldsymbol{C}}} - 3\right), \tag{5.29}$$

where $\hat{\bar{\boldsymbol{C}}} = \bar{J}^{-\frac{2}{3}}\bar{\boldsymbol{C}}$. It is noteworthy that the incompressibility condition is not applied directly to this equation as $\bar{J}$ is itself a function of $\bar{\boldsymbol{F}}$. The first Piola-Kirchhoff stress is obtained from Equation 5.3 as

$$\bar{\boldsymbol{P}} = \frac{\mu}{2(1-c)^2}\bar{J}^{-\frac{2}{3}}\left(\bar{\boldsymbol{F}} - \frac{1}{3}\left(\operatorname{tr}\bar{\boldsymbol{C}}\right)\bar{\boldsymbol{F}}^{-T}\right), \tag{5.30}$$

where the components of the deformation gradient tensor used in Equation 5.29 and Equation 5.30 are expressed as

$$\bar{\boldsymbol{F}} = \left[\begin{array}{cc|c} & & 0 \\ \multicolumn{2}{c|}{\bar{\boldsymbol{F}}_{2\times 2}} & 0 \\ \hline 0 & 0 & 1 \end{array}\right].$$

The purpose of this procedure is to ensure that the condition of incompressibility is embedded in the form of the effective energy function and the corresponding first Piola-Kirchhoff stress.

5.4 Validation of the Second-Order Estimate

This section provides a validation for the SOE method described in Section 5.2 against available analytical solutions. It is known that incompressibility imposes difficulties in their numerical treatment, this is why, the validation is performed for RVEs with incompressible matrix material as they are considered "critical" cases. Besides, as will be shown later, porous RVEs with compressible matrix material provide adequate results for both SOE and FE implementation.

In this section, porous RVEs with incompressible matrix in addition to RVEs with rigid inclusions and incompressible matrix material will be studied and for which the corresponding SOE are compared against the analytical solutions described in Section 5.3.

5.4.1 Porous Incompressible Neo-Hookean Solid: Analytical Estimates

Consider a porous RVE with incompressible Neo-Hookean matrix phase of volume fraction $c^{(1)}$ and with strain energy function $\Psi^{(1)}$. The initial porosity volume fraction is $c^{(2)} = c_o$.

The strain energy function of the porous phase is expressed as $\Psi^{(2)} \to 0$ [37]. It follows that $\mathbf{A}^{(2)} \to \mathbf{0}$ and $c^{(1)} = 1 - c_o$. The upper HS estimate is used in this case using $\mathbf{A}^{(1)}$ as a reference material in Equation 5.11.

The SOE implementation described in Section 5.2.2 requires the material parameters of each of the phases. The porous phase is implemented as a material with considerably low Young's modulus E and *Poisson's ratio* ν. The matrix to void Young's modulus ratio used is approximately 7000. For the matrix phase, the nearly-incompressible Neo-Hookean material is used to obtain the first Piola-Kirchhoff stress and the corresponding tangent modulus required for the computation of the SOE. The RVE is then subjected to different types of loadings as described in the following.

Simple In-plane Shear Deformation

A simple in-plane shear deformation (see Equation 5.17) is applied to the RVE described above with $\gamma \in [0, 1]$ and $c_o = 20\%$. The response of the material obtained from the SOE is then compared to the analytical solution expressed in Equation 5.20. Figure 5.2 illustrates

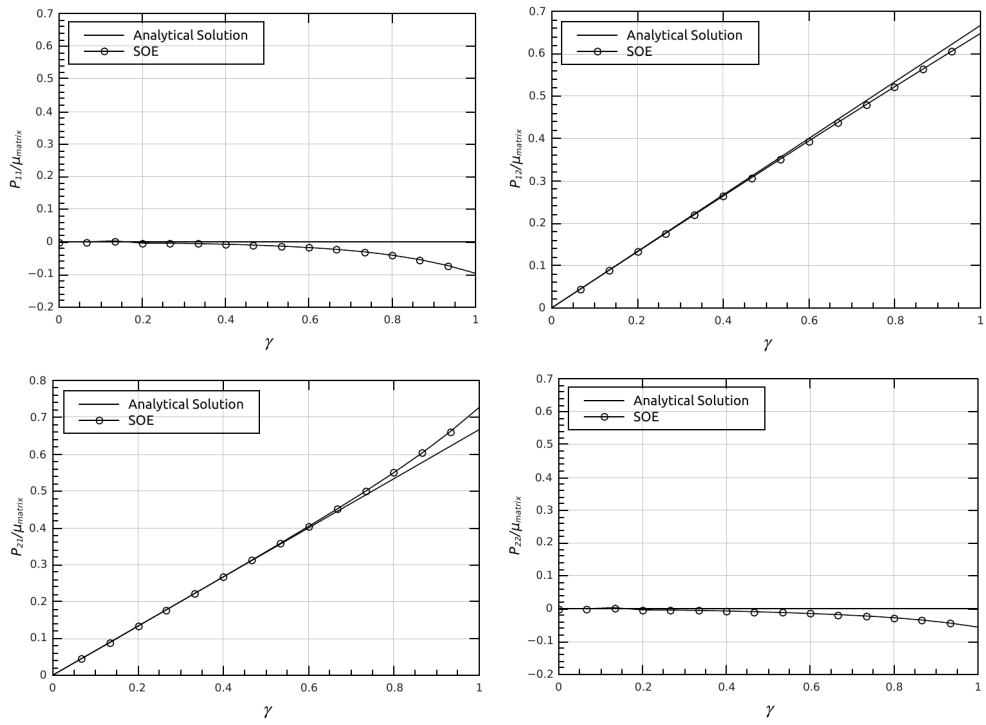

Figure 5.2: The first Piola-Kirchhoff stress components for the Second-Order Estimate and the analytical solution for a porous incompressible Neo-Hookean solid subjected to simple in-plane shear deformation. The void volume fraction used is 20%.

the response obtained from the implemented SOE plotted against the analytical solution for the present case. It is shown in this figure that the implemented SOE agrees with the analytical solution for the four components of the first Piola-Kirchhoff stress. The

maximum error is, as expected, in the diagonal components P_{11} and P_{22} that are most affected by the incompressibility condition.

In-plane Hydrostatic Deformation

The in-plane hydrostatic deformation expressed in Equation 5.21 is imposed on the RVE described earlier. The output is then plotted against the analytical solution in Equation 5.23. Two RVEs are used in this case, one with $c_o = 30\%$ and the other with $c_o = 50\%$. Figure 5.3 shows that the SOE gives the same pattern of the analytical solution. It is

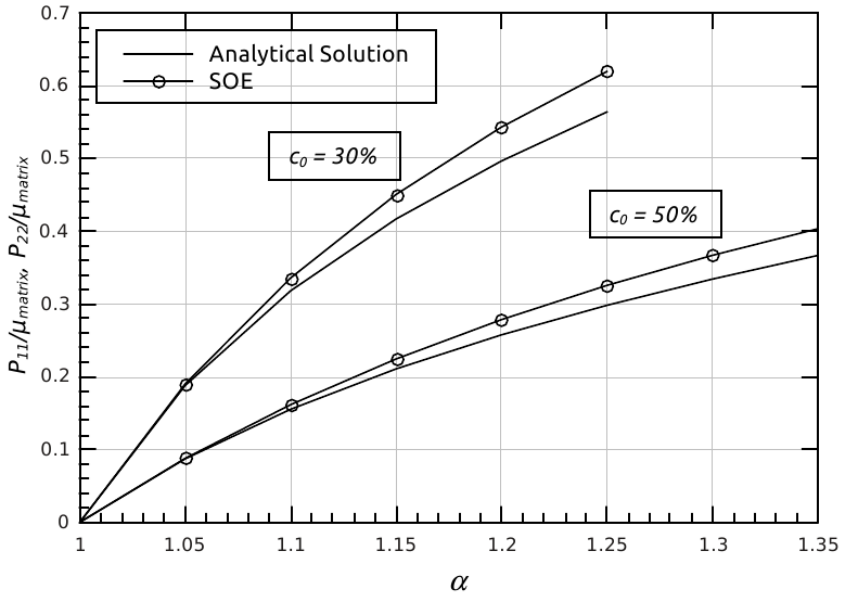

Figure 5.3: The first Piola-Kirchhoff stress for the Second-Order Estimate and the analytical solution for a porous incompressible Neo-Hookean solid subjected to in-plane hydrostatic deformation.

shown that the difference between the analytical solution and the SOE is reduced for higher porosity volume fraction. This agrees with the results obtained in [19]. Finally, and as expected, RVEs with higher void volume fractions predict a softer overall behavior.

5.4.2 Incompressible Neo-Hookean Solid with Rigid Inclusions: Analytical Estimates

Consider an RVE composed of an incompressible Neo-Hookean matrix phase of volume fraction $c^{(1)}$ and strain energy function $\Psi^{(1)}$, and a rigid inclusion phase of initial volume fraction $c^{(2)} = c$. For this case $\mathbf{A}^{(1)} < \mathbf{A}^{(2)}$, hence the lower HS estimate is used here with $\mathbf{A}^{(1)}$ being the reference material in Equation 5.11.

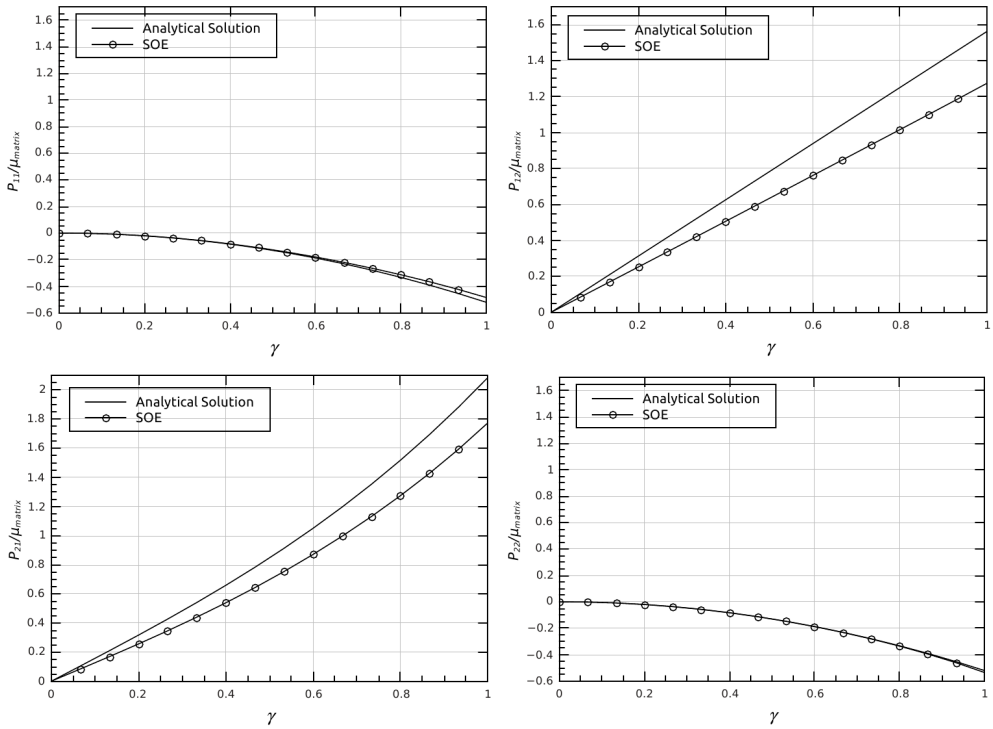

Figure 5.4: The first Piola-Kirchhoff stress components of the Second-Order Estimate and the analytical solution for a porous incompressible Neo-Hookean solid subjected to simple in-plane shear deformation. The void volume fraction used is 20%.

The SOE implementation described in Section 5.2.2 requires the material parameters of each of the phases. The rigid phase is implemented as a material with significantly large Young's modulus E and Poisson's ratio $\nu \to 0.5$. The matrix to inclusion Young's modulus ratio used is approximately 0.07. As mentioned earlier, the RVE in this case is incompressible hence only the deviatoric part of the Neo-Hookean energy function (see Equation 2.50) is used to obtain the first Piola-Kirchhoff stress and the tangent modulus of the constituents of the RVE. It is then subjected to an in-plane simple shear deformation as expressed in Equation 5.17, where $\gamma \in [0, 1]$. The inclusion volume fraction used in this case is $c = 20\%$.

Figure 5.4 shows the components of the first Piola-Kirchhoff stress obtained from the implemented SOE and the analytical solution described in Section 5.3. It can be seen that the dominant stress components P_{12} and P_{21} underestimate the composite behavior. This is consistent with the use of the Hashin-Shtrikman lower bound in this case. On the other hand, the diagonal components P_{11} and P_{22} of the SOE response show less error as, in this case, the incompressibility constraint is imposed explicitly. Figure 5.4 also shows that the current implementation of the SOE provides a better approximation of the overall behavior than that obtained by Lahellec *et al.* (2004) (using the original formulation) [14] for component P_{12} of the stress tensor. And, as will be seen later, these results are in

agreement with the homogenization-based FE results.

The proposed implementation to account for incompressibility is relatively simple compared to other suggestions in literature. For instance, Ponte Castañeda and Tiberio (2000) [34] suggested approximating the deviatoric part of the energy function of the incompressible phase using the SOE while the volumetric part is to be imposed "exactly" based on the results obtained in [38]. In addition, Lahellec *et al.* (2004) [14] proposed using *Lagrange multipliers* for the same purpose.

Chapter 6

Computational Homogenization of Hyperelastic Materials

This chapter provides numerical examples for the purpose of investigating the properties of different multi-scale models described in Section 3.3.2. In addition, a comparison with the SOE explained in Section 5.2 and the corresponding analytical solution provided in Section 5.3, if available, is performed.

First, porous RVEs are studied with a particular interest in the effect of the statistical distribution of voids on the homogenized behavior. Different material models are used for this purpose. This is then followed by a study of RVEs with incompressible matrix and rigid inclusions leading to overall incompressible RVEs in which case numerical problems arise.

6.1 Porous Hyperelastic Solids

Porosity characterizes several classes of materials, for instance, sponge-like materials and materials with voids as defects. A distinctive property of such materials is that, even if the matrix material is incompressible, the overall material is compressible. This makes their numerical treatment less problematic. Compressible and incompressible matrix materials for the porous RVE will be considered in the following.

6.1.1 Compressible Matrix Material under Simple In-plane Shear Loading

For the purpose of investigating the effect of the statistical distribution of voids in the RVE on the homogenized properties, two models were considered:

i. a square RVE with a single circular void of initial volume fraction of $c_o = 20\%$. This RVE is meshed with 1558 3-noded triangular elements and a total of 864 nodes. The corresponding mesh is shown in Figure 6.1a.

ii. The other model is a square RVE with randomly distributed circular voids with a total initial void volume fraction of $c_o = 20\%$. This RVE consists of 1558 3-noded triangular elements and 1000 nodes and the corresponding mesh is shown in Figure 6.1b.

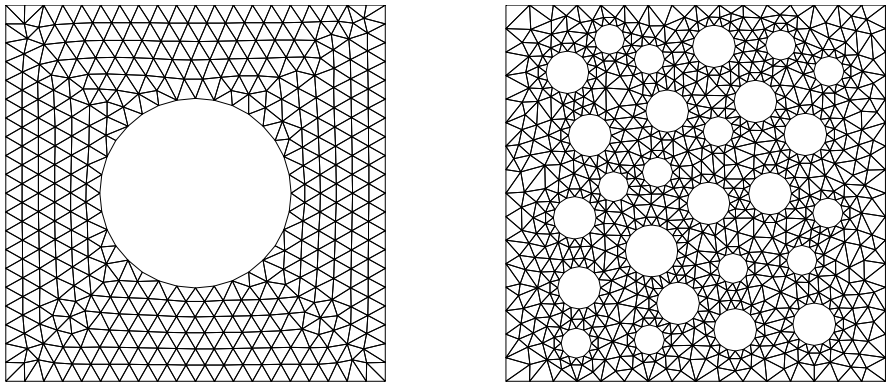

(a) Single circular void. (b) Randomly distributed voids.

Figure 6.1: Porous representative volume elements with void volume fraction of $c_o = 20\%$ meshed with 3-noded triangular elements.

Both models are made of compressible hyperelastic matrix materials, namely, compressible Neo-Hookean and Hencky materials. A simple in-plane shear deformation (see Equation 5.17) using different multi-scale models (boundary conditions), namely, the linear boundary displacement, periodic boundary displacement fluctuation and uniform boundary traction assumptions (see Section 3.3.2). The matrix material has a Poisson's ratio of $\nu = 0.2$ and $\mu = 29.2$ GPa and, for the SOE implementation, the matrix to void Young's modulus ratio used is approximately 7000. The output of the described models is plotted in Figure 6.2 for the Hencky material and in Figure 6.3 for the compressible Neo-Hookean material. The corresponding SOE is also plotted in both figures in addition to the Voigt upper bound described in Section 5.3.1.

Figures 6.2 and 6.3 show that the uniform boundary traction assumption provides the softest homogenized behavior for both RVEs as it is the least constrained. On the other hand, the linear boundary displacements model gives the stiffest as it is the most constrained while periodic boundary fluctuations model predicts a behavior that lies between the former models. This agrees with the results obtained in [33] for small strains. In addition, it is noted that the homogenized response converges with the increase of the statistical sample, i.e. the band formed by the homogenized results based on RVEs with random distribution of voids is narrower in this case. This is in agreement with the results obtained in [33] and [12].

The SOE supports the results as it lies in the vicinity of the random distribution RVE results except for component P_{11} at larger values of shear where the SOE falls outside this

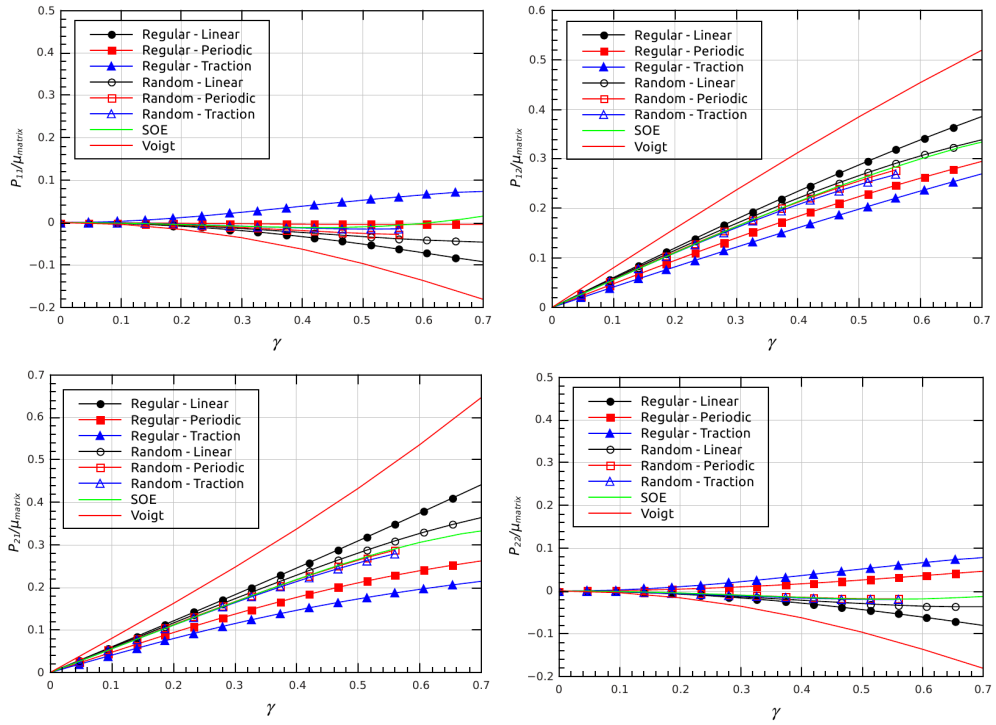

Figure 6.2: Comparison between different multi-scale models for an RVE with a single circular void and another with randomly distributed voids both with initial void volume fraction of $c_o = 20\%$ and Hencky matrix material. The behavior obtained from the SOE and the Voigt upper bound are also provided.

band. On the other hand, the Voigt bound predicts a behavior that is stiffer than any of the homogenized results, hence giving an upper bound. It is to be noted here that the SOE gives adequate behavior for all four components of stress in contrast to other cases that will be described in the following sections.

Figure 6.4 shows the deformation of both RVEs with Hencky matrix material under the periodic boundary fluctuation assumption. It can be seen that the elements in the RVE with random distribution of voids under a shear of $\gamma = 0.56$ become highly distorted and continuous remeshing is required to obtain appropriate results for higher values of shear. This also occurs when using the uniform boundary traction model. For that reason, the plots in Figure 6.2 for these models are not available for shear values higher than $\gamma = 0.56$. Figure 6.5 illustrates the distribution of stress P_{12} for both RVEs with compressible Neo-Hookean matrix material. It is to be noted that the stresses plotted correspond to the average of the stress values of the Gauss points in each element.

Tables 6.1 and 6.2 show the residual values required to obtain the solution for both RVEs with compressible Neo-Hookean matrix material at a shear magnitude of $\gamma = 0.56$. These values confirm that the N-R algorithm converges quadratically for all multi-scale models. However, the convergence is more difficult for RVEs with random distribution of voids as implied by the increased number of iterations to reach convergence.

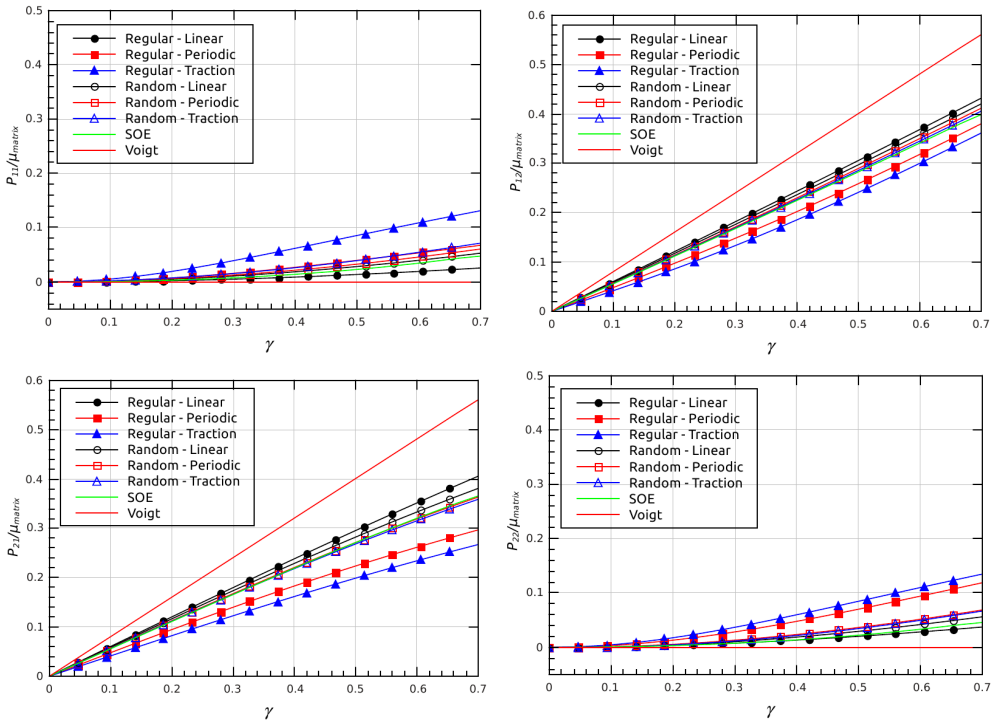

Figure 6.3: Comparison between different multi-scale models for an RVE with a single circular void and another with randomly distributed voids both with initial void volume fraction of $c_o = 20\%$ and compressible Neo-Hookean matrix material. SOE and the Voigt upper bound are plotted for comparison.

	Linear BC	**Periodic BC**	**Traction BC**
1	9.036×10^{-2}	1.488×10^{-1}	1.459×10^{-1}
2	4.015×10^{-3}	9.539×10^{-3}	6.441×10^{-3}
3	5.164×10^{-6}	2.813×10^{-5}	8.190×10^{-6}
4	5.629×10^{-11}	2.813×10^{-10}	5.271×10^{-11}

Table 6.1: Residual values of a representative volume element with a single void and compressible Neo-Hookean matrix material at a shear of $\gamma = 0.56$.

6.1.2 Incompressible Matrix Material under Simple In-plane Shear Loading

Porous RVEs with compressible matrix material are discussed above. Similarly, two porous RVEs are built with 20% void volume fraction, one having one single void and the other consists of a random distribution of voids. Both RVEs consist of an incompressible Neo-Hookean matrix material with a Poisson's ratio of $\nu = 0.49$ and $\mu = 23.5$ GPa and subjected to in-plane simple shear. The matrix to void Young's modulus ratio used is approximately 7000 for the SOE implementation.

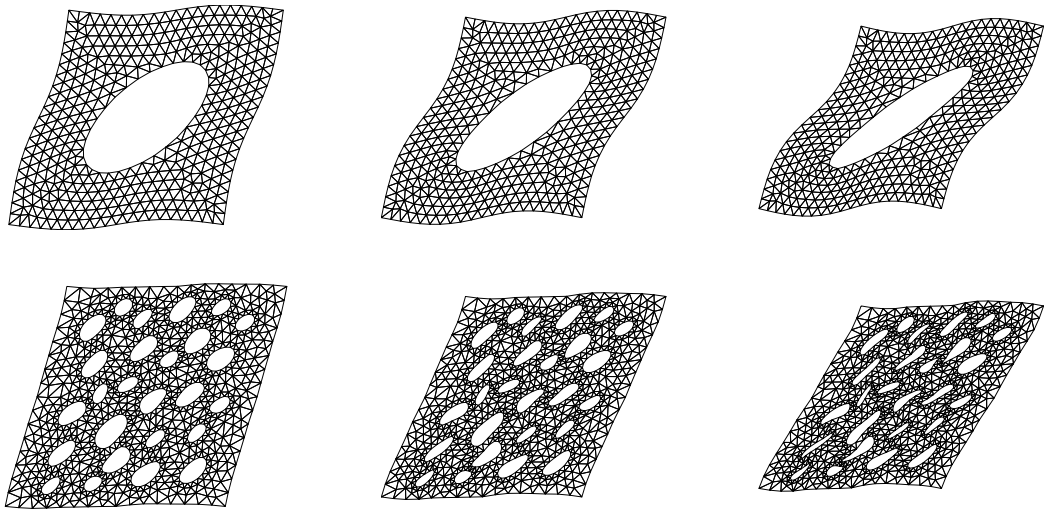

Figure 6.4: Deformation of two porous representative volume elements with compressible Hencky matrix material and a void volume fraction of $c_o = 20\%$. One consists of a single void (first row) and the other is formed of a random distribution of voids (second row) under different magnitudes of shear, $\gamma = 0.28$, 0.42, and 0.56 (from left to right respectively) using the periodic boundary fluctuation assumption.

	Linear BC	**Periodic BC**	**Traction BC**
1	1.622×10^{-1}	2.030×10^{-1}	1.561×10^{-1}
2	9.166×10^{-3}	1.368×10^{-2}	1.030×10^{-2}
3	1.370×10^{-4}	3.106×10^{-4}	2.001×10^{-4}
4	1.489×10^{-7}	7.697×10^{-7}	5.047×10^{-7}
5	1.465×10^{-13}	1.565×10^{-12}	6.077×10^{-13}

Table 6.2: Residual values of a representative volume element with randomly distributed voids and compressible Neo-Hookean matrix material at a shear of $\gamma = 0.56$.

The RVE with a single void is meshed with 896 4-noded quadrilateral elements with F-bar formulation and a total of 1001 nodes. The RVE with random distribution of voids is meshed with 778 4-noded quadrilateral F-bar elements and 1006 nodes. F-bar elements, formulated by de Souza Neto *et al.* [3, 6] and described in detail in [5], are known to be suitable for meshing incompressible materials to avoid *volumetric locking* leading to overstiff results.

The resulting homogenized behavior is then plotted against the corresponding SOE in Figure 6.6 while Figure 6.7 shows the deformation of the RVE with a single void under the uniform boundary traction model at different values of shear deformation γ.

It is shown in Figure 6.6 that, as expected, the stresses obtained in this case are higher than those obtained using compressible matrix phase (see Figure 6.3). Figure 6.6 shows

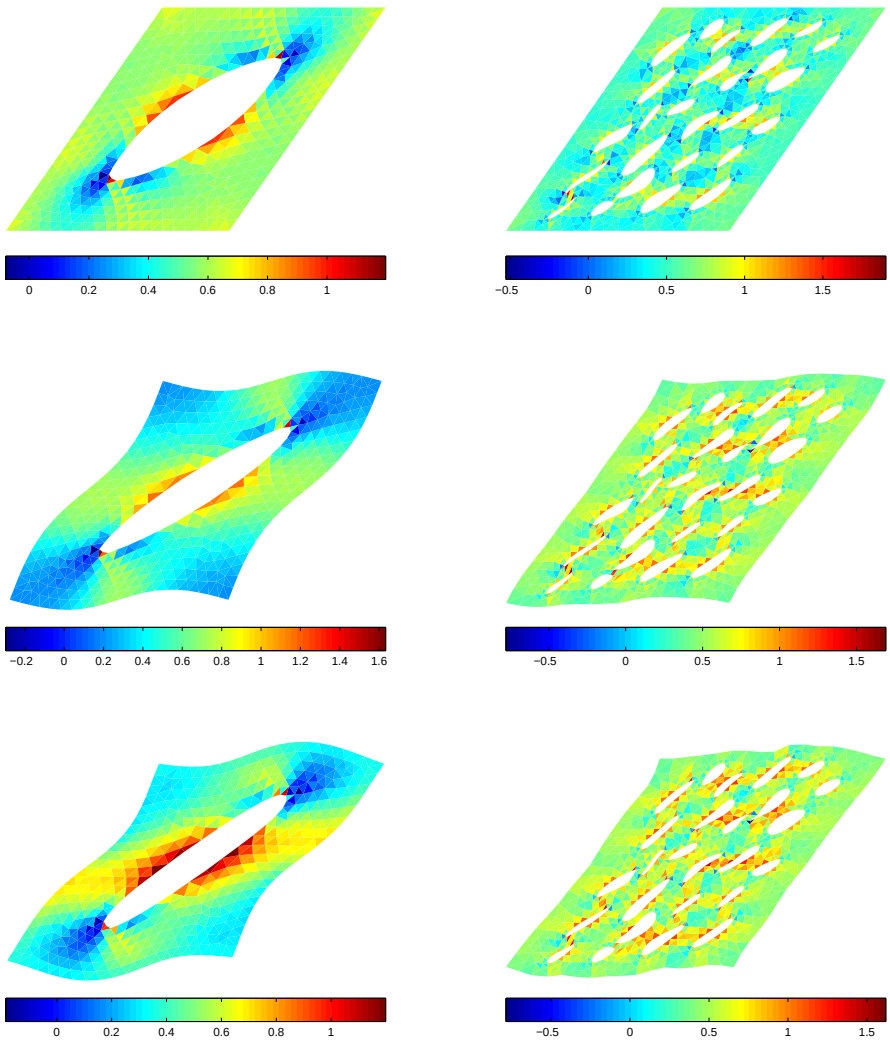

Figure 6.5: Shear component of the first Piola-Kirchhoff stress (P_{12}/μ) of two porous representative volume elements with compressible Neo-Hookean matrix material and a void volume fraction of $c_o = 20\%$. One consists of a single void (left) and the other is formed of a random distribution of voids (right). These are subjected to the linear boundary displacement assumption (first row), the periodic boundary fluctuation assumption (second row), and the uniform boundary traction assumption (third row) at a shear of $\gamma = 0.7$.

that, again, the RVE with random distribution of voids under different multi-scale models provides converged results for the homogenized behavior hence giving the narrower band described earlier. Moreover, the analytical solution described in Section 5.3.2 lies in this band implying that results based on the homogenization theory are successful in predicting the behavior of heterogeneous materials with an error depending on the type of the model used. In addition, the SOE predicts a behavior that agrees with the analytical solution and

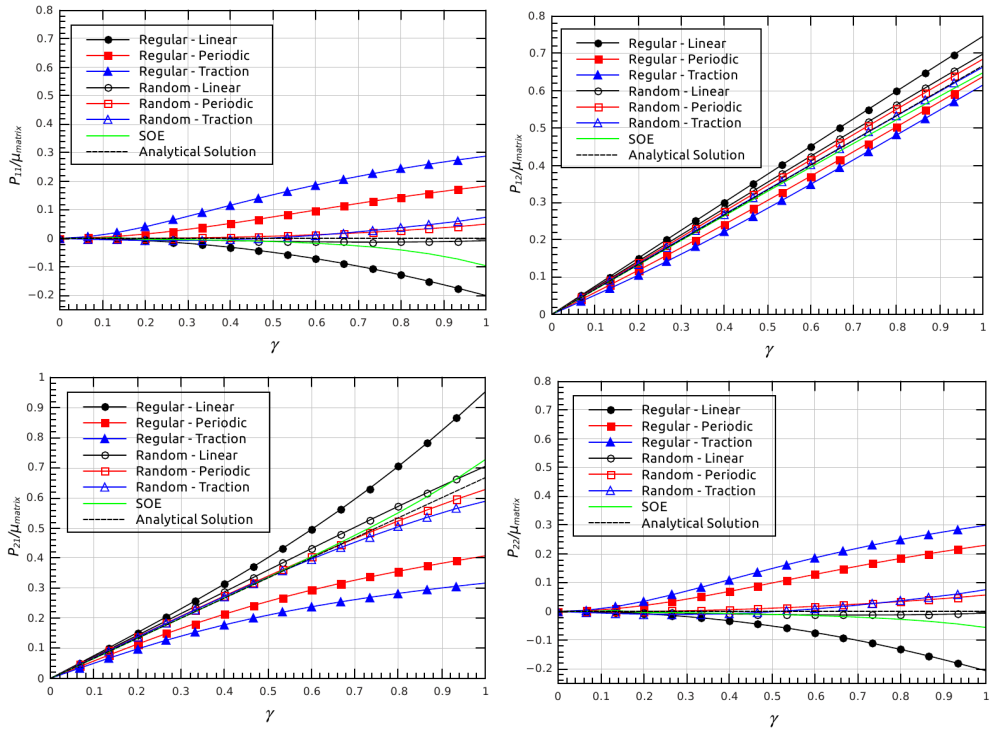

Figure 6.6: Comparison between different multi-scale models for an RVE with a single circular void and another with randomly distributed voids both with initial void volume fraction of $c_o = 20\%$ and incompressible Neo-Hookean matrix material. SOE and analytical solution are also plotted for comparison.

the homogenization-based results for the stress components dominated by the deformation P_{12} and P_{21}. while other stress components are predicted with a larger error.

	Linear BC	**Periodic BC**	**Traction BC**
1	6.863×10^{-1}	1.238×10^{0}	
2	3.813×10^{-2}	2.219×10^{-1}	
3	1.682×10^{-3}	2.219×10^{-1}	
4	1.313×10^{-6}	4.764×10^{-2}	Sub-incrementation required.
5	3.010×10^{-12}	4.603×10^{-4}	
6		1.153×10^{-6}	
7		2.525×10^{-12}	

Table 6.3: Residual values of a representative volume element with a single void and incompressible Neo-Hookean matrix material at a shear of $\gamma = 0.6$.

Table 6.3 shows the values of the residual to obtain the solution for the RVE with a single void using different multi-scale models at $\gamma = 0.6$. It is concluded from these values that, while quadratic convergence is conserved, the convergence is more difficult for an RVE

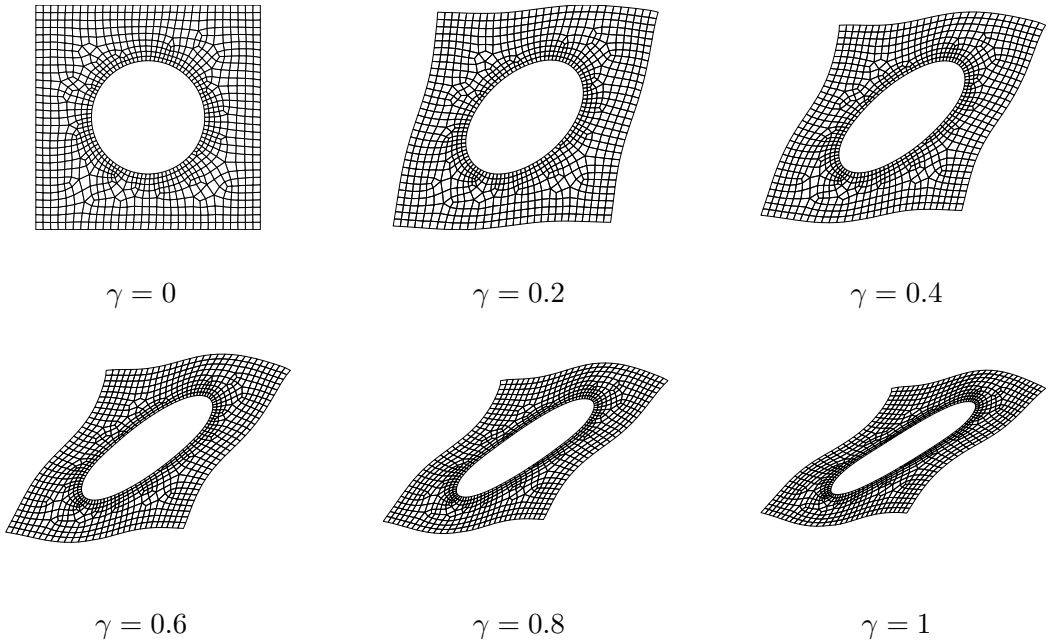

Figure 6.7: Deformation of porous representative volume element with incompressible Neo-Hookean matrix material and single void of volume fraction of $c_o = 20\%$ under different magnitudes of shear using the uniform boundary traction assumption.

with incompressible matrix material than that with compressible matrix (see Table 6.1) as implied by the increased number of iterations in this case. One can also deduce that, while this is not obvious in Table 6.1, convergence becomes more difficult with increasing the number of dofs to be solved for which is the case when using the uniform boundary traction model. As shown in Table 6.3, the uniform boundary traction model in this case requires the use of sub-incrementation.

An important parameter when dealing with incompressible materials is the pressure. The element type used has to ensure that reasonable output for the pressure is obtained[1]. Figure 6.8 shows contour plots of the pressure and the corresponding P_{12} for the RVE with a single void using the uniform boundary traction assumption at $\gamma = 1$. The pressure plots illustrated in Figure 6.8 do not show high pressure gradients between elements as expected from low-order elements (e.g. 3-noded triangular elements). The F-bar formulation used is the reason for that.

6.1.3 Incompressible Matrix Material under In-plane hydrostatic Loading

Interesting results concerning the properties of the multi-scale models are obtained from porous RVE subjected to in-plane hydrostatic loading (see Equation 5.21). Two porous

[1]This is discussed in detail in Section 6.3.

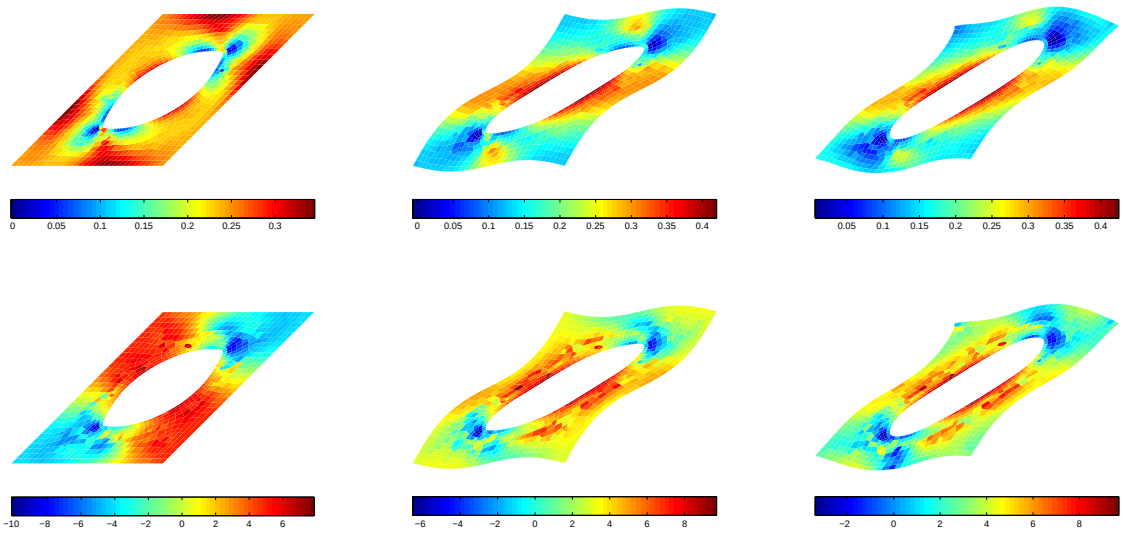

Figure 6.8: Shear component of the first Piola-Kirchhoff stress (P_{12}/μ) (first row) and the pressure values (second row) for a representative volume element with a single void of $c_o = 20\%$ volume fraction. This is subjected to a shear of magnitude $\gamma = 1$ using the linear boundary displacement assumption (first column), the periodic boundary fluctuation assumption (second column) and uniform boundary traction (third column).

RVEs were constructed with a single void, one with 30% and the other with 50% volume fraction. Both RVEs are made of incompressible Neo-hookean matrix material which is meshed using 4-noded F-bar quadrilateral elements. The RVE with $c_o = 30\%$ is meshed with 498 elements and 586 nodes while the one with $c_o = 50\%$ has 537 elements and 660 nodes as shown in Figure 6.9.

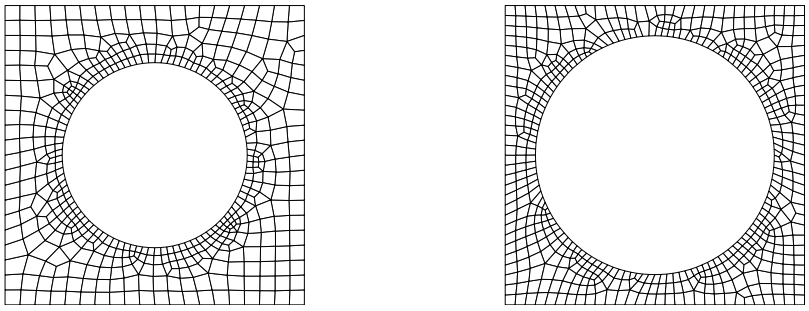

(a) $c_o = 30\%$ (b) $c_o = 50\%$

Figure 6.9: Porous representative volume elements with different volume fractions meshed with 4-noded quadrilateral elements.

Figure 6.10 plots the homogenized behavior of both RVEs using different boundary conditions in addition to the corresponding SOE and analytical solution described in Section 5.3. Results concerning the properties of different multi-scale models are furthermore con-

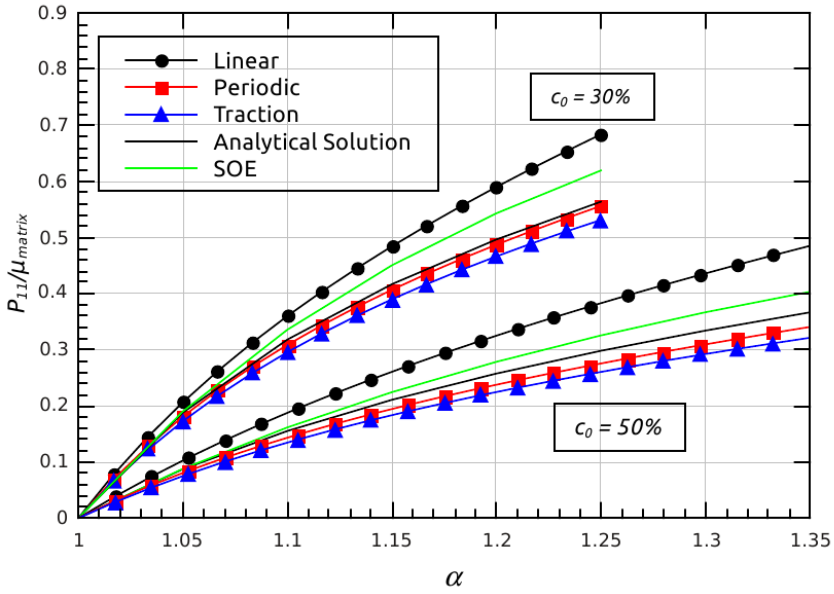

Figure 6.10: The first Piola-Kirchhoff stress for the homogenized behavior, the Second-Order Estimate (SOE), and the analytical solution for a porous incompressible Neo-Hookean solid subjected to hydrostatic deformation of magnitude α.

cluded from Figure 6.10. In addition, it is noted that the error between the homogenized behavior and the analytical solution increases for RVEs with higher porosity volume. In this case, the void is closer to the boundaries of the RVE which contradicts the fundamental assumption of the homogenization theory requiring the heterogeneity or the second phase to be far enough from the boundaries of the RVE so that the boundary conditions applied do not affect the homogenized behavior. This can be illustrated clearly in Figure 6.11 from the deformed RVE. Figure 6.11 also shows the distribution of stress for component P_{11} for the RVE with 50% void volume fraction at $\alpha = 1.35$ under different multi-scale models.

Figure 6.12 shows the deformation of the RVE with 30% void volume fraction at different values of α under different boundary conditions. Although the periodic boundary fluctuations model renders deformed RVEs with straight boundaries as the ones obtained from the linear boundary displacements model, their homogenized results are significantly. This is explained by the fact that, under the linear BC, the dofs are entirely fixed, while, under the periodic BC, the boundary dofs of the boundaries are free to move but with the periodicity condition. This is emphasized in Figure 6.13 where it is clearly shown that the nodes of both models do not coincide, thus giving different responses.

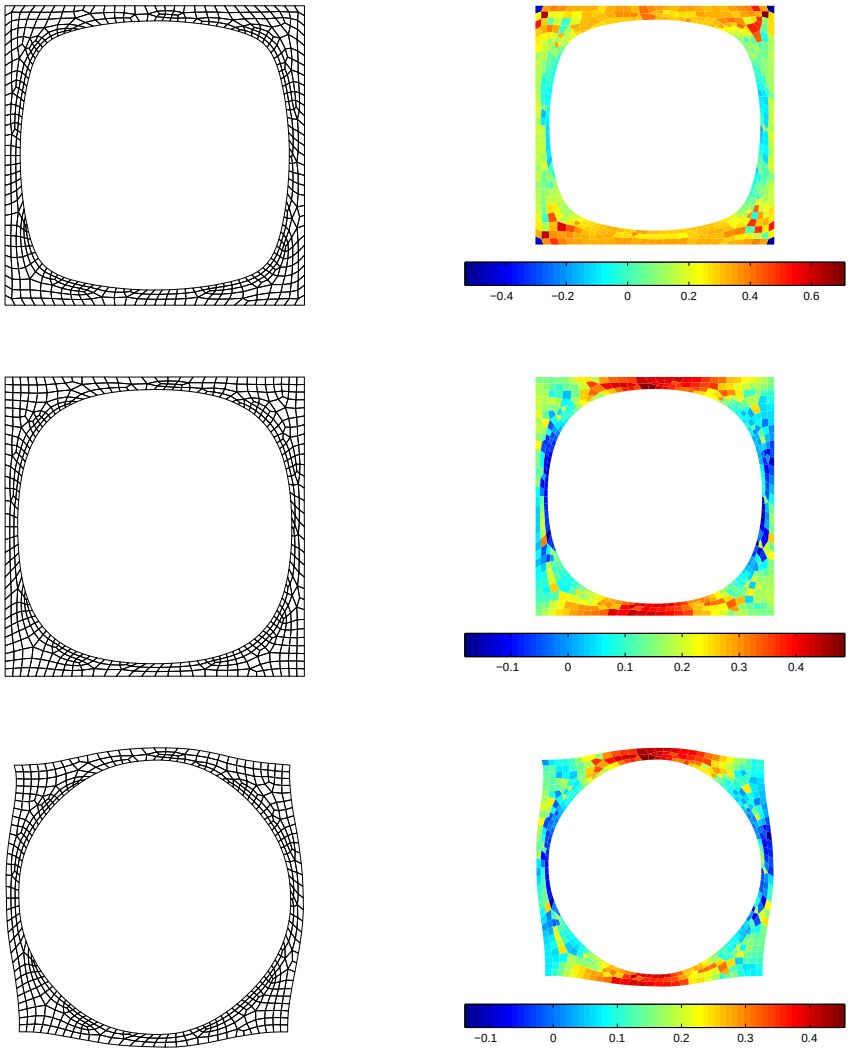

Figure 6.11: Deformation (right) and the first Piola-Kirchhoff stress (P_{11}/μ) of a representative volume element with 50% void volume fraction subjected to in-plane hydrostatic loading of magnitude $\alpha = 1.35$ using the linear boundary displacement assumption (first row), the periodic boundary fluctuation assumption (second row) and uniform boundary traction (third row).

6.2 Incompressible Hyperelastic Solids with Rigid Inclusions

This section is concerned with the behavior of solids consisting of incompressible matrix material and rigid inclusions. The models used consist of 1181 elements and 1242 nodes for the RVE with a single inclusion, and 3896 elements and 4005 nodes for the RVE with

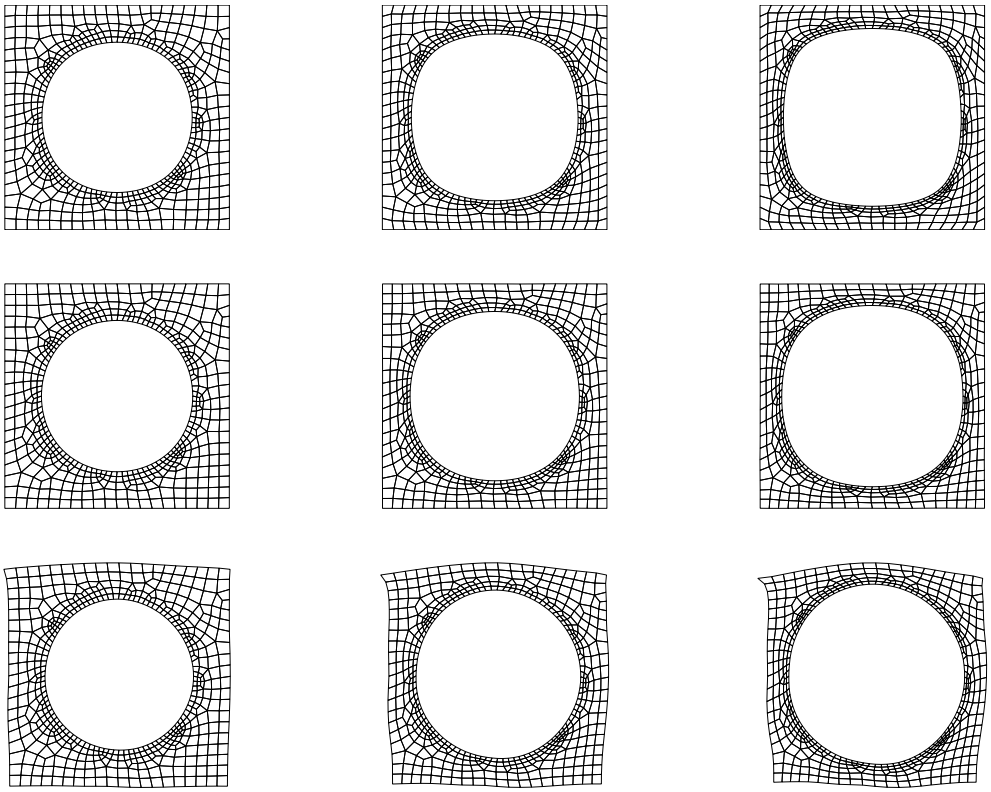

$\alpha = 1.05$ $\alpha = 1.15$ $\alpha = 1.25$

Figure 6.12: Deformation of a representative volume element subjected to in-plane hydrostatic loading of magnitude α using the linear boundary displacement assumption (first row), the periodic boundary fluctuation assumption (second row) and uniform boundary traction (third row). The initial void volume fraction used is $c_o = 30\%$.

randomly distributed inclusions both with $c = 20\%$ inclusion volume fraction (see Figure 6.14). Both RVEs are meshed with 4-noded quadrilateral elements with F-bar formulation and subjected to simple in-plane shear with $\gamma \in [0, 1]$.

Figure 6.15 shows the homogenized behavior obtained from both RVEs in addition to the SOE and the analytical solution available for this case (see Section 5.3.3). It can be seen in Figure 6.15 that the homogenized behavior form a wider band for both RVEs compared to the previously described cases. It is also shown that the periodic boundary fluctuations model converges to the analytical solution for all components of stress. The reason for this is that most analytical solutions are derived based on the assumption of periodic materials. The homogenized responses obtained also confirms that the higher the statistical sample the more accurate the results.

As explained in Section 5.3.3, the SOE behavior in this case provides a good approximation of the behavior with higher error in the dominant components, namely P_{12} and

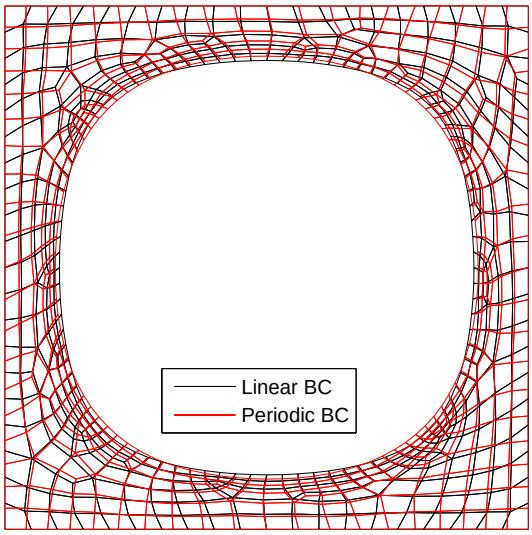

Figure 6.13: Deformed mesh of two representative volume elements under the linear boundary displacement assumption (black) and the periodic boundary fluctuation assumption (red) at $\alpha = 1.25$.

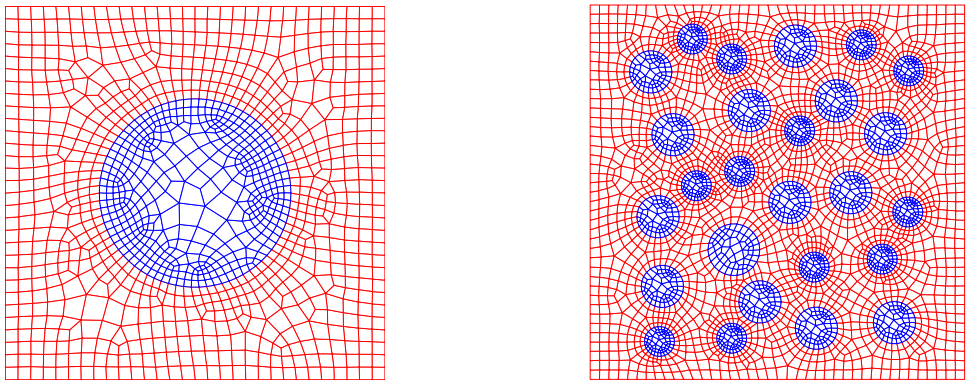

(a) Single circular inclusion. (b) Randomly distributed inclusions.

Figure 6.14: Solid with a single rigid inclusion.

P_{21}. Similar to the previous cases, the SOE gives a behavior that falls in the band formed by the RVE with random distribution of inclusions subjected to the different multi-scale models as expected. It also shows higher values of error with respect to the analytical solution compared to the previously described cases, but this is consistent with the wider band formed by the homogenized results. In other words, the homogenized results and the

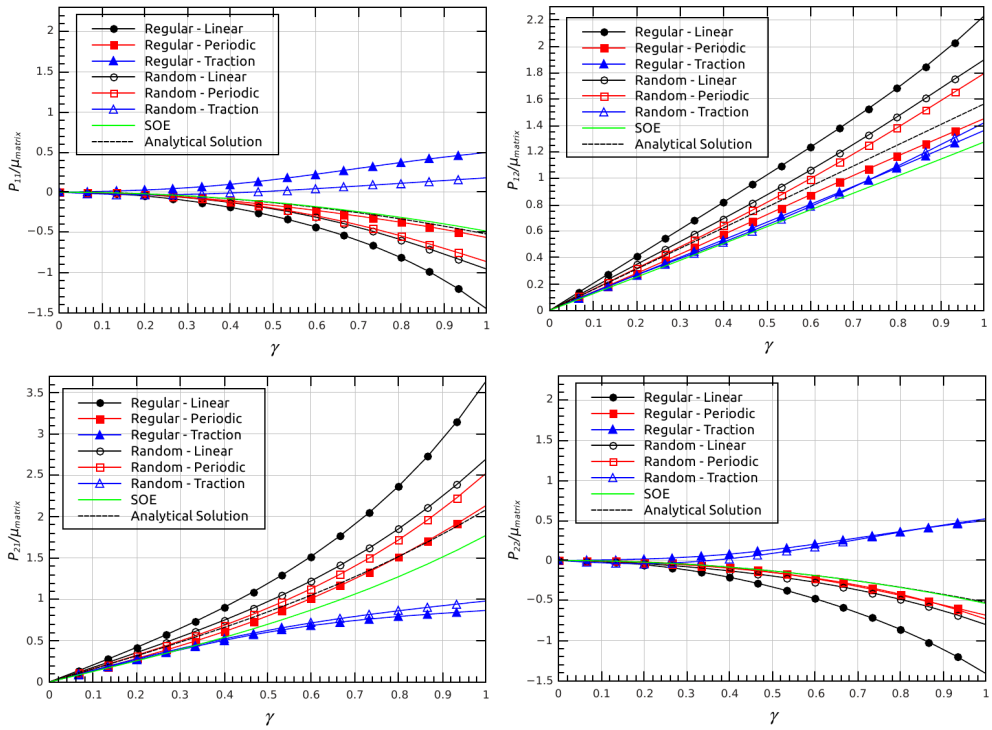

Figure 6.15: Comparison between different multi-scale models for a solid with a single rigid inclusion of initial volume fraction of $c = 20\%$ and incompressible Neo-Hookean matrix material. These are also compared to the SOE and the analytical solution.

SOE include larger values of error as the incompressibility condition imposes additional constraint over the RVE.

Figure 6.16 shows the deformation of the RVE with a single inclusion at different values of shear for different multi-scale models while Figure 6.17 shows the distribution of component P_{12} of the first Piola-Kirchhoff stress and the corresponding pressure distribution at $\gamma = 1$.

Table 6.4 shows the quadratic convergence of the N-R procedure used to solve the problem at a shear of $\gamma = 0.6$ using different multi-scale models. It can be concluded that the convergence is faster using the linear boundary displacements model as it requires less number of iterations than the uniform boundary traction model and it reaches a lower exponential value (10^{-11}) than the periodic boundary fluctuations model for the same number of iterations.

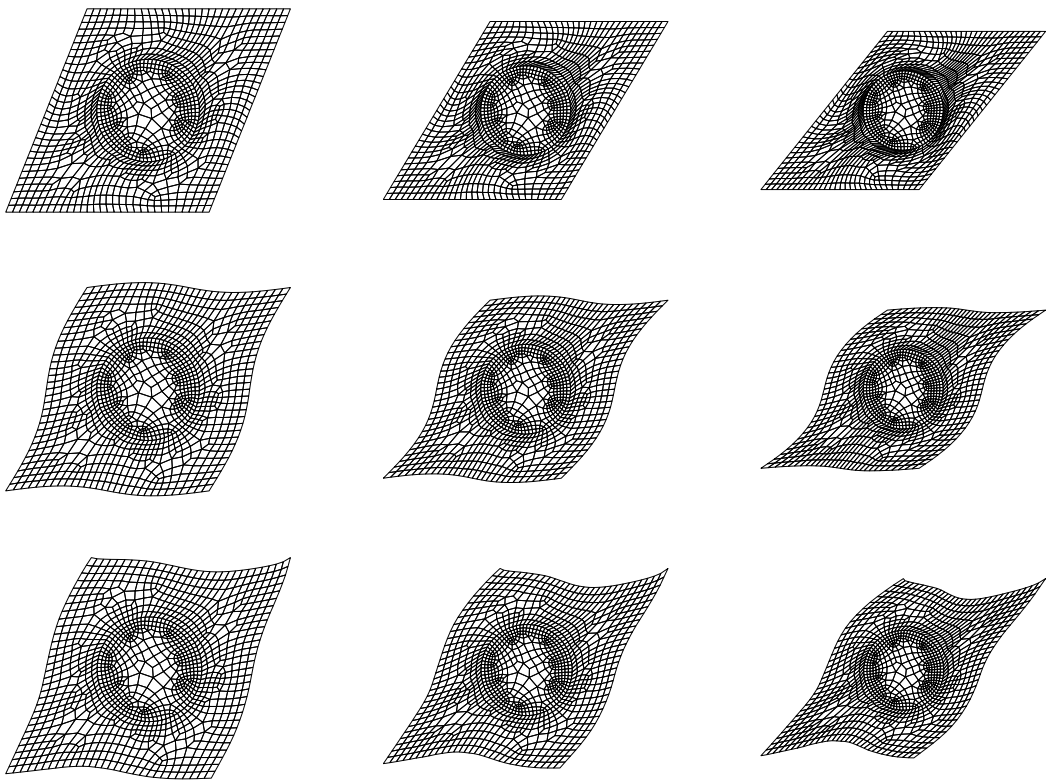

$\gamma = 0.4$ $\gamma = 0.6$ $\gamma = 0.8$

Figure 6.16: Deformation of a representative volume element with a single rigid inclusion subjected to in-plane simple shear loading of magnitude γ using the linear boundary displacement assumption (first row), the periodic boundary fluctuation assumption (second row) and uniform boundary traction (third row). The inclusion volume fraction used is $c = 20\%$.

	Linear BC	**Periodic BC**	**Traction BC**
1	$6.453 \times 10^{+1}$	$8.851 \times 10^{+1}$	$7.370 \times 10^{+1}$
2	$1.103 \times 10^{+1}$	$2.135 \times 10^{+1}$	$1.461 \times 10^{+1}$
3	2.102×10^{0}	3.460×10^{0}	3.893×10^{0}
4	1.693×10^{-2}	7.999×10^{-2}	4.737×10^{-1}
5	1.106×10^{-1}	3.439×10^{-1}	1.884×10^{-1}
6	1.071×10^{-5}	5.151×10^{-4}	2.216×10^{-2}
7	9.060×10^{-8}	1.898×10^{-5}	3.394×10^{-5}
8	5.701×10^{-11}	1.128×10^{-10}	6.087×10^{-8}
9			1.101×10^{-10}

Table 6.4: Residual values of a representative volume element with a single rigid inclusion and incompressible Neo-Hookean matrix material at a shear of $\gamma = 0.6$.

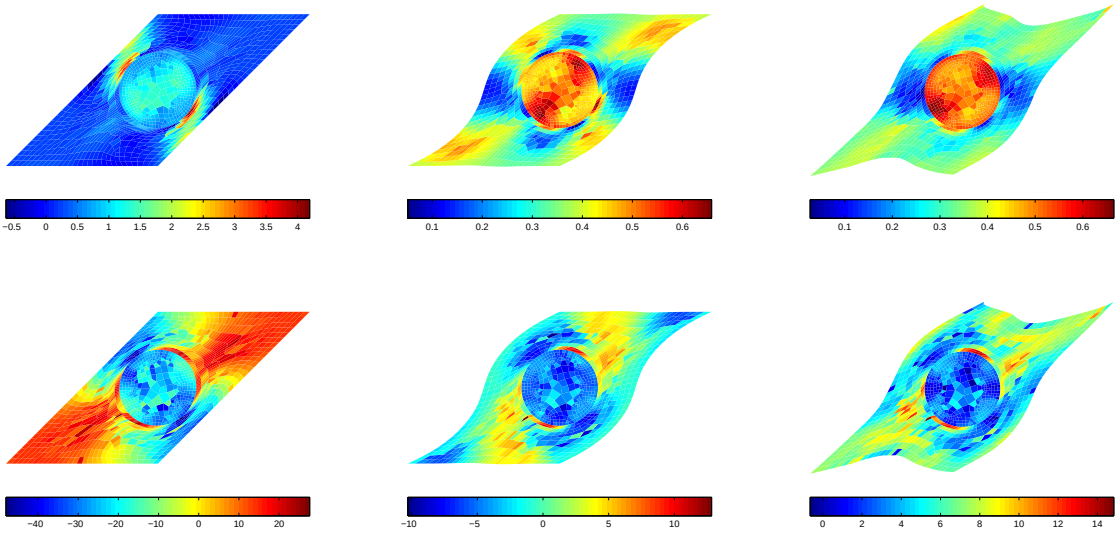

Figure 6.17: Shear component of the first Piola-Kirchhoff stress (P_{12}/μ) (first row) and the pressure values (second row) for a representative volume element with a single rigid inclusion of $c = 20\%$ volume fraction, subjected to a shear of magnitude $\gamma = 1$ using the linear boundary displacement assumption (first column), the periodic boundary fluctuation assumption (second column) and uniform boundary traction (third column).

6.3 Remarks on Finite Element Implementation

This section studies the effect of the element type used to discretize the RVE on the resulting behavior. This was motivated by the use of incompressible materials where, in such cases, it is known that low-order elements provide poor results, in particular, showing volumetric locking. A possible solution for such problem is to employ higher order elements, for instance, 8-noded quadrilateral elements.

For this purpose, different finite elements are used to discretize a porous RVE with void volume fraction of 20% and incompressible Neo-Hookean matrix materials. These are, namely, 3-noded triangular elements (TRI3), 4-noded quadrilateral elements (Q4), 4-noded quadrilateral elements with F-bar formulation (Q4FBAR), and 8-noded quadrilateral elements with full integration (Q8FI). These elements are illustrated in Figure 6.18 (except Q4FBAR).

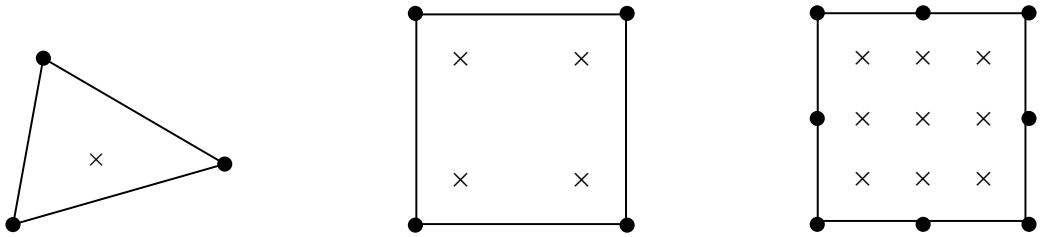

(a) TRI3 (b) Q4 (c) Q8FI

Figure 6.18: Different finite elements. (×) denotes a Gauss point and (•) denotes a node.

The homogenized behavior obtained using the described elements under the linear boundary displacement assumption is shown in Figure 6.19 which suggests that the error in stress is relatively small. However, the use of different elements is justified by the pressure plots shown in Figures 6.20, 6.21 and 6.22. It can be seen in Figure 6.20, for example, the pressure varies significantly in magnitude and distribution using different element types. This can be accounted for by noting that TRI3 and Q4 show sudden changes in pressure values between elements while Q4FBAR and Q8FI do not, which makes them more suitable when dealing with incompressibility. The advantage of using F-bar elements, developed by de Souza Neto *et al.* [3, 6], is the possibility of using lower order elements and still obtain adequate results for the pressure. This is in contrast to using higher order elements which are, in general, computationally more expensive. Figures 6.21 and 6.22 show the stress and pressure distributions at $\gamma = 1$ using the periodic boundary fluctuation and the uniform boundary traction assumptions, respectively.

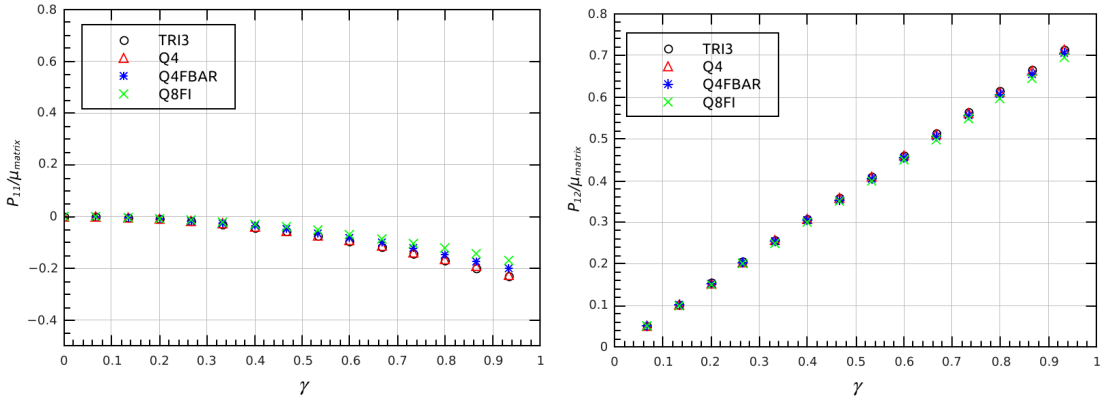

Figure 6.19: The first Piola-Kirchhoff stress for the homogenized behavior of a porous incompressible Neo-Hookean solid subjected to in-plane simple shear deformation using different discretization elements. The linear boundary displacements model is used.

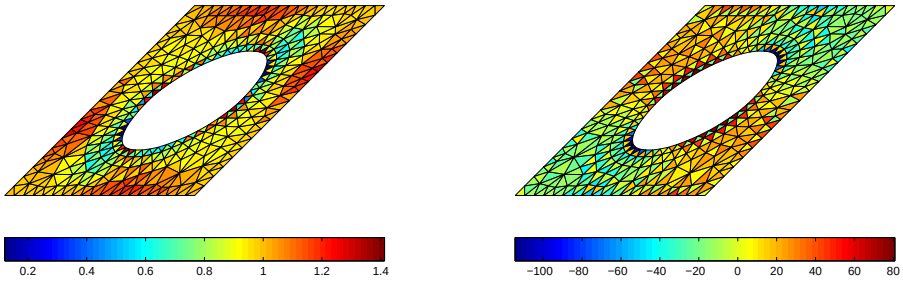

TRI3

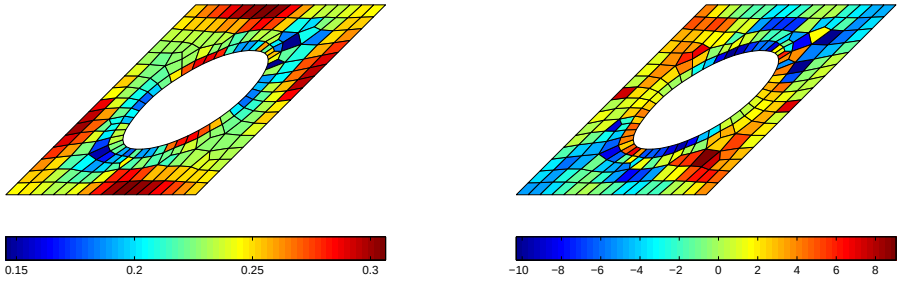

Q4

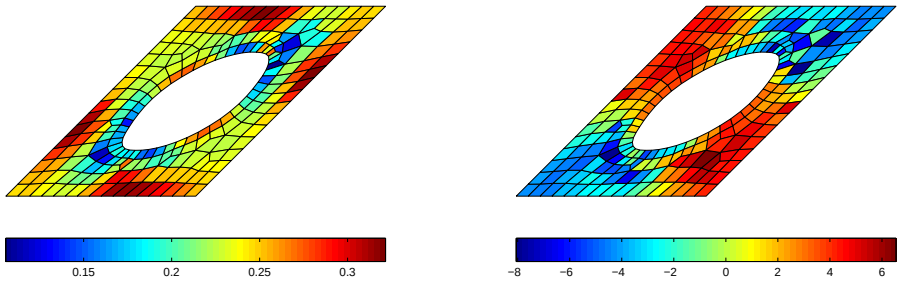

Q4FBAR

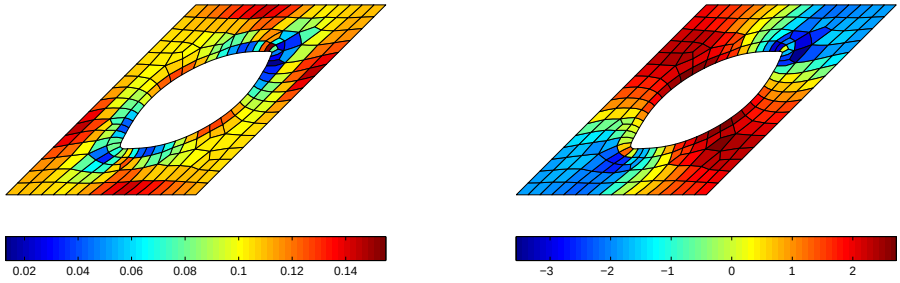

Q8FI

Figure 6.20: Shear component of the first Piola-Kirchhoff stress (P_{12}/μ) (left) and pressure distribution (right) of porous representative volumes discretized using different elements. The linear boundary displacements model is used.

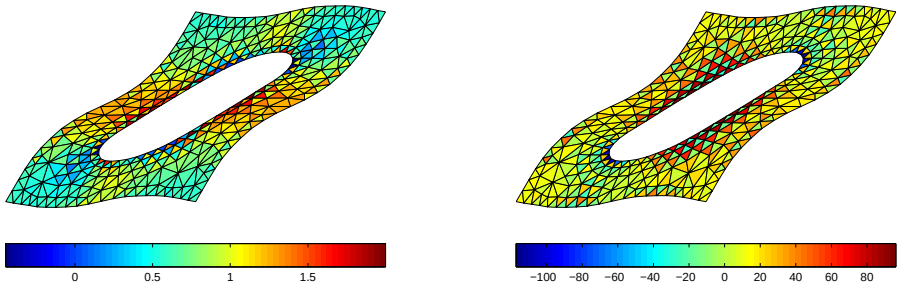

TRI3

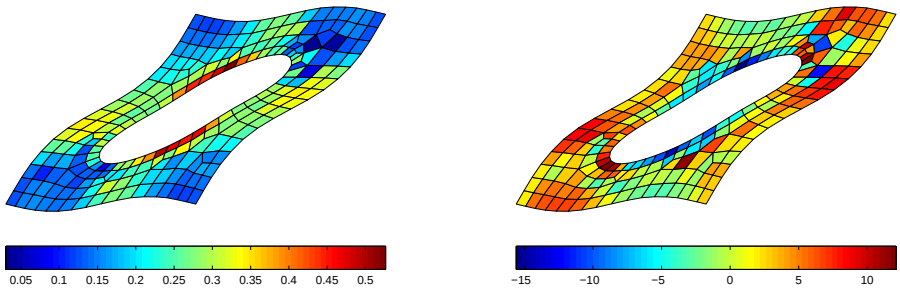

Q4

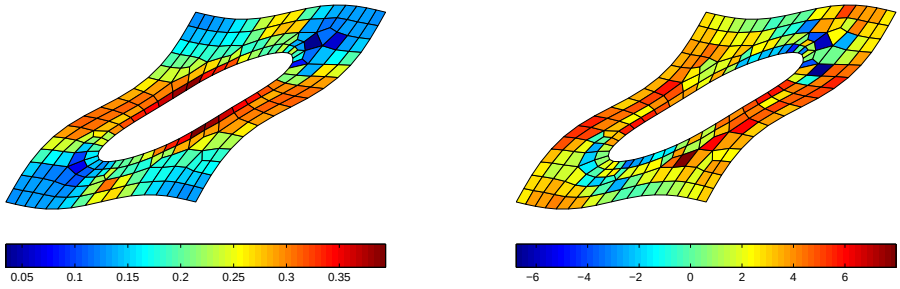

Q4FBAR

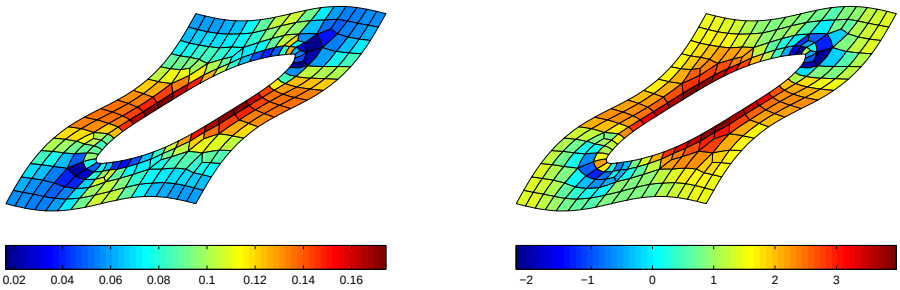

Q8FI

Figure 6.21: Shear component of the first Piola-Kirchhoff stress (P_{12}/μ) (left) and pressure distribution (right) of porous representative volumes discretized using different elements. The periodic boundary fluctuations model is used.

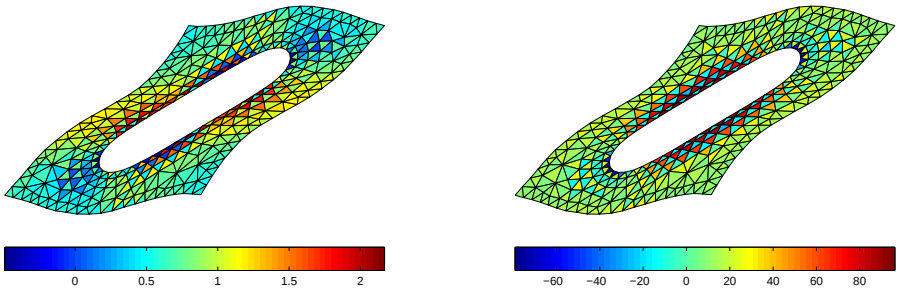

TRI3

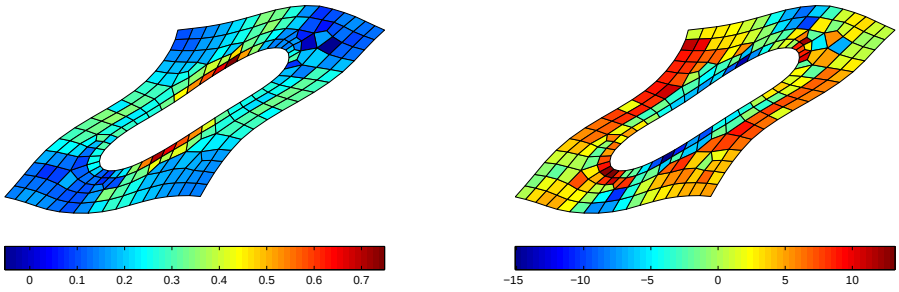

Q4

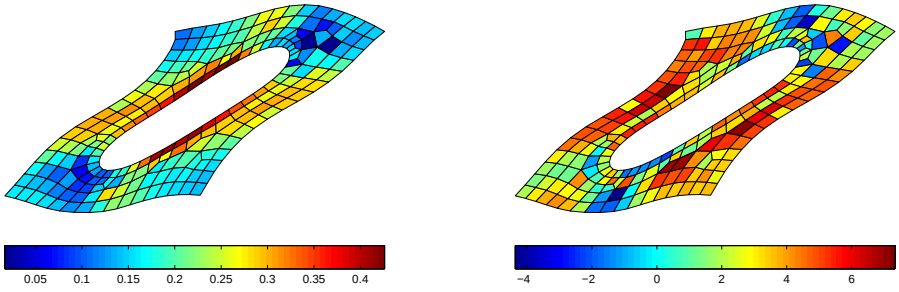

Q4FBAR

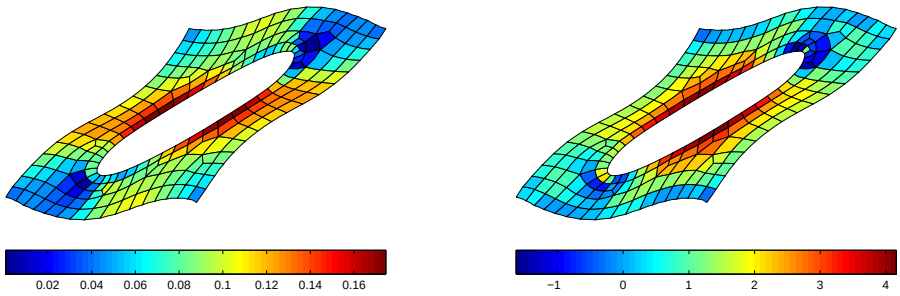

Q8FI

Figure 6.22: Shear component of the first Piola-Kirchhoff stress (P_{12}/μ) (left) and pressure distribution (right) of porous representative volumes discretized using different elements. The uniform boundary model is used.

Chapter 7

Conclusions

The description of the macroscopic behavior of heterogeneous materials based on its constituents on the microscopic level is the fundamental goal that motivated this work. In view of this, a computational framework for the homogenization-based multi-scale finite element analysis of solids at finite strains has been implemented for hyperelastic materials. One of the advantages of this framework is that it does not impose any limitations on the number of materials in the RVE. It also provides the possibility of imposing different multi-scale models.

The implemented framework has been tested on a variety of examples for porous solids and solids with rigid inclusions. Porous solids have been modelled with compressible and incompressible matrix materials showing that the multi-scale models form a band that surrounds the actual macroscopic behavior. The statistical distribution of voids has been also studied for which the estimates obtained based on computational homogenization become tighter. In addition, solids with rigid inclusions and incompressible matrix material were tested as they render an overall incompressible RVE. This case raises issues concerning their numerical treatment which was also addressed in this work.

Moreover, analytical estimates for the overall behavior of heterogeneous material have been approached. A framework based on the Second-Order Estimate has been implemented and tested against the finite element framework based on the homogenization theory. The implemented SOE was shown to be successful in approximating the behavior of a generic two-phase heterogeneous materials, even if one of the phases is a porous phase, subjected to any type of loading. It has also been shown that it is possible to approximate the behavior of compressible and incompressible RVEs with larger error values for the latter. The implemented SOE is, however, limited to two-phase composite materials. In addition, and although a clear description of the initial guesses used has been provided in the present work, the use of the fixed-point iteration algorithm requires careful choice of the initial guesses in order to obtain solutions within a reasonable number of iterations.

It is suggested for future work to include plasticity in the finite element framework. Initial developments based on von-Mises plasticity have been performed but not tested and the present computational homogenization framework provides a powerful platform for modelling behavior of heterogeneous dissipative materials. It is also advantageous to

obtain analytical estimates for the response of such heterogeneous materials. This would provide an understanding of the actual behavior of composite materials as well as the characteristics of the corresponding numerical treatment.

Appendix A

Analytical Solution for Homogeneous Simple Shear Deformation

For the purpose of testing the implemented procedure, simple shear is imposed on a homogeneous RVE and the output is compared to the analytical solution derived for each of the material models. The procedure followed by [30] and [33] provides the basis of the derivation of the analytical solutions.

Simple shear is an isochoric plane deformation defined by the amount of deformation γ. The deformation gradient in this case is

$$\begin{aligned} \boldsymbol{F} &= \boldsymbol{I} + \gamma \boldsymbol{e}_1 \otimes \boldsymbol{e}_2, && \text{(A.1)} \\ &= \begin{bmatrix} 1 & \gamma & 0 \\ 0 & 1 & 0 \\ 0 & 0 & 1 \end{bmatrix}, \\ &= \begin{bmatrix} \lambda_1 & 0 & 0 \\ 0 & \lambda_2 & 0 \\ 0 & 0 & 1 \end{bmatrix}, && \text{(A.2)} \end{aligned}$$

where $\boldsymbol{e}_1$ and $\boldsymbol{e}_2$ are the current orthonormal basis vectors.

Equation A.2 comes from the fact that the rotation tensor $\boldsymbol{R} = \boldsymbol{I}$ for simple shear deformation, hence the polar decomposition reduces to $\boldsymbol{F} = \boldsymbol{V}$. Tensor $\boldsymbol{V}$ can be expressed in terms of the principal stretches λ_1, λ_2 and $\lambda_3(= 1)$, and taking into account that simple shear does not involve any changes in volume,

$$J = \det \boldsymbol{F} = 1 \implies \lambda_1 \lambda_2 = 1. \tag{A.3}$$

Consequently, $\lambda_1 = \lambda_2^{-1} = \bar{\lambda}$. By performing the spectral decomposition of the left Cauchy-

Green strain tensor $\boldsymbol{B}$

$$\begin{aligned}
\det(\boldsymbol{B} - \bar{\lambda}^2\boldsymbol{I}) &= 0,\\
\det\begin{vmatrix} 1+\gamma^2-\bar{\lambda}^2 & \gamma & 0 \\ \gamma & 1-\bar{\lambda}^2 & 0 \\ 0 & 0 & 1-\bar{\lambda}^2 \end{vmatrix} &= 0,\\
\bar{\lambda}^4 - (\gamma^2+2)\bar{\lambda}^2 + 1 &= 0,\\
\bar{\lambda}^2 - (\gamma^2+2) + \bar{\lambda}^{-2} &= 0,\\
\bar{\lambda}^2 + \bar{\lambda}^{-2} - 2 = \gamma^2 \implies \bar{\lambda} + \bar{\lambda}^{-1} &= \gamma.
\end{aligned} \tag{A.4}$$

The orientation θ with respect to the Lagrangian principal axes is related to γ, according to [30], as

$$\tan(2\theta) = \frac{2}{\gamma} \quad 0 < \theta \leq \frac{\pi}{4}. \tag{A.5}$$

Consequently, the principal unit vectors are defined, as a function of θ, as

$$\begin{aligned}
\boldsymbol{n}_1 &= \cos\theta\boldsymbol{e}_1 + \sin\theta\boldsymbol{e}_2\\
\boldsymbol{n}_2 &= -\sin\theta\boldsymbol{e}_1 + \cos\theta\boldsymbol{e}_2\\
\boldsymbol{n}_3 &= \boldsymbol{e}_3.
\end{aligned} \tag{A.6}$$

Compressible Neo-Hookean Model

From the constitutive equation 2.45 and taking into account Equation A.3, the Cauchy stress is expressed as

$$\boldsymbol{\sigma} = \mu(\boldsymbol{B} - \boldsymbol{I}), \tag{A.7}$$

and, consequently, the principal components of $\boldsymbol{\sigma}$ are obtained as

$$\sigma_1 = \mu(\lambda_1^2 - 1) = \mu(\bar{\lambda}^2 - 1), \text{ and} \tag{A.8}$$

$$\sigma_2 = \mu(\lambda_2^2 - 1) = \mu(\bar{\lambda}^{-2} - 1). \tag{A.9}$$

The Hencky Model

The Cauchy stress is related to the Kirchhoff stress by the Jacobian J, hence, and as a consequence of Equation A.3, $\boldsymbol{\sigma} = \boldsymbol{\tau}$. Using Equation 2.60, the Cauchy stress can be expressed as

$$\begin{aligned}
\boldsymbol{\sigma} &= 2\mu\ln\boldsymbol{V} + \lambda\,\mathrm{tr}(\ln\boldsymbol{V})\boldsymbol{I},\\
&= 2\mu\ln\boldsymbol{V},
\end{aligned} \tag{A.10}$$

where $\mathrm{tr}(\ln \boldsymbol{V}) = \ln \bar{\lambda} + \ln \bar{\lambda}^{-1} + \ln 1 = 0$. The principal components of $\boldsymbol{\sigma}$ are

$$\sigma_1 = 2\mu \ln \lambda_1 = 2\mu \ln \bar{\lambda}, \text{ and} \tag{A.11}$$
$$\sigma_2 = 2\mu \ln \lambda_2 = -2\mu \ln \bar{\lambda}, \tag{A.12}$$

In order to compare the analytical solutions to those obtained by the multi-scale formulation, a homogeneous RVE made of hyperelastic material with Young's Modulus of 200 GPa and Poisson's ratio of 0.3 is discretized with 32 linear triangular elements and subjected to a simple in-plane shear with shear magnitude of γ. The values of the component P_{12} of the first Piola-Kirchhoff stress are evaluated and plotted against the analytical solution of the corresponding component for $\gamma \in [0, 2]$. The output of both procedures is plotted in Figure A.1 for both material models described. It can be seen from Figure A.1

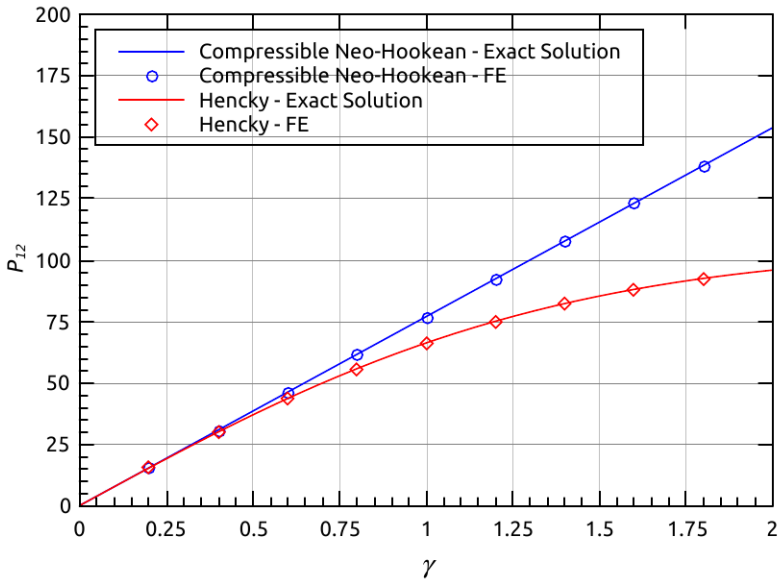

Figure A.1: Analytical solution versus multi-scale solution obtained for a homogeneous RVE made of 32 linear triangular elements subjected to Periodic Boundary Conditions.

that both solutions coincide. It should also to be noticed that the solution obtained by the multi-scale code implemented is reached in one step as this setting corresponds to the Taylor model where no solution is required.

Bibliography

[1] Bonet J. and Wood R.D. *Nonlinear Continuum Mechanics for Finite Element Analysis*. Cambridge University Press, 2008.

[2] Bouchart V. et al. Implementation and numerical verification of a non-linear homogenization method applied to hyperelastic composites. *Computational Materials Science* 43 (2008), pp. 670–680.

[3] de Souza Neto E.A., Andrade Pires F.M., and Owen D.R.J. F-bar-based linear triangles and tetrahedra for finite strain analysis of nearly incompressible solids. Part I: formulation and benchmarking. *International Journal for Numerical Methods in Engineering* 62 (2005), pp. 353–383.

[4] de Souza Neto E.A. and Feijóo R.A. Variational Foundations of Multi-Scale Constitutive Models of Solid: Small and Large Strain Kinematical Formulation. *National Laboratory for Scientific Computing (LNCC/MCT), Brazil, Internal Research and Development Report* 16/2006 (2006).

[5] de Souza Neto E.A., Perić D., and Owen D.R.J. *Computational Methods for Plasticity: Theory and Applications*. Wiley, 2008.

[6] de Souza Neto E.A. et al. Design of simple low order finite elements for large strain analysis of nearly incompressible solids. *International Journal of Solids and Structures* 33 (1996), pp. 3277–3296.

[7] deBotton G. Transversely isotropic sequentially laminated composites in finite elasticity. *Journal of the Mechanics and Physics of Solids* 53 (2005), pp. 1334–1361.

[8] Hashin Z. Large isotropic elastic deformation of composites and porous media. *International journal of solids and structures* 21 (1987), pp. 711–720.

[9] Hill R. A self-consistent mechanics of composite materials. *Journal of Mechanics and Physics of Solids* 13 (1965), pp. 213–222.

[10] Holzapfel G.A. *Nonlinear Solid Mechanics: A Continuum Approach for Engineering*. John Wiley & Sons, 2000.

[11] Idiart M.I. Modeling the macroscopic behavior of two-phase nonlinear composites by infinite-rank laminates. *Journal of Mechanics and Physics of Solids* 56 (2008), pp. 2599–2617.

[12] Kouznetsova V., Brekelmans W.A.M., and Baaijens F.P.T. An approach to micro-macro modeling of heterogeneous materials. *Computational Mechanics* 17 (2001), pp. 37–48.

[13] Krätschmer D. Weiterentwicklung eines schädigungsmechanischen Modells zur Berechnung einer maximal zulässigen Werkstoffausnutzung unter schwingender Beanspruchung angewandt auf eine Aluminiumgusslegierung. PhD thesis. Abschlussbericht, IMWF Universität Stuttgart, 2009.

[14] Lahellec N., Mazerolle F., and Michel J.C. Second-order estimate of the macroscopic behavior of periodic hyperelastic composites: theory and experimental validation. *Journal of the Mechanics and Physics of Solids* 52 (2004), pp. 27–49.

[15] Levin V.M. Thermal expansion coefficients of heterogeneous materials. *Mekhanika Tverdogo Tela* 2 (1967), pp. 83–94.

[16] Lopez-Pamies O. and Ponte Castañeda P. Homogenization-based constitutive models for porous elastomers and implications for macroscopic instabilities: I-Analysis. *Journal of the Mechanics and Physics of Solids* 55 (2007), pp. 1677–1701.

[17] Lopez-Pamies O. and Ponte Castañeda P. On the overall behavior, microstructure evolution, and macroscopic stability in reinforced rubbers at large deformations: I-Theory. *Journal of the Mechanics and Physics of Solids* 54 (2006), pp. 807–830.

[18] Lopez-Pamies O. and Ponte Castañeda P. On the overall behavior, microstructure evolution, and macroscopic stability in reinforced rubbers at large deformations: II-Application to cylindrical fibers. *Journal of the Mechanics and Physics of Solids* 54 (2006), pp. 831–863.

[19] Lopez-Pamies O. and Ponte Castañeda P. Second-Order Estimates for the macroscopic response and loss of ellipticity in porous rubbers at large deformations. *Journal of Elasticity* 76 (2004), pp. 247–287.

[20] Lopez-Pamies O. An exact result for the macroscopic response of particle-reinforced Neo-Hookean solids. *Journal of Applied Mechanics* 77 (2010).

[21] Lopez-Pamies O. An exact result for the macroscopic response of porous Neo-Hookean solids. *Journal of Elasticity* 95 (2009), pp. 99–105.

[22] Lopez-Pamies O. et al. On the extremal properties of Hashin's hollow cylinder assemblage in nonlinear elasticity. *Journal of Elasticity* 107 (2012), pp. 1–10.

[23] Mandel J. Plasticité Classique et Viscoplasticité. *CISM Courses and Lectures No. 97.* (1971).

[24] Masson R. New explicit expressions of the Hill polarization tensor for general anisotropic elastic solids. *International Journal of Solids and Structures* 45 (2008), pp. 757–769.

[25] Miehe C., Schotte J., and Schröder J. Computational micro-macro transitions and overall moduli in the analysis of polycrystals at large strains. *Computational Materials Science* 16 (1999), pp. 372–382.

[26] Moffatt W.G., Pearsall G.W., and Wulff J. *The Structure and Properties of Materials*. Vol. I. John Wiley & Sons, p. 140.

[27] Moulinec H. and Suquet P. A numerical method for computing the overall response of nonlinear composites with complex microstructure. *Computer* 157 (1998), pp. 69–94.

[28] Nebozhyn M.V. and Ponte Castañeda P. Second-order estimates for the effective behavior of nonlinear porous materials. *Symposium on Transformation Problems in Composite and Active Materials* (1998), pp. 73–88.

[29] Nemat-Nasser S. Averaging theorems in Finite deformation plasticity. *Mechanics of Materials* 31 (1999), pp. 493–525.

[30] Ogden R.W. *Non-Linear Elastic Deformation*. Dover Civil and Mechanical Engineering. Dover Publications, INC, 1997.

[31] Okolo B. *Microstructure and Properties of Engineering Materials, lecture notes*. The German University in Cairo, 2010.

[32] Perić D., Owen D.R.J., and Honnor M.E. A model for finite strain elasto-plasticity based on logarithmic: Computational issues. *Computer Methods in Applied Mechanics and Engineering* 94 (1992), pp. 35–61.

[33] Perić D. et al. On micro-to-macro transitions for multi-scale analysis of non-linear heterogeneous materials: unified variational basis and finite element implementation. *International Journal for Numerical Methods in Engineering* 87 (2011), pp. 149–170.

[34] Ponte Castañeda P. and Tiberio E. A second-order homogenization method in finite elasticity and applications to black-filled elastomers. *Journal of the Mechanics and Physics of Solids* 48 (2000), pp. 1389–1411.

[35] Ponte Castañeda P. Bounds for nonlinear composites via iterated homogenization. *Journal of the Mechanics and Physics of Solids* 60 (2012), pp. 1583–1604.

[36] Ponte Castañeda P. Exact second-order estimates for the effective mechanical properties of nonlinear composite materials. *Journal of the Mechanics and Physics of Solids* 44 (1996), pp. 827–862.

[37] Ponte Castañeda P. Second-order homogenization estimates for nonlinear composites incorporating field fluctuations: II - applications. *Journal of the Mechanics and Physics of Solids* 50 (2002), pp. 759–782.

[38] Ponte Castañeda P. The overall constitutive behaviour of nonlinearly elastic composites. *Proceedings of the Royal Society of London, Series A. Mathematical and Physical Sciences* 422 (1989), pp. 147–171.

[39] Somer D. Computational Strategies for Multi-Scale Analysis of Solids: Small and Large Strain Formulations. PhD thesis. Civil and Computational Engineering Centre, Swansea University, UK, 2009.

[40] Speirs D. Characterisation of Materials with Hyperelastic Microstructures through Computational Homogenisation and Optimisation Methods. PhD thesis. Civil and Computational Engineering Centre, Swansea University, UK, 2007.

[41] Suvorov A.P. and Dvorak G.J. Rate form of the Eshelby and Hill tensors. *International Journal of Solids and Structures* 39 (2002), pp. 5659–5678.

[42] Zohdi T.I. and Wriggers P. *Introduction to Computational Micrmechanics*. Springer, 2005.

[43] *MATLAB Documentation*. Mathworks.com. 2013.